The analysis of inset dielectric guide and its application in leaky wave antennas

Ma, Lizhuang

Award date:
1989

Awarding institution:
University of Bath

THE ANALYSIS OF INSET DIELECTRIC GUIDE AND ITS APPLICATION IN LEAKY WAVE ANTENNAS

submitted by Lizhuang Ma

for the degree of PhD

of the University of Bath

1989

Ma Lizhuang

ProQuest LLC
789 East Eisenhower Parkway
P.O. Box 1346
Ann Arbor, MI 48106-1346

SUMMARY

This thesis is concerned with the analysis of Inset Dielectric Guide (IDG) and its applications on microwave and millimetric leaky wave antennas. IDG, as a variation of Image Line, seems to offer better performance, easier manufacture and particular promise for antenna applications.

A rigorous six-component hybrid mode analysis by using the Transverse Resonance Diffraction method is reviewed briefly. Then LSE/LSM approximation is used in the examination of the dispersion characteristics for relatively deeper and shallower slots. The results show excellent agreement with the measured curves.

IDG as an open transmission medium includes in its spectrum a range of continuous modes. This thesis pays appropriate attention on the mode completeness and the orthonormalization of the discrete and continuous spectrum of the IDG in the LSE/LSM description. Green's function is derived in the form of eigenfunction expansion, which is an essential prerequisite to the analysis of discontinuity problems.

A variational expression for the equivalent circuit of the radiating dipole is derived and applied to the design of a 23-element vertically polarized array. The array is built and tested showing excellent performance.

IDG antennas are concluded to be of practical importance due to their easier factoring, low cost and reasonably good performance. Further work is in progress.

ACKNOWLEDGEMENTS

The author would like to express her sincere thanks to Professor T. Rozzi for his continuous encouragement and expert guidance during the course of this work.

The author would like to thank all her colleagues and friends in the School of Electrical Engineering, University of Bath for their true friendship and help in various respects. Thanks especially go to Dr. S. Hedges for his previous work. The help of Mr. T. Murphy and Mr. J. Griffiths in performing the measurements is gratefully acknowledged.

This work was funded by a grant from the Science and Engineering Research Council and by a British Telecom China Fellowship approved by The Royal Society. Many thanks are due to both of these organizations.

CONTENTS

PUBLICATIONS ARISING FROM THIS WORK

[1] T. Rozzi and L. Ma, 'Scattering by dipoles in I.D.G and Application to Millimetric Leaky Wave Antennas', Proceedings of the 17th European Microwave Conference, Rome, September 1987, pp. 543-548.

[2] T. Rozzi and L. Ma, 'Mode Completeness, Normalization and Green's Function of the Inset Dielectric Guide', IEEE Trans. Microwave Theory and Techniques, Vol. MTT-36, March 1988 pp. 542-551.

[3] T. Rozzi, L. Ma, R. de Leo and P. Morini, ' Equivalent Network of Transverse dipoles on Inset Dielectric Guide (IDG): Application to Linear Arrays', IEEE Trans. Antenna and Propagation, to be published.

[4] R. de Leo, L. Ma, A. Morini and T. Rozzi, 'Analisi di schiere di antenne su guida d'onda di tipo inset', National Conference on Applied Electromagnetism, Rome, Sept. 1988.

CHAPTER 1

INTRODUCTION

1.1 Introduction

Millimeter wave techniques have evolved rapidly during the last decade. The advantages associated with the use of millimeter wavelengths arise from the compactness of the antenna and electronic circuitry, the broad bandwidth and the propagation aspects. The small size of the electronic equipment enables radar and radiometry acquisition to be employed on small missiles or aircrafts and allows high spatial resolution to be obtained from an electronic package of small volume. The great bandwidth available at these frequencies can support high capacity point to point links and the channels can also be widely separated to prevent cross-channel interference. Of course, optical systems offer even higher resolution and wider band, but they are limited to fog, cloud and smoke free condition and have poor volume search capabilities. Millimeter wave systems operating in the propagation windows at 94, 140 and 220 *GHz* offer very significant advantages for high resolution all weather operation. For communications, use is also made of high attenuation bands for security using line-of-sight transmission; 60 *GHz* is the commonly used frequency for such purposes.

Although there are clearly many advantages to be obtained by using systems at millimeter wave frequencies, there at present is a paucity of commercially available systems. This is due, apart from the poor performance and high cost of solid state devices at these frequencies, which is out of the topic of this thesis, to that there is no preferred medium for designing and building circuits.

One might imagine that the circuitry and antenna required by these new millimeter wave systems could be developed by scaling down in size those at lower frequency. While this is indeed true for some millimeter wave systems, it is not generally the case due to tolerance problems and costly manufacture. It is recognized that for operating frequencies in excess of 90 *GHz* new circuit techniques must be developed.

Also where antennas are required to be conformal to a vehicle surface, millimeter wave reflector and horn antennas are often too bulky and expensive, particularly where some form of beam-scanning is required. For conformal applications, ideally, the receiver/transmitter circuitry needs to be integrated as far as possible with the antenna structure and current trends in antenna design have been considerably influenced by the advances in semiconductor diode and source devices.

For the above reasons the requirements for developing new circuit techniques and new classes of low profile substrate-based planar antennas for the use at millimeter wave bands have been increasing during the last ten years and this in fact was the stimulus for the work presented in this thesis.

This introductory chapter intends to put this work into context and to give a synopsis of the following chapters. The first section introduces the motivation of the thesis. The next section outlines the generalities about dielectric lines and introduces Inset Dielectric Guide (*IDG*). The third section briefly discusses the feasibility of two types of arrays formed on *LSE*- and *LSM*-mode supporting *IDG*. This chapter concludes with an

outline of the work presented in the remaining eight chapters.

1.2 Millimeter Wave Transmission Line and IDG

Considerable effort has been spent on the development of transmission media suitable for millimeter wave communications.

As operating frequency increases above $30\,GHz$, the cost of rectangular metal waveguide components increases because of tight fabrication tolerances, and the losses depend increasingly on surface finish. High circuit costs may in fact become the limiting factor to the ever increasing commercial development in millimeter wave technology. Thus, the ease of manufacture and capability for mass production is becoming as important a criteria as the circuit performance of such media.

The line losses also constitute an important parameter in the evaluation of a transmission line. Some standard microwave structures, like microstrip, finline, suspended stripline etc. reveal high losses and poor Q-factor (100 to 700 only) at millimeter frequencies, that makes them not suitable to form resonators for use in filters, oscillators and fine frequency discriminators. It was realized that for frequencies above $100\,GHz$ a dielectric guide would be required. The major advantage of dielectric lines is their lower loss with values of less than $10^{-2}\,dB$/wavelength and higher Q-factor of several thousands at lower millimeter frequencies.

The image line is a recognized low loss transmission media with unloaded Q-factor of 2500, but its main disadvantage, besides manufacturing difficulties, is its radiation loss from all practical components. For further confining the field to the structure, the trapped image guide has been proposed [1], but it is even more difficult to make, especially for small guide dimensions. In order to overcome such manufacturing

difficulties, *IDG*, shown in cross section in Fig.1.1, has been proposed as a low cost alternative [2]. *IDG*, which is just a rectangular groove filled with dielectric material, has many of the advantages of the trapped image guide without its fabrication problems.

Standard grooves are easy to be formed on a metal sheet or they can be fabricated in a plastic mould, that can be subsequently spray-metallized.

Low melting point dielectric can be poured in the groove in liquid form, which is sufficient for many applications.

High quality dielectric slabs can be cut to a specified rectangular shape. Contact with the metal walls is not as critical as for image guide.

There is also a considerable problem in incorporating active devices in image line arising from the unwanted radiation. This could be significantly eased in *IDG* because of the better field confinement. An investigation of the implementation of an active device in *IDG* was given by Hedges [3].

Compared with the image guide three distinct advantages can be expected to arise from the use of the *IDG* structure:

1) simpler manufacture

2) lower radiation loss, especially from bends

3) easier embedding of active devices.

The *IDG* structure was analyzed, previously, by Zhou and Itoh [4], as an intermediate structure in the analysis of trapped image guide. That analysis used the effective dielectric constant (*EDC*) method and it gave useful and accurate approximate results for the fundamental mode.

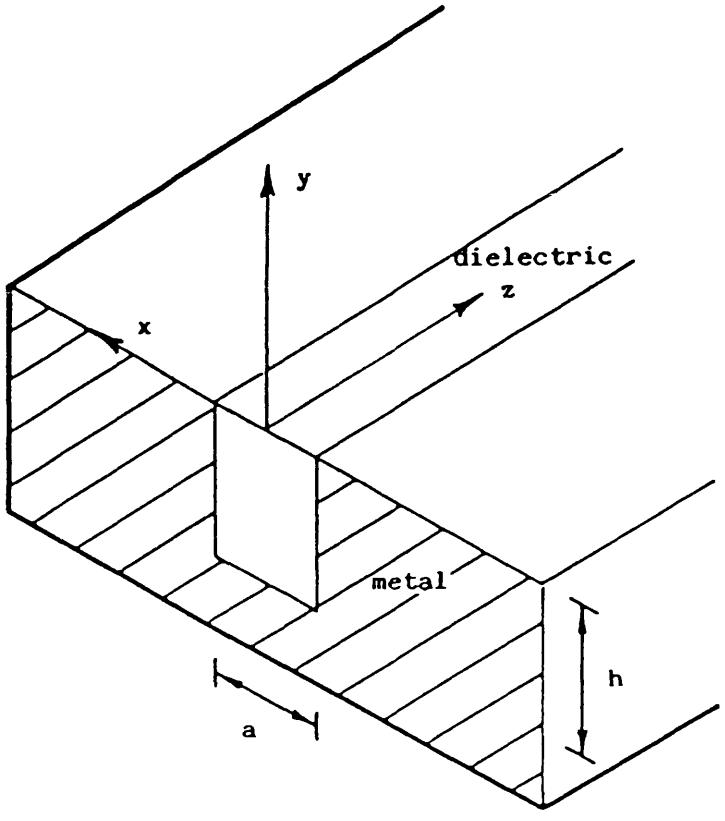

Figure 1.1 The cross-sectional structure
of Inset Dielectric Guide.

The 90^0 edge, however, imposes a singularity on the transverse fields, which is important for the accurate evaluation of field distributions and radiation properties.

Consideration was given to the above problem in the rigorous, full hybrid treatment by the method of Transverse Resonance Diffraction (*TRD*) [5]. The discrete spectrum was evaluated, together with propagation losses and Q-factors for the fundamental and a number of higher order discrete modes. Those results show that, away from cutoff, propagation losses are dielectric-dominated.

For *IDG* there are two useful regions of single mode operation. The first one is to operate with the H_{01} mode in relatively deep slots. The second region is with the E_{11} mode in shallow, broad slots. Moreover, for practical aspect ratios, the assumption of a single *LSE* or *LSM* potential gives a very good description, provided that the edge conditions are still accounted for in the field distribution over the slot aperture, which implies that the potential is intrinsically non-separable.

The *IDG* is an open waveguide and, consequently, its spectrum includes, besides one or a few discrete modes, a continuous range of modes, which were not considered before. The excitation of the latter takes place due to discontinuities, particularly when these are located close to the air-dielectric interface, such as metal posts (e.g. diodes) or radiating dipoles, if the *IDG* is to be used as a leaky wave antenna. Therefore, with a view to analyzing practical components in *IDG*, it is necessary to obtain a complete spectral characterization, inclusive of the continuum.

In the course of this thesis we are going to determine the orthonormalized discrete and continuous spectra. Then the eigenfunction expression of the Green function for the *IDG* in the *LSE/LSM* description is derived. Finally, the results are used in the design of two differently polarized array antennas.

1.3 The Feasibility of Arrays Formed on IDG

The growing interest in the use of millimeter wavelengths for radar and communication systems stems principally from military requirements. Conventional antenna technology utilizing reflectors and horns continues to feature but seems too bulky and expensive. Strenuous efforts are being made to devise new fabrication methods leading to further miniaturization, integration and cost saving.

Increasing attention has been paid to developing new classes of low profile substrate-based planar antennas that can be flush-mounted on vehicles and missiles and can possibly allow some degree of circuit integration together with additional means of electronic scanning by semiconductor implant or frequency sweeping.

A large number of different forms of novel planar antenna structures for millimeter wavelengths have been invented. They can be broadly characterized as

1) purely dielectric guides and radiating elements,

2) metal radiating elements.

Dielectric waveguide, originally a promising solution for a very low-loss transmission medium, has turned out disappointing in regards to integration of active devices, fabrication and tolerance to discontinuities. On the other hand, dielectric waveguide seems to offer promise for the realization of integrated leaky-wave antennas.

Purely dielectric arrays, which are particularly suitable for use at the upper millimeter band, have been derived from integrated optical techniques and have an intrinsic low loss. At present, however, they are not easy to manufacture, except possibly by thick film techniques and can not be made by simple etching processes as used for their metal counterparts.

Microstrip patch antennas [6] obviously belong to the second class. They are cheap and easy to fabricate, but their poor Q- and polarization properties are well known, particularly above 90 GHz.

Recently, some very elaborate approaches employing dielectric guide configurations loaded by some metal disks or strips were reported for millimeter wave applications. For example, in 1982 Itoh proposed a trapped image guide leaky wave antenna [7]. In 1985 Solbach developed a hybrid dielectric image-line antenna array, using double metal disks printed on the top of the guide configuration [8]. We considered carefully these experiences.

The possibility of realising low-cost, easy to fabricate, relatively high-quality antennas of the leaky-wave type based on the *IDG* configuration has been the object of a feasibility study. It is easy to lay thin metal strips on the air dielectric interface, that act as dipole radiators. The principle of operation is as follows: for *IDG* operating in its fundamental *LSE*-mode the main component of the electric field is x-directed and is not far from its maximum value at the air-dielectric interface. Induced currents are therefore easily set up in the transverse strips without twisting of the field lines, as is the case in microstrip patch antennas and image line antennas. The strips in turn act as x-directed dipole radiators. By placing uniformly spaced metal strips on the surface of the dielectric, a vertically polarized array is created, as shown in Fig.1.2, which produces a fan beam at microwave or millimeter wave frequency. For *LSM*-mode supporting *IDG*, the main component of the electric field is z-directed and is maximum at the center of the interface, where the x-directed electric field is zero. Therefore, when a longitudinal strip is located at the center of the guide, it acts as a z-directed dipole radiator and a horizontally polarized array can be formed by a series of strips, as shown in Fig.1.3.

In view of these essential properties, this type of array has some potential advantages, namely,

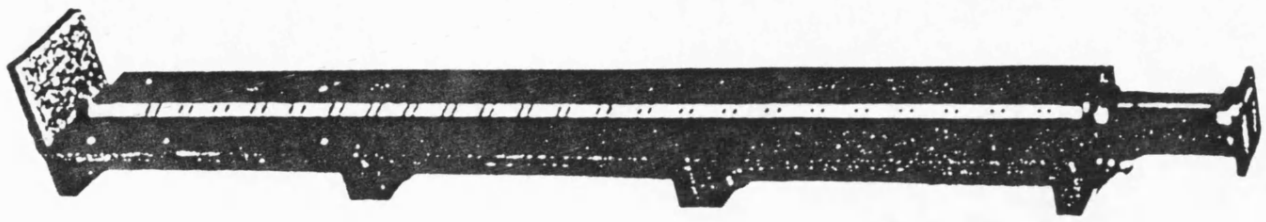

Figure 1.2 The photograph of a 23-element
Taylor's excitation array formed on LSE mode supporting IDG.

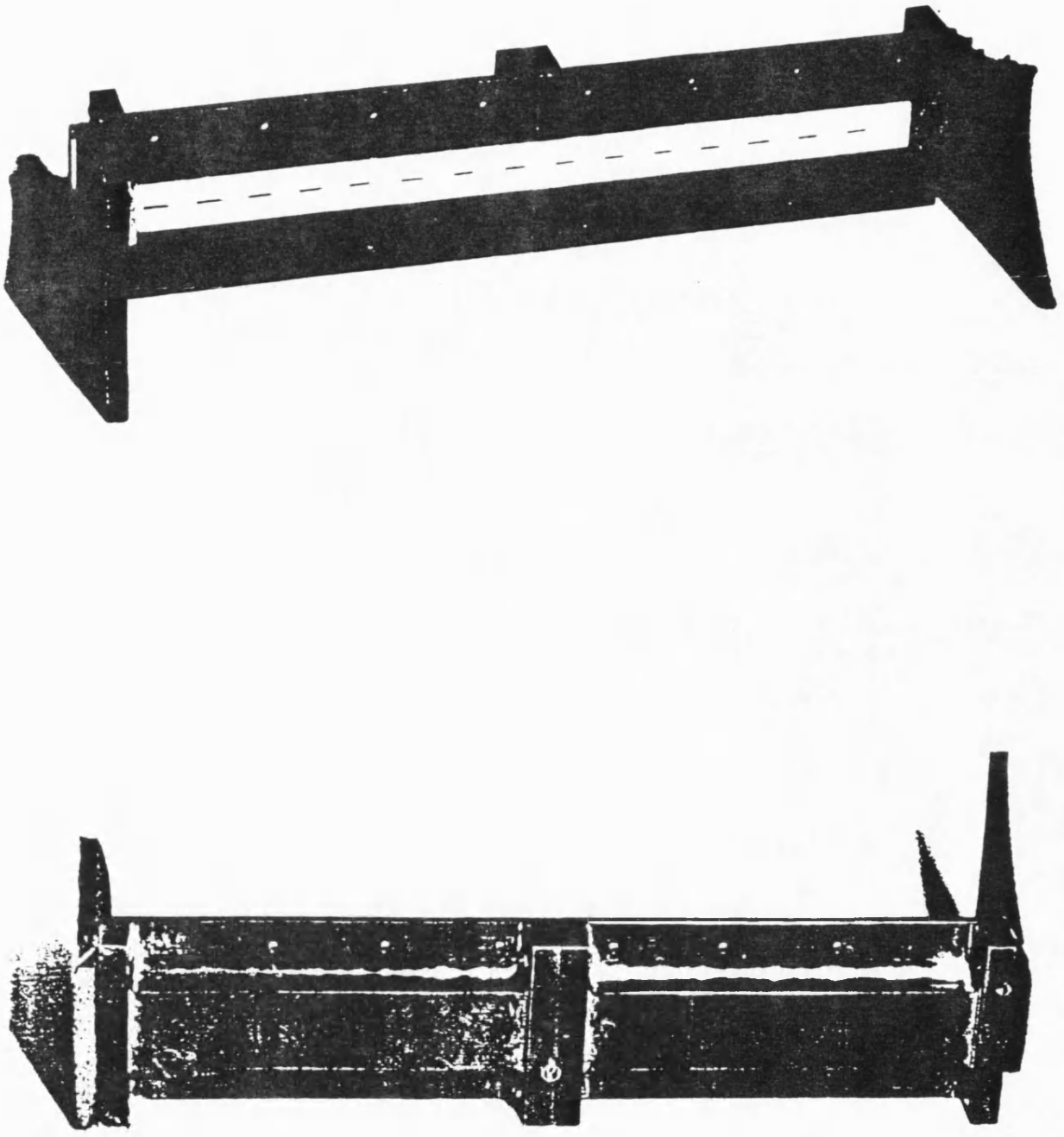

Figure 1.3 The photographs of a horizontally polarized array formed on LSM mode supporting IDG showing the coaxial feed.

1) ease of manufacture,

2) low loss,

3) low mutual coupling,

4) negligible generation of cross-polarized field,

5) physically compatibility with conventional waveguide or coaxial feeds.

Two one-dimensional arrays were designed, fabricated and tested. The measured results are very encouraging indeed.

1.4 The Structure of the Thesis

This section briefly outlines the content of the thesis. This is an introductory chapter. The remainder of the work contains seven chapters. Chapter 2 is used to introduce some fundamental concepts and theory about linear arrays. The design of the array excitation for uniform distribution and Dolph-Chebyshev's and Taylor's distributions is discussed. The realization of the actual aperture distribution is also given in this chapter.

Chapter 3 deals with the discrete spectrum. It gives a rigorous analysis of *IDG*, introduces an approach yielding an accurate transverse equivalent network for the fundamental mode using the method of transverse resonance diffraction (*TRD*). The loss characteristics of *IDG* are discussed in the end of the chapter.

Chapter 4 is devoted to complete the characterization of the spectrum to include the continuum and verify their orthonormalization for the even *LSE*(TE^z)-polarization, having $E_y = 0$ and E_x as the main electric field component. The scalar Green function is subsequently determined, which is a prerequisite for the solution of discontinuity problems. As an example of the use of Green's function, the radiation of a thin, single

transverse dipole at the air-dielectric interface is analyzed. An analogous analysis for the odd *LSM* (TM^y)-polarization, having $H_y = 0$ and E_z as the main electric field component is given in Chapter 6.

Chapter 5 develops the equivalent network of a single transverse dipole for the *LSE*-case. The result is used in the design of a 23-element Taylor's distribution array. The array was built and tested. The experimental results shown in this chapter are in excellent agreement with the theory.

The scattering parameters of a single longitudinal dipole on the air-dielectric interface are measured by means of the electric-probe technique and the HP network analyzer. The results are shown in Chapter 7.

A very primitively designed array is discussed. The measured result shows that this kind of construction holds promise for a good horizontally polarized array.

In conclusion, Chapter 8 summarizes the implication of this work for the study of the complete spectrum of *IDG* and the realization of this kind of leaky-wave antenna. Further research in this area is suggested.

REFERENCES

[1] T. Itoh and B. Adelseck, " Trapped image guide for millimeter wave circuits ", *IEEE Trans. Microwave Theory and Tech., vol. MTT*-28, pp. 1433-1436, Dec. 1980.

[2] S. C. Gratze, " Inset dielectric guide ", Proposal YBO 881, Marconi Research Laboratories.

[3] S. Hedges, " The analysis of inset dielectric guide by transverse resonance diffraction ", PhD Thesis.

[4] W. Zhou and T. Itoh, " Analysis of trapped image guide using effective dielectric constant and surface impedances ", *IEEE Trans. Microwave Theory and Tech., vol. MTT*-30, pp. 2163-2166, Dec. 1982.

[5] T. Rozzi and S. Hedges, " Rigorous analysis and network modeling of inset dielectric guide ", *IEEE Trans. Microwave Theory and Tech., vol. MTT*-35, pp. 823-834, Sep. 1987.

[6] J. R. James P. S. Hall and C. Wood " Microstrip Antenna Theory and Design " (Peter Peregrinus, Stevenage, 1981).

[7] T.Itoh and B.Adelseck, " Trapped Image Guide Leaky-Wave Antennas for Millimeter Wave Applications ", *IEEE Trans. Antenna and Propag. vol. AP-* 30, pp. 505-509, May 1982.

[8] K. Solbach, " Hybrid Design Proves Effective for Flat Millimeter-Wave Antennas", *Military Microwaves* pp.123-138 June 1985.

CHAPTER 2

THEORY OF LINEAR ARRAYS

2.1 Introduction

A single strip on IDG can radiate energy into space, but it is not possible to obtain the value of directivity or beamwidth required for many practical applications with a single strip. We require therefore antennas composed of several strips, i.e. arrays.

The starting point of array theory is the superposition principle. Upon using this principle in the calculation of the far field pattern of an array, we obtain the pattern multiplication principle. This states that the far field pattern of an antenna system composed of identical elements can be written as the product of two factors, namely, an element factor and an array factor (or space factor). The former is essentially the far field from a single element, which in our case will be discussed in Chapters 4 and 6. The present chapter will focus its attention on the latter factor, (dimensionless, scalar, and element-independent), which controls the features of radiation from the array. The array factor can be considered as the pattern of a hypothetical array consisting of isotropic radiators.

In Sec.2.2, a particularly simple array, a uniform array, is discussed, which gives

maximum directivity but a fixed maximum sidelobe level of $-13.5\ dB$. The very useful concept of Schelkunoff's unit circle representation is introduced in Sec.2.3. When sidelobes lower than those provided by uniform illumination are required, the aperture distribution needs to be tapered from the center to the ends. The two most used distributions for obtaining radiation patterns with narrow beamwidth and low sidelobes, Dolph-Chebyshev's and Taylor's distributions, are discussed in Secs.2.4 and 2.5 respectively. Sec.2.6 discusses the realization of the actual aperture distribution.

2.2 Uniformly Excited Array

Imagine a linear array consisting of N elements spaced equidistantly by d along the z-axis of a rectangular coordinate system whose origin coincides with the first element, as shown in Fig.2.1.

Let the excitation amplitude of the m-th element be a_m and its phase $m\phi$ (where ϕ, the phase difference between an element and the next, is taken as a constant). Then the array factor can be defined as [1]

$$F(\theta)=\sum_{m=0}^{N-1} a_m e^{jm(k_0 d\cos\theta+\phi)} \tag{2.1}$$

where k_0 is the free space wavenumber, $k_0\, d\cos\theta$ is the difference between the vector contributions of successive elements, that is due to the differences in path length to the observation point.

Defining

$$\psi=k_0\, d\cos\theta+\phi \tag{2.2}$$

we can rewrite (2.1) as

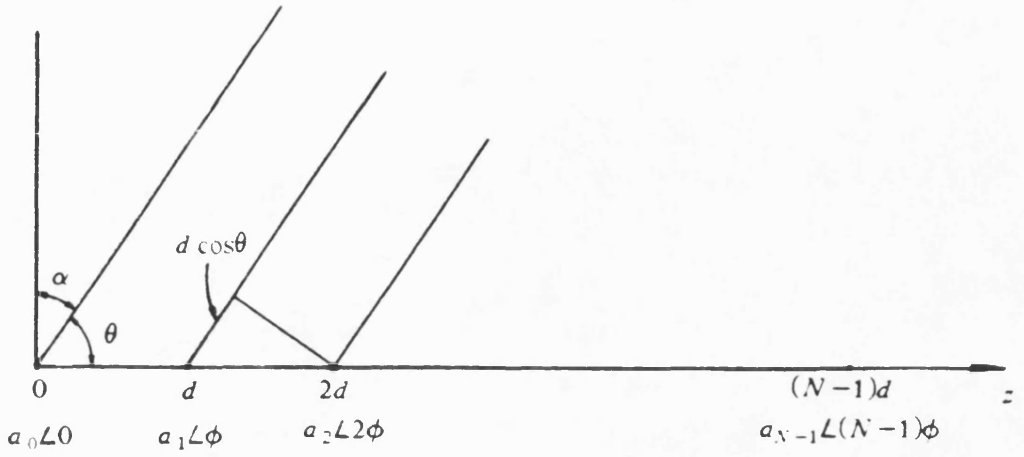

Figure 2.1 An array with progressive phaseshift

$$F(\psi)=\sum_{m=0}^{N-1} a_m e^{(jm\psi)} \tag{2.3}$$

For an array with uniform current distribution ($a_m=a$) and linear phase progression, i.e. a uniform array, the finite series in (2.3) may be summed by the formula for a geometrical progression, yielding the expression:

$$F(\psi)=a\,\frac{e^{(jN\psi)}-1}{e^{(j\psi)}-1} \tag{2.4}$$

By normalizing the amplitudes in such a way that $a=1/N$ and using Euler's formulas in (2.4), we get:

$$f(\psi)=e^{j(N-1)\psi/2}\,\frac{\sin(N\psi/2)}{N\sin(\psi/2)}$$

or

$$|f(\psi)|=\left|\frac{\sin(N\psi/2)}{N\sin(\psi/2)}\right| \tag{2.5}$$

(2.5) gives the normalized space factor of a uniform array. It indicates that for this kind of array

a) the principal maximum $|f(\psi)|=1$ occurs at

$$\psi=k_0\cos\theta+\phi=0$$

or

$$\theta=\cos^{-1}\left(-\frac{\phi}{k_0 d}\right)$$

b) the maxima of the sidelobes are obtained at

$$\frac{N\psi_{max}}{2}=\frac{2p+1}{2}\pi \qquad p=\pm1,\pm2,...$$

or

$$\theta_{max}=\cos^{-1}\left(\frac{1}{k_0 d}\left(\frac{2p+1}{N}\pi-\phi\right)\right) \tag{2.6}$$

c) the function f has its nulls at

$$\frac{N\psi_0}{2}=p\pi \qquad p=\pm1,\pm2,...$$

or

$$\theta_0=\cos^{-1}\left(\frac{1}{k_0 d}\left(\frac{2p\pi}{N}-\phi\right)\right) \tag{2.7}$$

When $\phi=0$, the array factor achieves its absolute maximum only in the direction normal to the array axis, $\theta=90^0$. This kind of array is known as 'broadside array'.

Using the change of variable $\theta=\theta_{max}-\alpha=\frac{\pi}{2}-\alpha$, as shown in Fig.2.1, (2.7) indicates that for a broadside array the first pair of nulls occur at

$$\theta_0=\cos^{-1}\left(\frac{1}{k_0 d}\frac{\pm2\pi}{N}\right)=\cos^{-1}\left(\pm\frac{\lambda_0}{Nd}\right)$$

or

$$\alpha_0=\sin^{-1}\left(\pm\frac{\lambda_0}{Nd}\right)\approx\pm\frac{\lambda_0}{L}$$

provided N is large. Then the width of the main beam is

$$2|\alpha_0|=2\frac{\lambda_0}{L} \tag{2.8}$$

Let $2\alpha_{1/2}=2\left(\frac{\pi}{2}-\theta_{1/2}\right)$ denote the half-power beamwidth, this can be found by setting

$$|f(w)|=\frac{1}{N}\frac{\sin\frac{N}{2}k_0\cos\theta_{1/2}}{\sin\frac{1}{2}k_0\cos\theta_{1/2}}\approx\frac{\sin\frac{N}{2}k_0\cos\theta_{1/2}}{\frac{N}{2}k_0\cos\theta_{1/2}}=0.707$$

Hence

$$\frac{N}{2}k_0 \cos \theta 1/2=1.39$$

or

$$\alpha_{1/2} = \sin^{-1}\frac{2.78}{Nk_0d} \approx \frac{2.78}{Nk_0d}$$

$$2\alpha_{1/2} = 0.88\,\frac{\lambda_0}{L} \tag{2.9}$$

where $L=Nd$ is the length of the array. From (2.5) and (2.6) we get the first sidelobe level:

$$SL=\left|\frac{\sin\frac{3\pi}{2}}{N\sin\frac{3\pi}{2N}}\right| \approx 0.212$$

In other words, the first sidelobe is about $13.5dB$ below the main lobe. This ratio is independent of N, as long as N is large enough for the approximation $\sin(3\pi/2N)=3\pi/2N$ to hold. Thus it is not possible to reduce the sidelobe radiation relative to the main beam below $13.5dB$ no matter how many elements we put into the array, as long as the array is uniform.

2.3 Schelkunoff's Unit Circle Representation

Defining

$$w=e^{j\psi}$$

and setting a_{N-1} equal to one, (2.3) can be written as:

$$f(w)=w^{N-1} + (a_{N-2}/a_{N-1})w^{N-2} + \cdots + a_0/a_{N-1} = P_{N-1}(w) \tag{2.10}$$

(2.10) shows that the array factor of a uniformly spaced array of N elements can be expressed as an $(N-1)$th-order polynomial of the complex variable w. It also implies that every $(N-1)$th-order polynomial can be associated with a linear array of N elements.

The variable $w=e^{j\psi}$,where $\psi=k_0\, d\cos\theta+\phi$ is a complex variable of unit magnitude. Thus, as θ varies between 0 and π, $\phi-k_0\, d \le \psi \le \phi+k_0\, d$ and w varies along the unit circle in the range:

$$e^{j(\psi-k_0\, d)} \le w \le e^{j(\phi+k_0\, d)}$$

The range of w along the unit circle corresponds to the 'visible' region and it depends on the ratio d/λ and ϕ.

Let the roots of the polynomial $P_{N-1}(w)$ be $w_1, w_2, \cdots w_{N-1}$, then

$$f(w)=(w-w_1)(w-w_2)...(w-w_{N-1}) \tag{2.11}$$

$$|f(w)| = |w-w_1|\ |w-w_2| \cdots |w-w_{N-1}| \tag{2.12}$$

The magnitude and phase angle of f now have simple geometrical interpretations. For each value of θ, $|f|$ is proportional to the product of the length of the distances $d_1, d_2, \cdots d_{N-1}$ between each zero $w_1, w_2, \cdots w_{N-1}$ and the point on the unit circle corresponding to the specified value of θ and the phase angle of f is equal to the sum of the phase angle of each factor in (2.11). To each root configuration corresponds one particular set of excitation coefficients. In general, the converse is not true. However, if all roots are on the unit circle, then there is a one-to-one correspondence between the relative variation of $|f|$ and the root configuration.

For a uniform array of N elements, the array factor (2.4) can be rewritten as:

$$f(w)=\frac{1}{N}\frac{w^N-1}{w-1}$$

By using de Moivre's theorem in the numerator, we obtain the $N-1$ roots of $f(w)=0$

$$w_m=e^{j2\pi m/N} \qquad m=1,2,...N-1 \tag{2.13}$$

The first root of w^N-1, $w=1$, is not a root of $f(w)=0$ because of cancellation with the denominator, $w-1$. In fact, $w=1$ corresponds to the direction of maximum radiation. The root positions are shown in Fig.2.2 for the case $N=5$. The array factor is simply given by

$$|f(w)| = \frac{1}{5} d_1 d_2 d_3 d_4 \tag{2.14}$$

The circle in Fig.2.2 is known as Schelkunoff's unit circle representation [2]. Its use in the synthesis of arrays will be discussed below:

From (2.14) and Fig.2.2 it is noted that, with w approximately halfway between the successive nulls w_m and w_{m+1}, the product of these distances gives the relative height of the m-th sidelobe. It follows that if these two roots are brought closer together, the height of the sidelobe will be reduced. For broadside arrays, if the heights of all the sidelobes are to be reduced, the roots must cluster closer around $-\pi$, indicating that the mainbeam region on the unit circle (from w_1 to w_{N-1}, anticlockwise) must be enlarged. In other words, the sidelobes are reduced at the expense of broadening the main beam.

Suppose it is desired to produce a pattern in which all the sidelobes are at $-20dB$. This would require that the four roots of Fig.2.2 cluster close to $-\pi$.

This design problem can be solved graphically by trial and error. At present, the roots are at $\pm 72^0$ and $\pm 144^0$ and the sidelobe level is $-13.5dB$. Suppose the new position $\pm 87^0$ and $\pm 149^0$ were tried. By drawing a unit circle with roots placed in these positions, the product of the measured distances gives the first sidelobe at $-18.5dB$ and the second at $-21.3dB$. This suggests that the roots w_2 and w_3 have been placed too close together, but that w_1 and w_4 might be just about right. After a few trials we find that, in order to obtain a pattern with $-20dB$ sidelobe level, the proper root positions are at $\pm 89^0$ and $\pm 145.5^0$. Returning to (2.11), this can now be rewritten as

$$\begin{aligned} f(w) &= (w - e^{j1.55})(w - e^{j2.54})(w - e^{-j2.54})(w - e^{-j1.55}) \\ &= w^4 + 1.6w^3 + 1.95w^2 + 1.6w + 1 \end{aligned}$$

If this polynomial is compared with (2.10) it can be observed that the relative current distribution are in the ratio

1 : 1.6 : 1.95 : 1.6 : 1

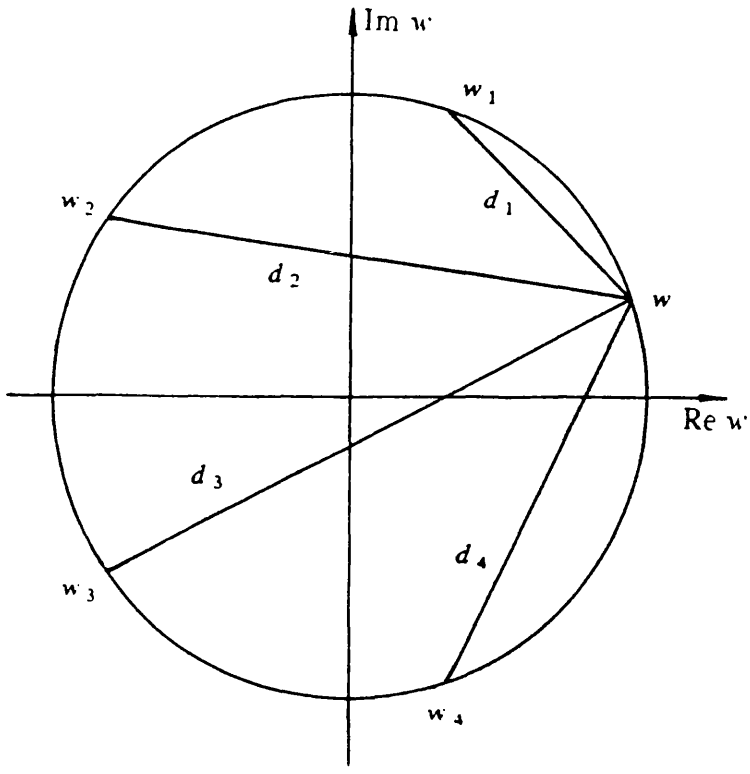

Figure 2.2 Root positions on a Schelkunoff Unit Circle
for a uniform array of 5 elements

This distribution is tapered symmetrically.

The following question naturally suggests itself. What are the location of zeros, and the current distributions for which the array will have

a) the narrowest mainlobe width for a given sidelobe level or

b) the lowest sidelobe level for a given mainlobe width?

These properties, of course, can be required from a linear equispaced array of any number of elements. The resulting current distribution is the one known as the Dolph-Chebyshev distribution.

2.4 Dolph-Chebyshev Array

A symmetrically tapered amplitude distribution is associated with a pattern having lower sidelobes then those of a uniform array. Lowering the sidelobes broadens the beamwidth and reduces the excitation efficiency. The latter is defined as the ratio of its directivity to the directivity for uniform excitation. Some improvements in both beamwidth and efficiency are obtained by raising the further-out sidelobes. Intuitively, one might expect equal-level sidelobes to be optimum for a given sidelobe level. A method of accomplishing this for a half-wave spaced broadside array was invented by Dolph, who recognized that the Chebyshev polynomials are ideally suited: in the range from -1 to $+1$ a Chebyshev polynomial oscillates with unit amplitude, while outside this range its value increases monotonically. The Chebyshev polynomial can be expressed as

$$T_N(x) = \begin{cases} (-1)^N \cosh\,(N \operatorname{arc\,cosh} |x|) & x < -1 \\ \cos\,(N \operatorname{arc\,cos} x) & |x| \le 1 \\ \cosh\,(N \operatorname{arc\,cosh} x) & x \ge 1 \end{cases} \tag{2.15}$$

The first few polynomials are,

$$T_0(x) = 1$$

$$T_1(x) = x$$

$$T_2(x) = 2x^2 - 1$$

$$T_3(x) = 4x^3 - 3x$$

$$T_4(x) = 8x^4 - 8x^2 + 1$$

They are shown in Fig.2.3. Polynomials of higher degree can be obtained from the recurrence relationship $T_{n+1}(x)=2xT_n(x)-T_{n-1}(x)$ or from the functional equation $T_{mn}(x)=T_m[T_n(x)]=T_n[T_m(x)]$

Chebyshev's polynomials have the following properties:

a) $T_N(x)$ is a polynomial of Nth degree,

b) For N even (odd) it contains even (odd) powers of x only,

c) The polynomial passes through the points (1,1) and $(-1,(-1)^N)$ and oscillates between the bounds ± 1 in the interval $|x| \le 1$,

d) For $N > 1$ the extrema are all in the interval $|x| < 1$ and occur at

$$x = \cos\left(p\frac{\pi}{N}\right), \quad p = 1,2,...N-1 \tag{2.16}$$

e) For $N > 0$ the zeros are all in the interval $|x| < 1$ and occur at

$$x = \cos\left(\frac{2p+1}{2N}\pi\right), \quad p = 0,1,2,...N-1 \tag{2.17}$$

From the fundamental lemma of algebra, we can prove that among all polynomials of degree n which pass through two given points (x_0,R) and $(x_2,0)$, $x_1 \le x_2 < x_0$, where x_1 is the largest zero of $T_n(x)$, as shown in Fig.2.4, $T_n(x)$ minimizes the largest absolute value in the interval $|x| < 1$. The opposite is also true: among all polynomials $P_n(x)$ of degree n, which pass through a given point (x_0,R) and which remain within the bounds ± 1 in the interval $|x| < 1$, the Chebyshev polynomial $T_n(x)$ minimizes the distances x_0-x_2 where x_2 is the largest zero of $P_n(x)$. These optimum properties of Chebyshev's

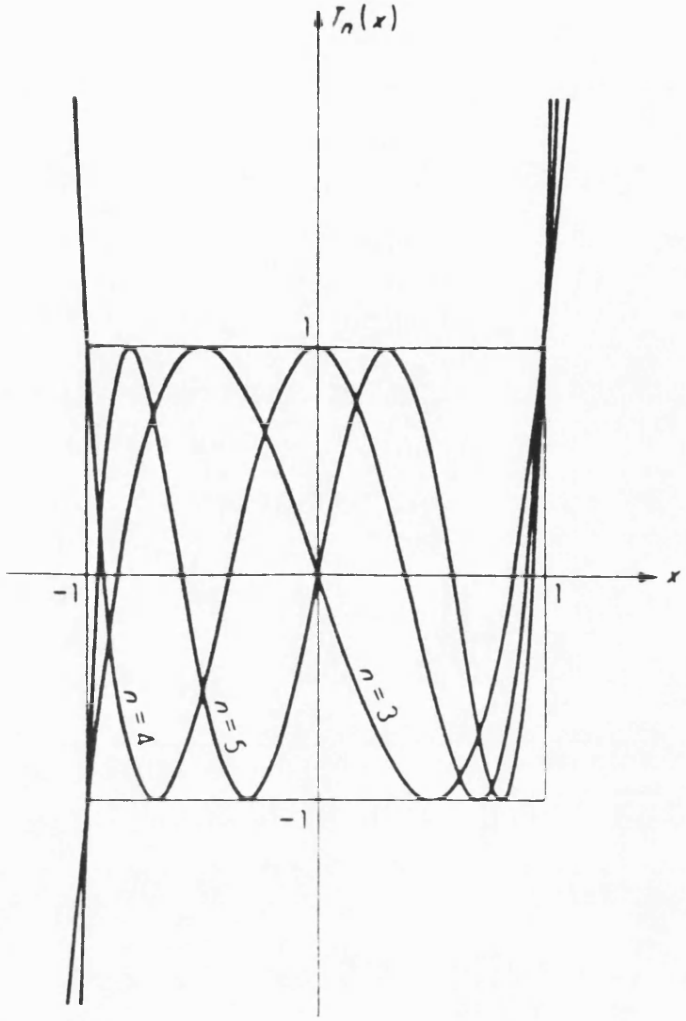

Figure 2.3 The Chebyshev polynomials $T_n(x)$ for $n = 3,4,5$

polynomial can be used in the design of optimum arrays.

As the starting point for the derivation of the Dolph-Chebyshev current distribution, we consider a symmetric excitation, i.e. excitation with $|a_m|=|a_{N-m-1}|$. It is then advantageous to let the midpoint of the array coincide with $z=0$. By numbering the elements from the center to the ends and using the parity, the array factor may now be expressed in the following way,

$$f(\psi)=\begin{cases} 2\sum_{m=1}^{N/2} |a_m| \cos\frac{2m-1}{2}\psi & N \text{ even} \\ a_0 + 2\sum_{m=1}^{(N-1)/2} |a_m| \cos m\psi & N \text{ odd} \end{cases} \tag{2.18}$$

From the trigonometric identity,

$$\cos nx = \cos^n x - C_n^2 \cos^{n-2} x \sin^2 x + C_n^4 \cos^{n-4} x \sin^4 x - \ldots.$$

we can see that function $\cos px$ can be expressed as a polynomial of degree p in $\cos x$. Consequently, (2.18) can be written as

$$f(\psi)=\begin{cases} \sum_{m=1}^{N/2} a'_m (\cos\frac{\psi}{2})^{2m-1} & N \text{ even} \\ a'_0 + \sum_{m=1}^{(N-1)/2} a'_m (\cos\frac{\psi}{2})^{2m} & N \text{ odd} \end{cases} \tag{2.19}$$

where a'_m are new coefficients. The degree of both polynomials is $N-1$. If we simply set $x=\cos(\psi/2)$, the range of x is restricted to the interval between -1 and $+1$ as ψ varies. In this interval $T_{N-1}(x)$ will oscillate between -1 and $+1$. The result is an array factor of several lobes of the same level, and there will be no main lobe. In order to get a main lobe, we set

$$x = x_0 \cos(\frac{\psi}{2}) \tag{2.20}$$

where $x_0>1$ is a parameter. Expressed in terms of the Chebyshev polynomial, the array

factor thus obtained is

$$f(\psi) = T_{N-1}\left(x_0 \cos\frac{\psi}{2}\right) \tag{2.21}$$

In order to illustrate how the transformation (2.20) works, we shall refer to a geometrical configuration shown in Fig.2.4. For a broadside array, $\psi=0$, if the element spacing d is $\lambda_0/2$, then, as θ increases from 0 to π, $\psi=k_0\, d\cos\theta$ varies from π through 0 to $-\pi$ and $x=x_0\cos(\psi/2)$ goes from 0 through x_0 to 0, as shown in Fig.2.4. In the rectangular coordinate system (x,f) and in the polar coordinate system (θ,f), the corresponding points move from A through B to C and A' through B' to C', respectively, as shown in Figs.2.4 (a) and (b). The array factor $f(\psi)$ obtained in this manner will have an absolute maximum R corresponding to a main lobe and extrema ±1 corresponding to sidelobes. The sidelobe level is $1/R$.

Now let us examine a broadside array with a fixed element number N of elements and spacing $k_0\, d$. We first consider the case when the beamwidth $2\alpha_0$ between the first pair of nulls of the pattern is specified.

The first null of the pattern corresponds to the largest zero $x_1=\cos[\pi/(2N-2)]$ of the Chebyshev polynomial $T_{N-1}(x)$. This determines the parameter x_0 in the transformation of (2.20).

$$\cos\frac{\pi}{2N-2} = x_0 \cos\frac{k_0\, d\cos\left(\frac{\pi}{2}-\alpha_0\right)}{2}$$

$$x_0 = \frac{\cos(\pi/(2N-2))}{\cos((k_0\, d\sin\alpha_0)/2)} \tag{2.22}$$

With x_0 known, the sidelobe level follows $R=T_{N-1}(x_0)$ or since $x_0>1$,

$$R = \cosh\left((N-1)\cosh^{-1}x_0\right) \tag{2.23}$$

(2.22) and (2.23) express the relationship between the prescribed beam width $2\alpha_0$ and the corresponding sidelobe level $1/R$, which, according to the optimum property of

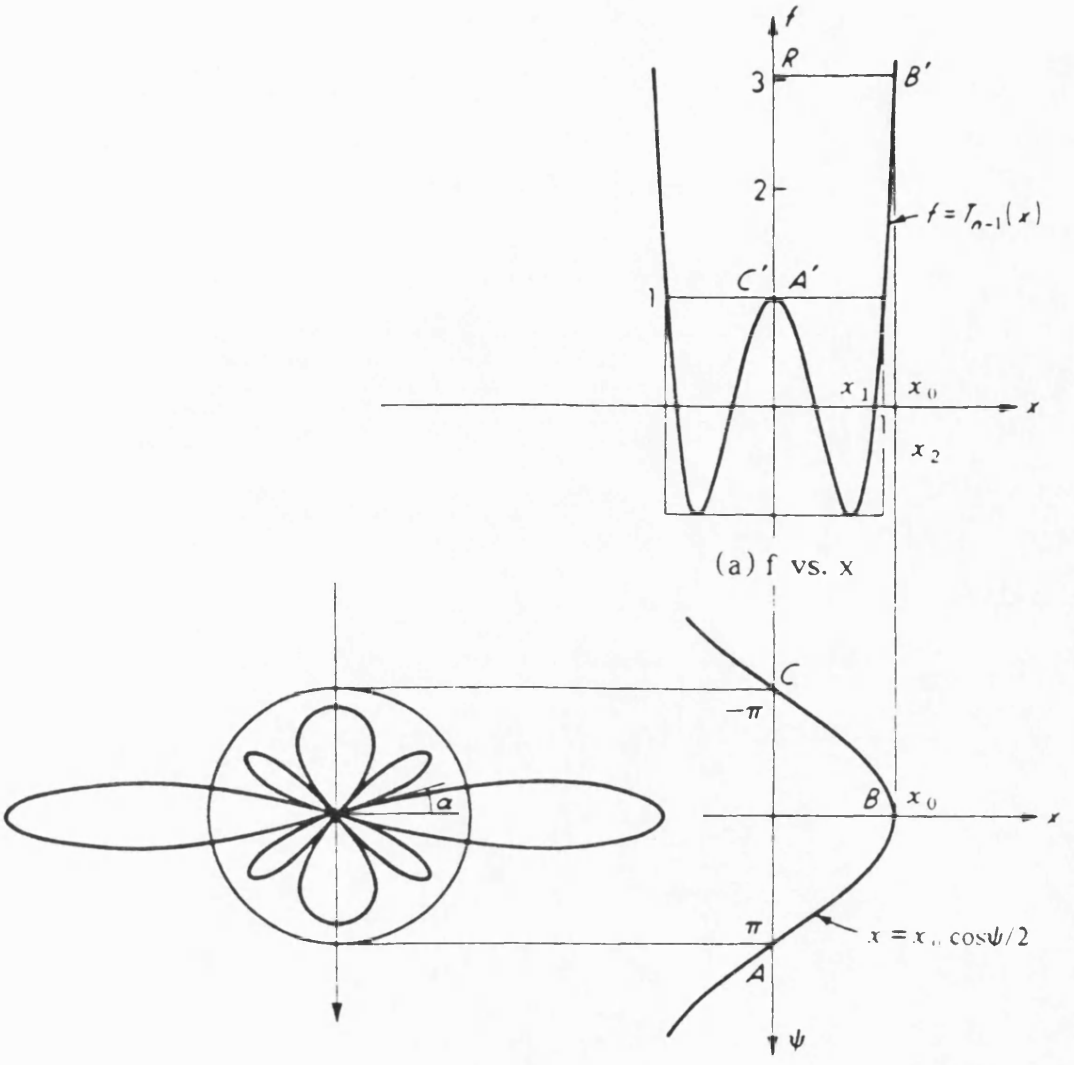

Figure 2.4 Geometrical construction of array pattern for broadside Dolph-Chebyshev array with $d = \lambda_0/2$

the Chebyshev polynomial, is as low as possible.

If, instead of the beam width, the sidelobe level $1/R$ is the required quantity, we must have

$$T_{N-1}(x_0) = R \qquad R > 1$$

The solution for this algebraic equation follows directly from (2.15)

$$x_0 = \cosh\left(\frac{1}{N-1}\cosh^{-1}R\right) \tag{2.24}$$

The optimum beam width, which goes together with the specified sidelobe level, can be obtained by solving (2.22) for α_0.

The maximum possible spacing is determined by the need to prevent x falling below -1. This gives the maximum element spacing for a broadside array as,

$$d/\lambda = \frac{\arccos(-1/x_0)}{\pi} \tag{2.25}$$

which approaches one wavelength spacing for large arrays. From (2.19) we can see the space factor is just the discrete Fourier transform of the array excitation. Therefore, the excitation a_m may be obtained from the inverse relationship. Substituting the Chebyshev polynomial representation and $R = T_{N-1}(x_0)$ we get

$$a_n = \frac{2}{N}\left[R + 2\sum_{m=1}^{(N-1)/2} T_{N-1}\left(x_0 \cos\frac{m\pi}{N}\right)\cos\frac{2nm\pi}{N}\right] \tag{2.26}$$

$$(0 \le n \le (N-1)/2)$$

for N = odd, and

$$a_n = \frac{2}{N}\left[R + 2\sum_{m=1}^{N/2-1} T_{N-1}\left(x_0 \cos\frac{m\pi}{N}\right)\cos\frac{(2n-1)m\pi}{N}\right] \tag{2.27}$$

$$(1 \le n \le N/2)$$

for N = even.

These formulas are valid for $d \geq \lambda_0/2$. Chebyshev's distribution gives the optimum pattern, but when N is large, for a practical R and α, the distribution tends toward large peaks at the array ends. Sometimes this is difficult to realize. Hence, Chebyshev's distribution is not used in practice as often as Taylor's $\bar{n}$ distribution: the latter offers more flexibility.

2.5 Taylor's Array

Taylor's array is based on the sampling of a continuous array. When the element spacing of a discrete array, d, tends to zero, the array becomes continuous, as shown in Fig.2.5. The continuous uniform array factor can be derived by assuming an excitation

$$a(z) = \begin{cases} c_0 \, e^{-j\beta z} & -l/2 \leq z \leq l/2 \\ 0 & \text{elsewhere} \end{cases} \tag{2.28}$$

The array factor, i.e. the Fourier transform of the excitation, is

$$F(\theta) = \int_{-l/2}^{l/2} a(z) \, e^{jk_0 z \cos\theta} \, dz \tag{2.29}$$

$$= 2c_0 \int_0^{l/2} \cos(k_0 z \cos\theta - \beta z) \, dz$$

$$= 2c_0 \frac{\sin\frac{l}{2}(k_0 \cos\theta - \beta)}{k_0 \cos\theta - \beta}$$

By normalizing and setting

$$u = \frac{l}{\lambda}(\cos\theta - \frac{\beta}{k_0}) \tag{2.30}$$

we obtain

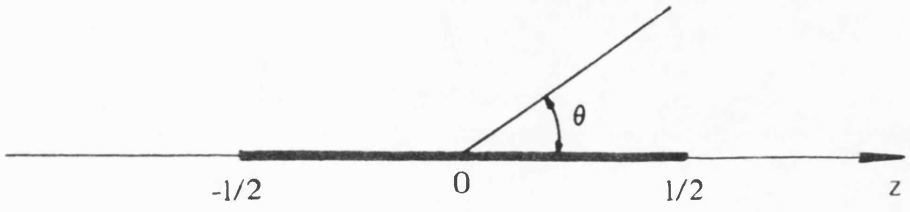

Figure 2.5 Geometry of a continuous array.

$$f(\theta) = \frac{\sin \pi u}{\pi u} \tag{2.31}$$

Where $\theta_0 = \cos^{-1}(\beta/k_0)$ is the pointing angle of the main lobe, that corresponds to $u=0$.

The array factor corresponding to the excitation

$$a(z) = \begin{cases} c_0 \cos\frac{\pi z}{l} e^{-j\beta z} & -l/2 \le z \le l/2 \\ 0 & \text{elsewhere} \end{cases} \tag{2.32}$$

is

$$F(\theta) = c_0 \int_{-l/2}^{l/2} \cos\frac{\pi z}{l} e^{j(k_0 z \cos\theta - \beta z)}\, dz \tag{2.33}$$

$$= c_0 \int_{-l/2}^{l/2} \cos\frac{\pi z}{l} \cos(k_0 z \cos\theta - \beta z)\, dz$$

$$= c_0 \frac{2l}{\pi} \frac{\cos \pi u}{1-(2u)^2}$$

$$f(\theta) = \frac{\cos \pi u}{1-(2u)^2} \tag{2.34}$$

The two patterns expressed by (2.31) and (2.34) are shown in Fig.2.6. The first pair of zeros of the tapered array is at $u = \pm\frac{3\pi}{2}$, ($u=\pm\pi$ for a uniform array), the first sidelobe level is $-23dB$ ($-13.5dB$ for a uniform array). It can be seen again that the tapering of the excitation affects the positions of the zeros, and consequently affects the pattern (width of the main beam and the level of sidelobes).

The pattern of (2.31) shows symmetrical sidelobes whose heights trail off as u^{-1}, the closest pair of sidelobes being $13.5dB$ down. As θ moves from 0 through θ_0 to π, u moves from $\frac{l}{\lambda}(1-\frac{\beta}{k_0})$ through 0 to $\frac{l}{\lambda}(-1-\frac{\beta}{k_0})$. The number of sidelobes in the "visible" range of u thus depends on the aperture length l/λ. All of this is consistent with the theory of discrete linear array. What Taylor sought was to find a way of depressing the $\bar{n}$ innermost sidelobes on each side of the main beam to a common height while leaving

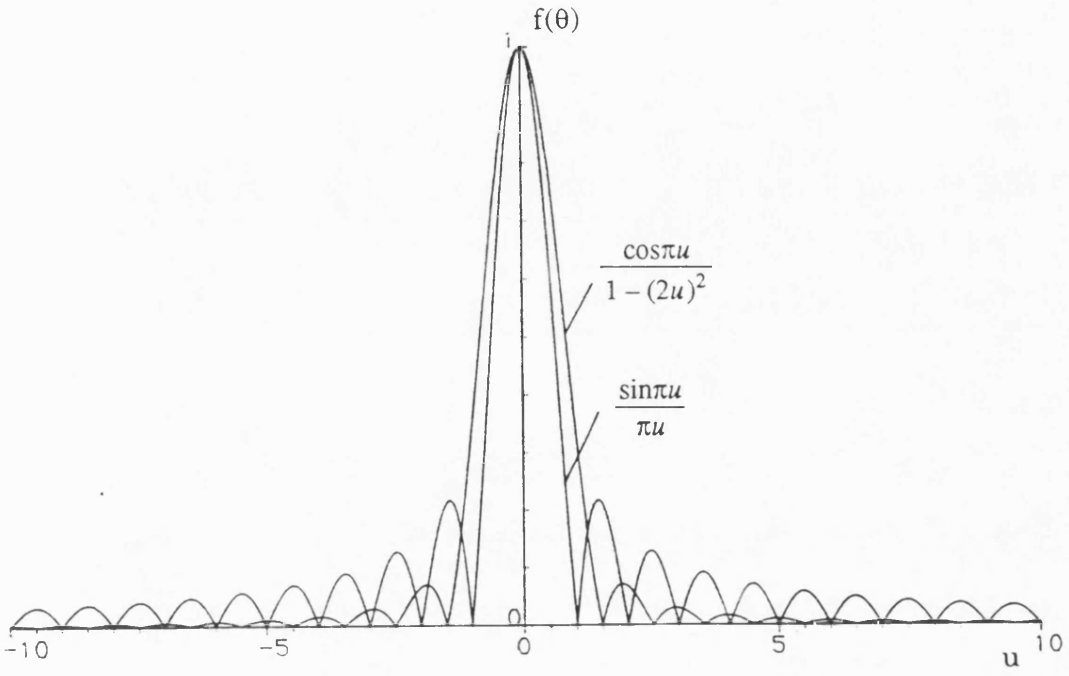

Figure 2.6 The patterns of $\frac{\sin\pi u}{\pi u}$ and $\frac{\cos\pi u}{1-(2u)^2}$

alone all the sidelobes that are further-out. In order to satisfy both requirements, the nulls of the new pattern are to occur at integer values of u for $|u| \geq \bar{n}$. For $|u| < \bar{n}$, the nulls will be needed at [3]

$$u_n = \pm\sigma\sqrt{A^2 + (n - 1/2)^2} \tag{2.35}$$

Where $\sqrt{A^2 - (n - 1/2)^2}$ is the position of the n-th null of the continuous Chebyshev array,

$$A = \frac{1}{\pi}\text{arc cosh}R = \frac{1}{\pi}\ln(R + \sqrt{R^2 - 1}) \tag{2.36}$$

and σ is a parameter given by

$$\sigma = \bar{n}(A^2 + (\bar{n} - 1/2)^2)^{-1/2} \tag{2.37}$$

The new pattern can be expressed by

$$f(u) = \frac{\sin\pi u}{\pi u}\frac{\prod_{n=1}^{\bar{n}-1}(1 - u^2/u_n^2)}{\prod_{n=1}^{\bar{n}-1}(1 - u^2/n^2)} \tag{2.38}$$

With a Taylor pattern, as defined by (2.35) and (2.38), it becomes a simple matter to find the corresponding aperture distribution from (2.29). Setting $a(z) = h(z)e^{-j\beta z}$ with $h(z)$ represented by the Fourier series

$$h(z) = \sum_{m=0}^{\infty} B_m \cos\frac{2m\pi z}{l} \tag{2.39}$$

and substituting into (2.29) we find

$$f(u) = \sum_{m=0}^{\infty} B_m \int_{-l/2}^{l/2} \cos\frac{2m\pi z}{l} e^{j(k_0 z\cos\theta - \beta z)}\, dz$$

$$= \sum_{m=0}^{\infty} B_m \int_{-l/2}^{l/2} \cos\frac{2m\pi z}{l}\cos\frac{2n\pi z}{l}\, dz$$

From the orthonormalization

$$\int_{-l/2}^{l/2} \cos\frac{2m\pi z}{l}\cos\frac{2n\pi z}{l}\,dz = \begin{cases} l & n=m=0 \\ l/2 & n=m\neq 0 \\ 0 & n\neq m \end{cases}$$

We obtain

$$f(m) = \delta_m l\, B_m \tag{2.40}$$

where

δ_m=1 when m=0

δ_m=1/2 m=1,2,...

However, (2.38) indicates that

$$f(m) = \frac{\sin\pi m}{\pi m}\frac{\prod_{n=1}^{\bar{n}-1}(1-m^2/u_n^2)}{\prod_{n=1}^{\bar{n}-1}(1-m^2/n^2)} = 0$$

when $m \geq \bar{n}$. Hence, this Fourier series is truncated, and thus the continuous aperture distribution is given by

$$a(z) = \frac{e^{-j\beta z}}{l}[f(0) + 2\sum_{m=1}^{\bar{n}-1} f(m)\cos\frac{2m\pi z}{l}]$$

$$|a(z)| = \frac{1}{l}[f(0) + 2\sum_{m=1}^{\bar{n}-1} f(m)\cos\frac{2m\pi z}{l}] \tag{2.41}$$

By sampling the continuous aperture distribution at $z_n = -\frac{l}{2} + \frac{nl}{N-1}(n=0,N-1)$, we find the distribution for a discrete array of N elements. The f(m) in (2.41) can be found from

$$f(m) = \begin{cases} \dfrac{((\bar{n}-1)!)^2}{(\bar{n}-1+m)!\,(\bar{n}-1-m)!}\prod_{n=1}^{\bar{n}-1}(1-\dfrac{m^2}{z_n^2}) & m < \bar{n} \\ 0 & m \geq \bar{n} \end{cases} \tag{2.42}$$

An aperture distribution computed from (2.41) is shown in Fig.2.7. For comparison, the Dolph excitation for a 13 element discrete array is shown as well.

The half-power beamwidth for a Taylor contribution is [4]

$$2\alpha_{1/2} \approx 2\sin^{-1}\left\{\frac{\lambda\sigma}{L\pi}[(\cosh^{-1}R)^2 - (\cosh^{-1}\frac{R}{\sqrt{2}})^2]\right\} \tag{2.43}$$

2.6 Realization of the Aperture Distribution

After getting the aperture distribution, our next step is to realize it physically.

The normalized conductance of the n-th element can be defined as:

$$g_n = \frac{P_{rn}}{P_{in}} \tag{2.44}$$

where P_{rn} and P_{in} are respectively the power radiated from and incident on the n-th element. g_n measures the radiation loss of n-th element. P_{in} can be written as: [5]

$$P_{in} = \delta^{n-1}(1-\sum_{k=1}^{n-1} P_{rk}\delta^{1-k}) \tag{2.45}$$

In (2.45), δ is a parameter representing the loss of a section of transmission line between two adjacent elements.

The power weight function of the nth element is defined as:

$$W_n = a_n^2/(\sum_{m=1}^{N} a_m^2) \tag{2.46}$$

Obviously

$$\sum_{n=1}^{N} W_n = 1$$

Setting

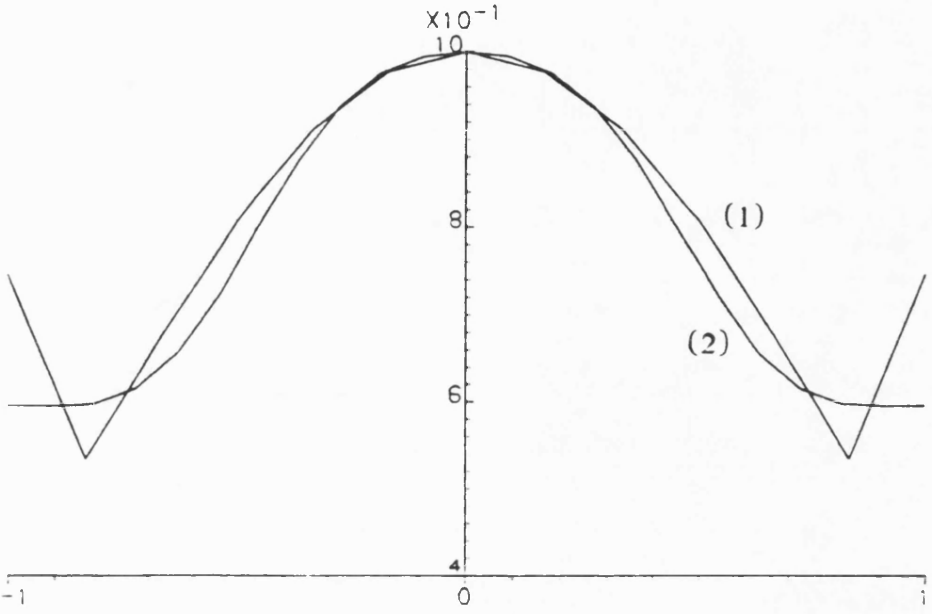

Figure 2.7 A comparison between the two aperture distributions.
(1) Chebyshev array distribution, N=13.
(2) Taylor array distribution, $\bar{n}$ =4, N=23.

$$\mu W_n = P_{rn} \tag{2.47}$$

then the efficiency of the array, μ, is given by

$$\mu = (1-p_0/\delta^{N-1})/(\sum_{k=1}^{N} W_k/\delta^{k-1}) \tag{2.48}$$

Where P_0 is the power dissipated into the load, which depends on the number of elements, the realizability of the element radiation loss, etc. Substituting (2.45) and (2.47) into (2.44) we get

$$g_n = \mu W_n/(\delta^{n-1}(1-\sum_{k=1}^{n-1} \mu W_k \delta^{1-k})) \tag{2.49}$$

Fig.2.8 shows a distribution of normalized conductance, in which $P_0 = 0.17$, $\bar{n} = 4$, $N = 23$, $R = -20dB$.

We are using this theory to realize an array on *IDG*. A relationship between normalized conductance and the dipole lengths is developed in Chapter 5. With the date given in Fig.2.8, a 23-element array is built. The experimental result is in excellent agreement with the theory.

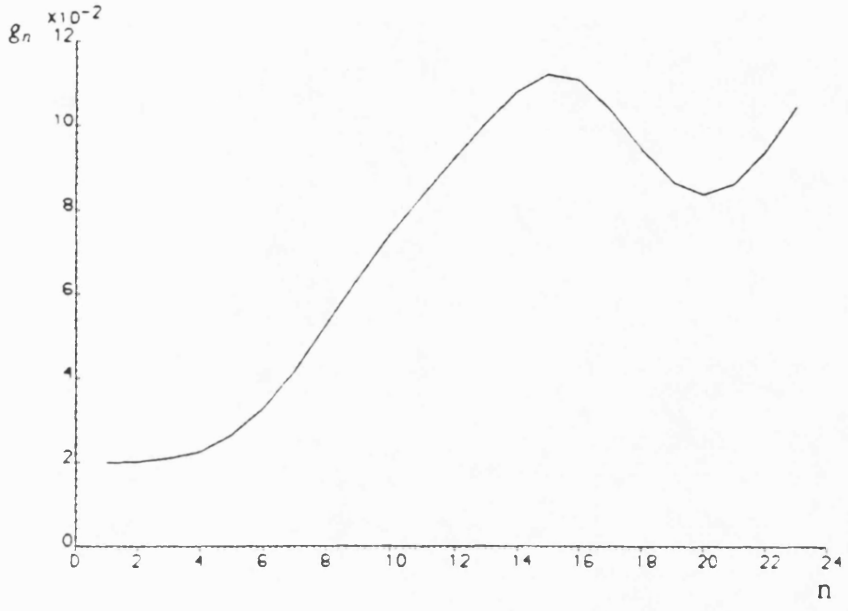

Figure 2.8 The distribution of the normalised conductance for a 23-element Taylor array.

REFERENCES

[1] C. A. Balanis, *Antenna Theory Analysis* and *Design.* New York: Harper & Row, Publishers, 1982.

[2] Samuel Silver, *Microwave Antenna Theory* and *Design.* Peter Peregrinus Ltd, 1984.

[3] A. W. Rudge etc, *The Handbook of Antenna Design.* Vol. 2 Peter Peregrinus Ltd, 1983.

[4] Warren L. Stutzman and Gary A. Thiele, *Antenna Theory* and *Design.* John Wiley & Sons, 1981.

[5] Francis M. Gray, *Design of a Narrow Wall Transverse Slotted Waveguide Array at 70GHz* 30 Sept. 1963, Harry Diamond Lab., Army Material Command, USA.

CHAPTER 3

A RIGOROUS FULL HYBRID ANALYSIS OF INSET DIELECTRIC GUIDE

3.1 Introduction

The Inset Dielectric Guide (*IDG*) is an easy-to-fabricate alternative to the image line, less sensitive to loss by radiation at discontinuities. The *IDG* structure has been analyzed by Zhou and Itoh [1] as an intermediate structure in the analysis of trapped image guide. They made an approximate analysis in which the wave equation is solved for region I and II using separation of variables and the two solutions are fitted at the air-dielectric interface as shown in Fig.3.1. Regions III are ignored. It is a reasonable approximation for the fundamental mode, where the field is well confined to the dielectric. The singularity imposed on the field by the 90^0 metal edges, however, causes diffraction, which is important for the accurate evaluation of the field distribution and propagation loss. A rigorous full hybrid analysis and a network modeling of *IDG* have been given by Rozzi and Hedges [2], which yield an accurate equivalent circuit for the discrete modes. This analysis considered mainly the even-mode solutions with respect to x. This chapter retraces the method and extends the analysis to odd parity.

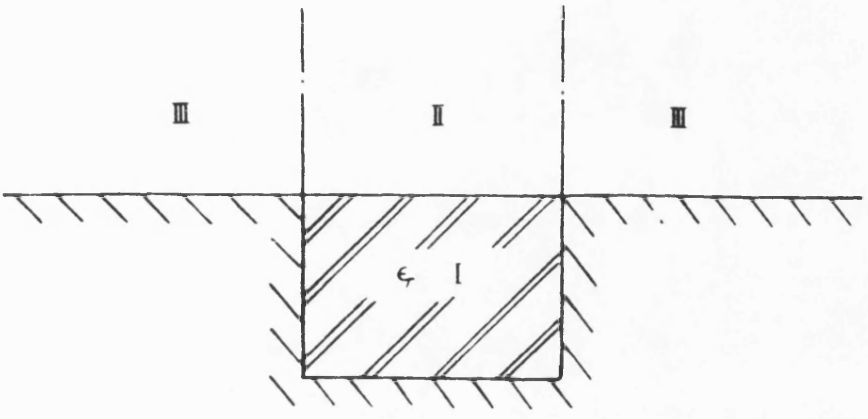

Figure3.1 Cross-section of *IDG*.

In recent years, the spectral-domain approach developed by Itoh [3] has been preferred over the space-domain approach for the numerical solution of boundary value problems. In both approaches, the fields are derived from potential functions, which, along with the necessary boundary conditions, can be formulated into sets of integral equations that can be solved for the propagation constant.

In the space-domain approach, these integrals are solved directly by Galerkin's method, the unknown functions being expanded by a suitable set of basis functions. In the spectral-domain approach, the integral equations are transformed into the Fourier domain prior to solution by Galerkin's method. The advantage of the latter method is that the integral equation is often easier to formulate, the Green functions often being found by inspection. However, the choice of expansion sets required for solution in the Fourier domain is restricted by the requirement that they have simple Fourier transforms. Thus, functions that do not accurately model the edge conditions are sometimes used, which results in slow convergence rate.

The approach outlined in this chapter is a space-domain approach. Unlike the spectral-domain approach, there is no restriction on the choice of expansion functions. In fact, the functions used are particularly accurate in that they take into account the singularity imposed on the guide field by the 90^0 metal edges. The problem is formulated so that only one set of basis functions is required, which results in a further increase in accuracy. As a result, the convergence is very rapid, and often only the first term of the expansion is sufficient.

3.2 Formulation of Admittance Operators

The coordinate system used in this analysis is shown, along with the guide structure, in Fig.1.1. For each homogeneous region, we may write

$$\varepsilon_r k_0^2 = k_x^2 + k_y^2 + \beta^2 \tag{3.1}$$

where β is the z-directed propagation constant to be determined. For such a composite structure it is easier to solve for propagation in a direction perpendicular to the dielectric interface, i.e., the y-direction.

From the boundary conditions and Maxwell's equations, integral equations for the transverse field components are set up. In order that they are solved on a computer, they are transformed by Galerkin's technique into scalar equations. In this approach, the integral equations are transformed into the space spanned by the set of functions used to discretize the unknown field components E_x and E_z. These functions are chosen to model as accurately as possible the field components so that few terms are needed for adequate convergence. This includes taking into account the diffraction of the field due to the presence of the 90^0 metal edges at $x=\pm a/2$, $y=0$. This diffraction due to the metal edges results in a hybrid mode structure. Thus a full six-field analysis is required. The six field components can be obtained from the superposition of *LSE* and *LSM*-modes. For propagation in the y direction, these appear to be y-directed *TE* and *TM*-modes. Thus, the hybrid mode can be derived from y-directed electric and magnetic Hertzian vector potentials, Π_e and Π_h.

These are of the form

$$\Pi_e = \mathbf{y}\, \psi_e(x,y)\, e^{-j\beta z} \tag{3.2a}$$

$$\Pi_h = \mathbf{y}\, \psi_h(x,y)\, e^{-j\beta z} \tag{3.2b}$$

where $\mathbf{y}$ is the unit vector in the y direction. From the potentials, the fields are derived

by

$$\mathbf{E} = -j\omega\mu_0 \nabla\times\Pi_h + \varepsilon_r k_0^2 \Pi_e + \nabla \nabla \cdot \Pi_e \tag{3.3a}$$

$$\mathbf{H} = j\omega\varepsilon_0\varepsilon_r \nabla\times\Pi_e + \varepsilon_r k_0^2 \Pi_h + \nabla \nabla \cdot \Pi_h \tag{3.3b}$$

or, componentwise, suppressing the z-dependence $e^{-j\beta z}$

$$H_y(x,y) = (\varepsilon_r k_0^2 + \partial_y^2)\, \psi_h(x,y) \tag{3.4a}$$

$$E_y(x,y) = (\varepsilon_r k_0^2 + \partial_y^2)\, \psi_e(x,y) \tag{3.4b}$$

$$E_x(x,y) = \partial_x \partial_y\, \psi_e(x,y) + \omega\, \mu_0\, \beta\, \psi_h(x,y) \tag{3.4c}$$

$$E_z(x,y) = -j\beta\, \partial_y\, \psi_e(x,y) - j\omega\mu_0\, \partial_x\, \psi_h(x,y) \tag{3.4d}$$

$$H_x(x,y) = -\omega\, \varepsilon\, \beta\, \psi_e(x,y) + \partial_x\, \partial_y\, \psi_h(x,y) \tag{3.4e}$$

$$H_z(x,y) = j\, \omega\, \varepsilon\, \partial_x\, \psi_e(x,y) - j\beta\, \partial_y\, \psi_h(x,y) \tag{3.4f}$$

The scalar $\psi_e(x,y)$ and $\psi_h(x,y)$ must be chosen to satisfy the correct boundary conditions for the field components and have dimensional consistency.

The *IDG* structure can be considered to be a dielectric-filled rectangular waveguide with one of the side wall removed. Hence, the field in the slot can be constructed from the superposition of discrete waveguide mode functions. In the air region, of course, a continuous spectrum is possible. The field in each region will thus have to be derived from separate sets of potential functions, which must be continuous across the interface between the two regions.

For convenience, from now on in this thesis all the quantities having dimension of length will be normalized in units of the width of the guide, a, and all the wavenumber quantities will be normalized in units of 1/a. Therefore the coordinates of the metal edges are (±1/2, 0).

The admittance operators are formulated from the transverse equivalent circuit. For propagation in the y direction, the slot appears as a short-circuited dielectric-filled parallel-plate waveguide radiating into free space. The potential functions are chosen as

follows.

In the slot region,

$$\psi_e(x,y) = \sum_n \frac{I'_n}{j\,\omega\varepsilon_0\varepsilon_r} \frac{1}{((n\pi)^2 + \beta^2)^{1/2}} \phi_{en}(x) \frac{\cos q_n(y+h)}{\cos q_n h} \tag{3.5a}$$

$$\psi_h(x,y) = \sum_n \frac{V''_n}{j\,\omega\mu_0} \frac{1}{((n\pi)^2 + \beta^2)^{1/2}} \phi_{hn}(x) \frac{\sin q_n(y+h)}{\sin q_n h} \tag{3.5b}$$

where the x-dependence for even-modes is

$$\phi_{hn}(x) = 2\delta_n \cos(n\pi x) \qquad \phi_{en}(x) = 2\sin(n\pi x) \tag{3.6}$$

$$\delta_n = 1/\sqrt{2} \qquad n = 0$$

$$\delta_n = 1 \qquad n = 2,4,6...$$

for odd-modes are

$$\phi_{hn}(x) = 2\sin(n\pi x) \qquad \phi_{en}(x) = 2\cos(n\pi x) \tag{3.7}$$

$$n = 1,3,5,...$$

and the conservation of wavenumber gives

$$\varepsilon_r k_0^2 = q_n^2 + (n\pi)^2 + \beta^2 \tag{3.8}$$

In the air region,

$$\psi_e(x,y) = \int_0^\infty dk_x \frac{I'(k_x)}{j\omega\varepsilon_0} \frac{1}{(k_x^2 + \beta^2)^{1/2}} \phi_e(x,k_x)\, e^{-jk_y y} \tag{3.9a}$$

$$\psi_h(x,y) = \int_0^\infty dk_x \frac{V''(k_x)}{j\omega\mu_0} \frac{1}{\sqrt{k_x^2 + \beta^2}} \phi_h(x,k_x)\, e^{-jk_y y} \tag{3.9b}$$

where

$$\phi_h(x,k_x) = \sqrt{2/\pi}\cos k_x x \qquad \phi_e(x,k_x) = \sqrt{2/\pi}\sin k_x x \tag{3.10}$$

for even-modes and

$$\phi_h(x,k_x) = \sqrt{2/\pi}\ \sin k_x x \qquad \phi_e(x,k_x) = \sqrt{2/\pi}\ \cos k_x \tag{3.11}$$

for odd-modes. The conservation of wavenumber gives

$$k_0^2 = k_y^2 + k_x^2 + \beta^2 \tag{3.12}$$

The orthogonal sets $\phi_{hn}(x)$ and $\phi_h(x,k_x)$ are normalized so that

$$\int_0^{1/2} \phi_{hn}(x)\, \phi_{hm}(x)\, dx = \delta_{nm} \tag{3.13a}$$

$$\int_0^{\infty} \phi_h(x,k_x)\, \phi_h(x,k_x')\, dx = \delta\,(k_x - k_x') \tag{3.13b}$$

The amplitude functions are chosen for the sake of convenience and in order to give the unknown amplitudes V_n'' and I_n' the dimensions of a voltage and current, respectively. This will become useful when circuit analogies are made.

By placing the potential functions (3.5) into (3.4), the field components in the slot can be found to be

$$E_x\,(x,y) = \sum_n E_{xn}\phi_{hn}(x)\ \frac{\sin q_n(y+h)}{\sin q_n h} \tag{3.14a}$$

$$E_y\,(x,y) = \sum_n E_{yn}\phi_{en}(x)\ \frac{\cos q_n(y+h)}{\cos q_n h} \tag{3.14b}$$

$$E_z\,(x,y) = \sum_n E_{zn}\phi_{en}(x)\ \frac{\sin q_n(y+h)}{\sin q_n h} \tag{3.14c}$$

$$H_x\,(x,y) = \sum_n H_{xn}\phi_{en}(x)\ \frac{\cos q_n(y+h)}{\cos q_n h} \tag{3.14d}$$

$$H_y\,(x,y) = \sum_n H_{yn}\phi_{hn}(x)\ \frac{\sin q_n(y+h)}{\sin q_n h} \tag{3.14e}$$

$$H_z\,(x,y) = \sum_n H_{zn}\phi_{hn}(x)\ \frac{\cos q_n(y+h)}{\cos q_n h} \tag{3.14f}$$

where the amplitudes are:

$$E_{xn} = \left(\pm \frac{I_n'}{\omega \varepsilon_0 \varepsilon_r} q_n (n\pi) \tan q_n h - j\beta V_n'' \right) \frac{1}{((n\pi)^2 + \beta^2)^{1/2}} \tag{3.15a}$$

$$E_{yn} = -j \frac{I_n'}{\omega \varepsilon_0 \varepsilon_r} ((n\pi)^2 + \beta^2)^{1/2} \tag{3.15b}$$

$$E_{zn} = \left(\frac{I_n'}{\omega \varepsilon_0 \varepsilon_r} \beta q_n \tan q_n h \pm V_n'' n\pi \right) \frac{1}{((n\pi)^2 + \beta^2)^{1/2}} \tag{3.15c}$$

$$H_{xn} = \left(j I_n' \beta \pm j \frac{V_n''}{\omega \mu_0} (n\pi) q_n \cot q_n h \right) \frac{1}{((n\pi)^2 + \beta^2)^{1/2}} \tag{3.15d}$$

$$H_{yn} = -j \frac{V_n''}{\omega \mu_0} ((n\pi)^2 + \beta^2)^{1/2} \tag{3.15e}$$

$$H_{zn} = \left(\pm I_n' (n\pi) - \frac{V_n''}{\omega \mu_0} \beta q_n \cot k_n h \right) \frac{1}{((n\pi)^2 + \beta^2)^{1/2}} \tag{3.15f}$$

It is noted that the difference of ϕ_{en} and ϕ_{hn} between even- and odd-mode only causes the signs of the terms containing ∂_x in (3.4) different. The upper and lower signs refer to the even- and odd-mode, respectively.

By rearranging (3.15) the amplitudes for the transverse electric fields E_{xn} and E_{zn} can be written as

$$\begin{bmatrix} E_{xn} \\ E_{zn} \end{bmatrix} = \frac{1}{((n\pi)^2 + \beta^2)^{1/2}} \begin{bmatrix} \pm n\pi & -j\beta \\ -j\beta & \pm n\pi \end{bmatrix} \begin{bmatrix} j \frac{q_n}{\omega \varepsilon_0 \varepsilon_r} \tan q_n h & 0 \\ 0 & 1 \end{bmatrix} \begin{bmatrix} I_n' \\ V_n'' \end{bmatrix} \tag{3.16}$$

If an angle θ is defined such that

$$\cos\theta = \frac{n\pi}{((n\pi)^2 + \beta^2)^{1/2}} \qquad \sin\theta = \frac{\beta}{((n\pi)^2 + \beta^2)^{1/2}} \tag{3.17}$$

then (3.16) can be rewritten as

$$\begin{bmatrix} E_{xn} \\ E_{zn} \end{bmatrix} = T_n \begin{bmatrix} Z_n' & 0 \\ 0 & 1 \end{bmatrix} \begin{bmatrix} I_n' \\ V_n'' \end{bmatrix} \tag{3.18}$$

where

$$Z_n' = j \frac{q_n}{\omega \varepsilon_0 \varepsilon_r} \tan q_n h$$

$$= j Z_{0n}' \tan q_n h \tag{3.19}$$

and

$$T_n = \begin{bmatrix} \pm\cos\theta & -j\sin\theta \\ -j\sin\theta & \pm\cos\theta \end{bmatrix} \tag{3.20}$$

Similarly we obtain

$$\begin{bmatrix} H_{zn} \\ -H_{xn} \end{bmatrix} = T_n \begin{bmatrix} 1 & 0 \\ 0 & Y_n'' \end{bmatrix} \begin{bmatrix} I_n' \\ V_n'' \end{bmatrix} \tag{3.21}$$

where

$$Y_n'' = -j \frac{q_n}{\omega\mu_0} cot\, q_n h$$

$$= -j Y_{0n}'' cot\, q_n h \tag{3.22}$$

(3.18) and (3.21) can be combined to give

$$\begin{bmatrix} H_{zn} \\ -H_{xn} \end{bmatrix} = T_n \begin{bmatrix} Y_n' & 0 \\ 0 & Y_n'' \end{bmatrix} T_n^{-1} \begin{bmatrix} E_{xn} \\ E_{zn} \end{bmatrix} \tag{3.23}$$

An analogous expression for the air region is

$$\begin{bmatrix} -h_z(k_x) \\ h_x(k_x) \end{bmatrix} = T(k_x) \begin{bmatrix} Y'(k_x) & 0 \\ 0 & Y''(k_x) \end{bmatrix} T^{-1}(k_x) \begin{bmatrix} e_x(k_x) \\ e_z(k_x) \end{bmatrix} \tag{3.24}$$

where

$$\cos\theta = \frac{k_x}{(k_x^2 + \beta^2)^{1/2}} \qquad \sin\theta = \frac{\beta}{(k_x^2 + \beta^2)^{1/2}}$$

$$Y'(k_x) = \frac{\omega \varepsilon_0}{k_y(k_x)} \qquad Y''(k_x) = \frac{k_y(k_x)}{\omega\mu_0} \tag{3.25}$$

The signs in (3.23) and (3.24) come from the different orientation of the Poynting Vector, i.e., for the power flow into the slot region,

$$P_{down} = E_x H_z - E_z H_x$$

for the air region

$$P_{up} = -E_x H_z + E_z H_x$$

It is desired that the electric fields transverse to y be retained as the unknown quantities, whereas the two remaining quantities transverse to y, i.e., H_z, H_x, be expressed in terms of the above two. A linear transformation can be written compactly by means of linear integral operators acting on the fields $E_x(x, 0)$, $E_z(x, 0)$ to give the field $H_z(x, 0)$, namely

$$\begin{aligned} H_z(x, 0) &= \int_0^{1/2} y_{11}(x,x',y=y'=0)\, E_x(x',0)\, dx' \\ &\quad + \int_0^{1/2} y_{12}(x,x',y=y'=0)\, E_z(x',0)\, dx' \\ &\equiv \hat{y}_{11} E_x + \hat{y}_{12} E_z \end{aligned} \tag{3.26}$$

and similarly for $H_x(x, 0)$. Analogous expressions hold in the air region. Thus we obtain for each region integral equations of the type

$$\begin{bmatrix} H_z(x, 0^-) \\ -H_x(x, 0^-) \end{bmatrix} = \begin{bmatrix} \hat{y}^s_{11} & \hat{y}^s_{12} \\ \hat{y}^s_{21} & \hat{y}^s_{22} \end{bmatrix} \begin{bmatrix} E_x(x, 0^-) \\ E_z(x, 0^-) \end{bmatrix} \tag{3.27}$$

and

$$\begin{bmatrix} -H_z(x, 0^+) \\ H_x(x, 0^+) \end{bmatrix} = \begin{bmatrix} \hat{y}^a_{11} & \hat{y}^a_{12} \\ \hat{y}^a_{21} & \hat{y}^a_{22} \end{bmatrix} \begin{bmatrix} E_x(x, 0^+) \\ E_z(x, 0^+) \end{bmatrix} \tag{3.28}$$

where the superscripts s and a refer to the slot and air region, respectively.

To illustrate the formulation of the Green admittance operators consider the derivation of $\hat{y}^s_{11}$ in (3.27) defined as:

$$H_z(x, 0) = \int_0^{1/2} y^s_{11}(x,x';y=y'=0)\, E_x(x',0)\, dx' \Big|_{E_z(x',0)=0} \tag{3.29}$$

From (3.23) with E_{zn} set to zero,

$$H_{zn} = E_{xn}(Y_n' \cos^2\theta + Y_n'' \sin^2\theta) \tag{3.30}$$

However from (3.14)

$$E_{xn} = \int_0^{1/2} E_x(x',0)\, \phi_{hn}(x')\, dx' \tag{3.31}$$

and so substituting (3.30) and (3.31) into (3.14f)

$$H_z(x, 0) = \sum_n \int_0^{1/2} E_x\, (Y_n' \cos^2\theta + Y_n'' \sin^2\theta)\, \phi_{hn}(x)\, \phi_{hn}(x') \tag{3.32}$$

Comparing (3.32) and (3.29) gives

$$y_{11}^s(x,x') = \sum_n (Y_n' \cos^2\theta + Y_n'' \sin^2\theta)\, \phi_{hn}(x)\, \phi_{hn}(x') \tag{3.33a}$$

The other slot admittances are found in a similar manner to be

$$y_{12}^s(x,x') = \pm j \sum_n (Y_n' - Y_n'') \sin\theta \cos\theta\, \phi_{hn}(x)\, \phi_{en}(x') \tag{3.33b}$$

$$y_{21}^s(x,x') = -y_{12}^s \tag{3.33c}$$

$$y_{22}^s(x,x') = \sum_n (Y_n' \sin^2\theta + Y_n'' \cos^2\theta)\, \phi_{en}(x)\, \phi_{en}(x') \tag{3.33d}$$

In order that both unknowns can be expressed in terms of the same set of functions, we require that they display the same x-dependence. This will be so if, instead of $E_z(x, 0)$, the problem is formulated in terms of $dE_z(x, 0)/dx$. As an added bonus, proper convergence of the admittance operators will also result from this transformation. Thus, by integration by parts of (3.27), we obtain

$$\begin{bmatrix} H_z(x, 0^-) \\ -\int_0^{1/2} H_x(x, 0^-)dx \end{bmatrix} = \begin{bmatrix} \hat{Y}_{11}^s & \hat{Y}_{12}^s \\ \hat{Y}_{21}^s & \hat{Y}_{22}^s \end{bmatrix} \begin{bmatrix} E_x(x, 0^-) \\ dE_z(x, 0^-)/dx \end{bmatrix} \tag{3.34a}$$

$$\begin{bmatrix} -H_z(x, 0^+) \\ \int_0^{\infty} H_x(x, 0^+)dx \end{bmatrix} = \begin{bmatrix} \hat{Y}_{11}^a & \hat{Y}_{12}^a \\ \hat{Y}_{21}^a & \hat{Y}_{22}^a \end{bmatrix} \begin{bmatrix} E_x(x, 0^+) \\ dE_z(x, 0^+)/dx \end{bmatrix} \tag{3.34b}$$

where

$$Y_{11} = y_{11} \qquad Y_{12} = -\int y_{12}\, dx'$$

$$Y_{21} = \int y_{21}\, dx \qquad Y_{22} = -\iint y_{22}\, dx\, dx'$$

i.e.

$$Y^s_{11}(x,x') = \sum_n (Y_n' \cos^2\theta + Y_n'' \sin^2\theta)\, \phi_{hn}(x)\, \phi_{hn}(x') \tag{3.35a}$$

The other slot admittances are found in a similar manner to be

$$Y^s_{12}(x,x') = \sum_n j\,(Y_n' - Y_n'') \sin\theta \cos\theta \left(\frac{1}{n\pi}\right) \phi_{hn}(x)\, \phi_{hn}(x') \tag{3.35b}$$

$$Y^s_{21}(x,x') = Y^s_{12} \tag{3.35c}$$

$$Y^s_{22}(x,x') = \sum_n (Y_n' \sin^2\theta + Y_n'' \cos^2\theta) \left(\frac{1}{n\pi}\right)^2 \phi_{hn}(x)\, \phi_{hn}(x') \tag{3.35d}$$

In the air region, the admittances are

$$Y^a_{11}(x,x') = \int_0^\infty dk_x (Y'(k_x) \cos^2\theta + Y''(k_x) \sin^2\theta)\ \phi_h(x,k_x)\, \phi_h(x',k_x) \tag{3.36a}$$

$$Y^a_{12}(x,x') = Y^a_{21}(x,x')$$

$$= \int_0^\infty dk_x\, j\,(Y'(k_x) - Y''(k_x)) \sin\theta \cos\theta \left(\frac{1}{k_x}\right) \phi_h(x,k_x) \phi_h(x',k_x) \tag{3.36b}$$

$$Y^a_{22}(x,x') = \int_0^\infty dk_x (Y'(k_x) \sin^2\theta + Y''(k_x) \cos^2\theta) \left(\frac{1}{k_x}\right)^2 \phi_h(x,k_x)\, \phi_h(x',k_x) \tag{3.36c}$$

where Y_n' and Y_n'' are the input admittances of the slot seen by the nth order *TM* and *TE* modes, respectively, i.e.,

$$Y_n' = -j\, \frac{\omega\mu_0}{q_n}\, cot\,(q_n h) \qquad Y_n'' = -j\, \frac{q_n}{\omega\mu_0}\, cot\,(q_n h)$$

In the air region, $Y'(k_x)$ and $Y''(k_x)$ are the admittances of the *TM* and *TE* plane waves:

$$Y'(k_x) = \frac{\omega\mu_0}{k_y(k_x)} \qquad Y''(k_x) = \frac{k_y(k_x)}{\omega\mu_0}$$

This formulation gives rise to the transverse equivalent circuit representation shown in Fig.3.2. The slot field is composed of an infinite number of *TE* and *TM*-components. The scalar equations so obtained describe propagation in the y-direction. The resonant

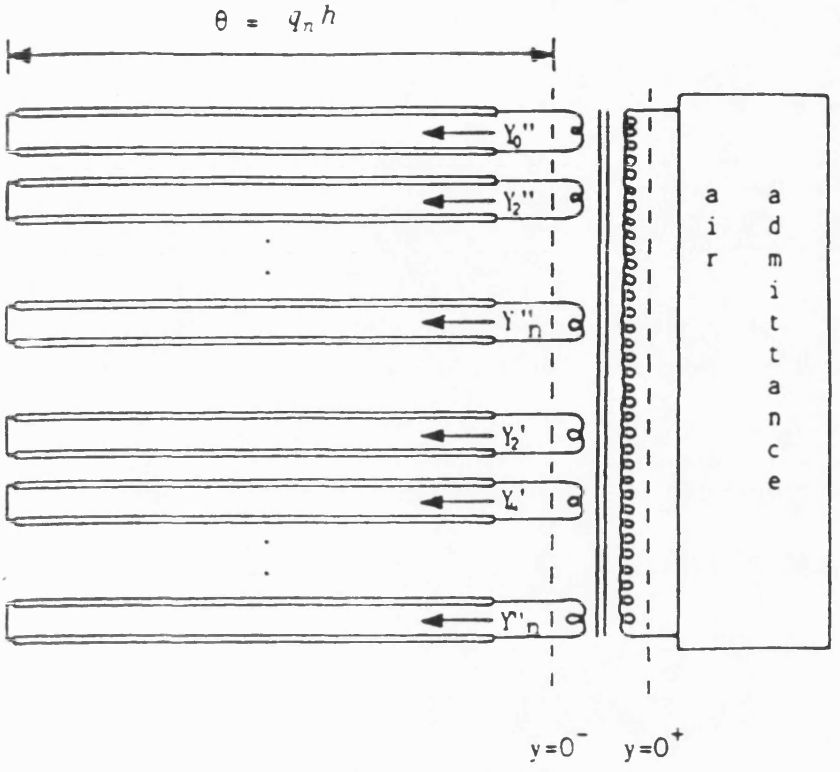

Figure3.2 The transverse equivalent circuit representation for *1DG* .

frequencies of this equivalent network are those frequencies for which the total admittance, taken at any point in the circuit, vanishes. Thus, for a given value of k_0, the propagation constant β is found as that value that causes the total transverse admittance to vanish [4]-[7].

This approach is found to give fast convergence for the value of β. For most practical applications, a 2 by 2 or, at most, a 4 by 4 matrix is all that is required to be solved.

Bearing in mind that the admittance operators have been defined as functions of β for each region for power flow into each region from the interface, continuity of the magnetic fields at the interface ($y = 0$) will give an integral equation in the unknowns $E_x(x, 0)$, $E_z'(x, 0)$, namely

$$\left[\hat{Y}\right] \cdot \begin{bmatrix} E_x(x, 0) \\ dE_z(x, 0)/dx \end{bmatrix} = 0 \tag{3.37}$$

where

$$\hat{Y} = \hat{Y}^s + \hat{Y}^a. \tag{3.38}$$

This is the dispersion equation for β.

3.3 Solution of the Integral Equation-Application of the Ritz-Galerkin Method

The Galerkin method is one of the fundamental mathematical methods for transforming a variational equation into a matrix equation. It will be used to solve the integral equation (3.37). The equation is discretized by means of the set used to expand the unknown $E_x(x, 0)$ and $E_z'(x, 0)$. The choice of a finite expanding set is crucial in achieving rapid convergence in the dispersion equation. If the choice satisfies the edge condition, the "scalar products" in (3.37) will converge rapidly and only a few terms will

be needed. Thus we seek an orthogonal set of functions that can be weighted by a term that takes into account the effect of the 90^0 metal edge.

The behavior of the field vectors at the edge of a conducting wedge of internal angle ϕ, as illustrated in Fig.3.3, has been investigated by Collin [8]. It was concluded that in the vicinity of $r=0$, where r is the radial distance from the edge, when r intends to zero, x- and y-directed components intend to infinity. The order of the singularity, α, depends on the wedge angle ϕ. When $\phi = 0$ the minimum allowed value of α is $-1/2$. When $\phi = \pi/2$, α is $-1/3$. The z-directed components intend to zero. The order is $r^{1/2}$ and $r^{2/3}$ for $\phi = 0$ and $\pi/2$ respectively. Thus a weight function which expresses the behavior of E_x and has a continuous derivative is given by

$$W(x) = (1 + 2x)^{-1/3} (1 - 2x)^{-1/3} = (1 - (2x)^2)^{-1/3} \tag{3.39}$$

From the general orthonormality condition of Gegenbauer polynomials

$$\frac{1}{N_n N_m} \int_{-1}^{1} (1 - u^2)^{\nu - \frac{1}{2}} C_m^{\nu}(u) C_n^{\nu}(u) \, du = \delta_{mn}$$

for a weight function like (3.39), an obvious choice for the basis term is the Gegenbauer polynomial $C_m^{1/6}(x)$ [9].

Thus we expand the unknown fields in terms of a weighted set of the Gegenbauer polynomials:

$$f_m(x) = C_m^{1/6}(2x) \tag{3.40}$$

where $m = 0,2,4,...$ for the even modes and $m = 1,3,5,...$ for the odd modes. Plots of the first three expansion terms for the even and odd cases across the slot are given in Fig.3.4.

So that $E_x(x, 0)$ and $E_z'(x, 0)$ are expanded as

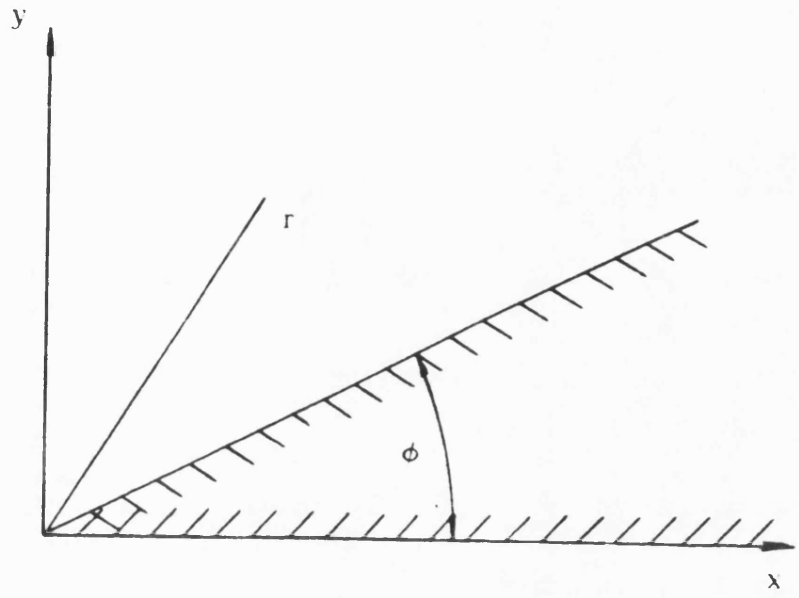

Figure3.3 Conducting wedge.

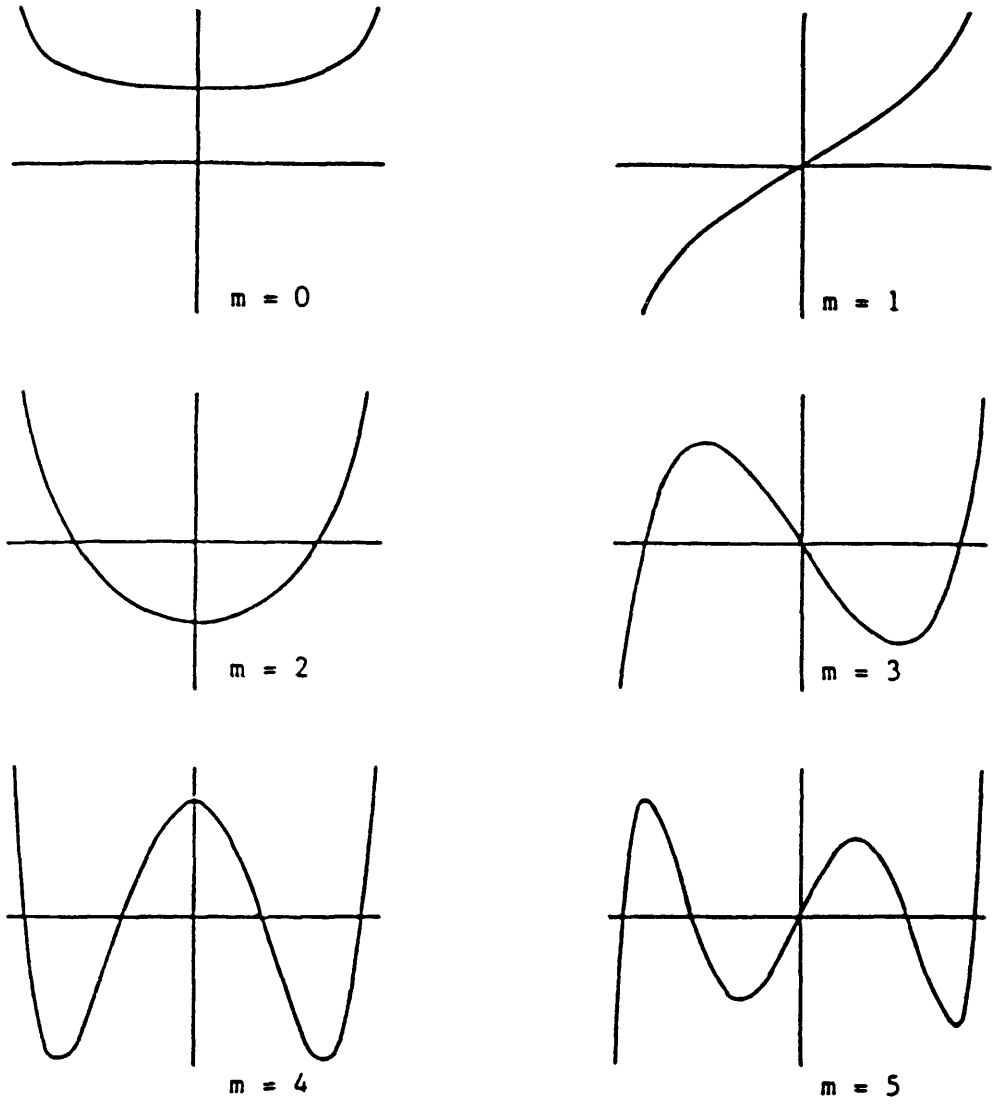

Figure3.4 Amplitude plots of the first three basis terms.

$$E_x(x, 0) = W(x) \sum_m X_m f_m(x) \tag{3.41a}$$

$$E_z'(x, 0) = W(x) \sum_m Z_m f_m(x) \tag{3.41b}$$

where the coefficients X_m and Z_m are the as yet undetermined amplitudes.

With such a basis set, the expansion functions $\phi_{hn}(x)$ and $\phi_h(x,k_x)$ are expanded as

$$\phi_{hn}(x) = \sum_m P_{mn} f_m(x) \tag{3.42a}$$

$$\phi_h(x,k_x) = \sum_m P_m(k_x) f_m(x) \tag{3.42b}$$

where the inner products P_{mn} and $P_m(k_x)$, evaluated across the half slot, are defined as

$$P_{mn} = < W(x) f_m(x), \phi_{hn}(x) >$$

$$\equiv \int_0^{1/2} W(x) f_m(x) \phi_{hn}(x) \, dx \tag{3.43a}$$

$$P_m(k_x) = < W(x) f_m(x), \phi_h(x,k_x) >$$

$$\equiv \int_0^{\infty} W(x) f_m(x) \phi_h(x,k_x) \, dx \tag{3.43b}$$

The evaluation of P_{mn} and $P_m(k_x)$ is given in [2 Appendix I]. Here the advantage of changing $E_x(x, 0)$ to $E_z'(x, 0)$ can be seen again. Because all the admittance operators are expressed with $\phi_{hn}(x)$ and $\phi_h(x,k_x)$, only one set of inner products is needed.

Upon substituting the series expansions for the fields in (3.37) and carrying out the integration, we obtain the matrix equation

$$\left[\dot{\mathbf{Y}}\right]\left[\begin{matrix}\mathbf{X}\\ \mathbf{Z}\end{matrix}\right] = 0 \tag{3.44}$$

This equation has a nontrivial solution when

$$\det |\mathbf{Y}| = 0 \tag{3.45}$$

3.4 A Simplification for the Even Modes

(3.44) is a general equation. It is sufficient to solve for β, although the field amplitudes X_m and Z_m cannot be found directly. For the even modes a further simplification was carried out [3]. In order to recover a scalar transverse equivalent circuit and obtain the field amplitudes, it is convenient to consider the fundamental transverse propagating mode in the slot, seen as a parallel-plate waveguide terminated by a short circuit at $y=-h$. This is incident upon a discontinuity (the transition between the two regions) and thus excites the radiation modes in the air region and the higher order nonpropagating transverse modes in the slot. In this manner, the fundamental slot mode can be isolated in (3.37) and all the other contributions lumped together to give

$$\left[\hat{Y}\right]\cdot\begin{bmatrix}E_x(x,0)\\ E_z'(x,0)\end{bmatrix}=\begin{bmatrix}-H_{z0}\,\phi_{h0}(x)\\ 0\end{bmatrix} \tag{3.46}$$

where $\hat{Y}=\hat{Y}'^{s}+\hat{Y}^{a}$, and $\hat{Y}'^{s}$ is the slot admittance operator with fundamental term removed. Also, the quantity $\hat{Y}$ denotes from now on in this section the total admittance with the fundamental term removed.

Upon discretization (3.46) becomes

$$\left[\mathbf{Y}\right]\cdot\begin{bmatrix}\mathbf{X}\\ \mathbf{Z}\end{bmatrix}=(-H_{z0})\cdot\begin{bmatrix}\mathbf{P}_0\\ \mathbf{0}\end{bmatrix} \tag{3.47}$$

Rearranging,

$$\begin{bmatrix}\mathbf{X}\\ \mathbf{Z}\end{bmatrix}=(-H_{z0})\mathbf{Y}^{-1}\cdot\begin{bmatrix}\mathbf{P}_0\\ \mathbf{0}\end{bmatrix} \tag{3.48}$$

Multiply both sides by $\left[\mathbf{P}_0^T,\,\mathbf{0}^T\right]$:

$$\left[\mathbf{P}_0^T,\,\mathbf{0}^T\right]\begin{bmatrix}\mathbf{X}\\ \mathbf{Z}\end{bmatrix}=\left[\mathbf{P}_0^T,\,\mathbf{0}^T\right]\mathbf{Y}^{-1}\begin{bmatrix}\mathbf{P}_0\\ \mathbf{0}\end{bmatrix}(-H_{z0}) \tag{3.49}$$

However, from (3.14a) and (3.41a),

$$\mathbf{P}_0^T \cdot \mathbf{X} = E_{x0} \tag{3.50}$$

and so

$$\frac{-H_{z0}}{E_{x0}} = \left[\left[\mathbf{P}_0^T, \mathbf{0}^T \right] \cdot Y^{-1} \cdot \begin{bmatrix} \mathbf{P}_0 \\ \mathbf{0} \end{bmatrix} \right]^{-1} \tag{3.51}$$

The normalized admittance of the fundamental slot mode looking from $y = 0$ toward the short circuit is

$$\frac{H_{z0}}{E_{x0}} = -j \cot q_0 h \tag{3.52}$$

Equation (3.51) represents the admittance of all the higher order slot modes and air waves as seen from the interface. At resonance the total admittance seen from both sides of the interface must total zero. Therefore the equation for resonance is

$$-j \cot q_0 h + \left[\left[\mathbf{P}_0^T, \mathbf{0}^T \right] \cdot \begin{bmatrix} \mathbf{Y}_{11} & \mathbf{Y}_{12} \\ \mathbf{Y}_{21} & \mathbf{Y}_{22} \end{bmatrix}^{-1} \cdot \begin{bmatrix} \mathbf{P}_0 \\ \mathbf{0} \end{bmatrix} \right]^{-1} = 0 \tag{3.53}$$

When N basis terms are used, $\hat{Y}_{11}$ becomes an N by N matrix, $\hat{Y}_{12}$ becomes N by $N-1$, $\hat{Y}_{21}$ becomes $N-1$ by N, and $\hat{Y}_{22}$ becomes $N-1$ by $N-1$. The overall admittance matrix becomes a square matrix of order $(2N-1)$.

The elements of the admittance matrices of the slot region occurring in (3.53) can be found from (3.35a)-(3.35c) to be

$$(Y_{11}^s)_{km} = -j \sqrt{\varepsilon_r k_0^2 - \beta^2} \sum_n \frac{\coth |q_n| h}{|q_n|} P_{kn} P_{mn} \tag{3.54}$$

and so on, where

$k = 0,2,4,\ldots \quad m = 0,2,4,\ldots \quad$ for Y_{11}

$k = 0,2,4,\ldots \quad m = 2,4,6,\ldots \quad$ for Y_{12}

$k = 2,4,6,\ldots \quad m = 0,2,4,\ldots \quad$ for Y_{21}

$k = 2,4,6,\ldots \quad m = 2,4,6,\ldots \quad$ for Y_{22}.

Corresponding expressions are derived from (3.36a)-(3.36c) for the admittance matrices of the air region. The apparent pole singularity at $k_x = 0$ in (3.36b) and (3.36c) is in fact compensated by a zero of $P_m(k_x)$ there.

3.5 Computed and Measured Results

The hybrid modes of *IDG* are designated HE_{nm} or EH_{nm} according to the relative dominance of the *TE* or *TM*-to-y components, respectively. The subscripts n,m refer to the number of half-wave variations across the slot and down the slot. For ease of manufacture and availability of equipment, the experimental prototypes were made from slots with two different cross-sections, i.e. $1.016\times1.524\ cm$ for HE_{01} mode supporting *IDG*, and $2.286\times1.016\ cm$ for EH_{11} mode, for transition into X-band rectangular waveguide.

Having solved for β, the basis amplitudes **X** and **Z** can be found from (3.48) for the even modes. Thus, the mode amplitudes of the field components given in (3.14) can be found as

$$E_{xn} = \mathbf{P}_n^T \cdot \mathbf{X} \tag{3.55a}$$

$$E_{yn} = -\left(\frac{1}{q_n}\right) cot\ q_n h \left((n\pi)\mathbf{P}_n^T \cdot \mathbf{X} + j\,\beta\,(\frac{1}{n\pi})\,\mathbf{P}_n^T \cdot \mathbf{Z}\right) \tag{3.55b}$$

$$E_{zn} = (\frac{1}{n\pi})\,\mathbf{P}_n^T \cdot \mathbf{Z} \tag{3.55c}$$

$$H_{xn} = (n\pi)\,\frac{cot\ q_n h}{\omega\,\mu_0\,q_n}\left(\beta\,\mathbf{P}_n^T \cdot \mathbf{X} + j(\frac{\varepsilon_r k_0^2 - (n\pi)^2}{(n\pi)^2})\mathbf{P}_n^T \cdot \mathbf{Z}\right) \tag{3.55d}$$

$$H_{yn} = \frac{1}{j\omega\mu_0}(j\,\beta\mathbf{P}_n^T \cdot \mathbf{X} + \mathbf{P}_n^T \cdot \mathbf{Z}) \tag{3.55e}$$

$$H_{zn} = \frac{1}{\omega\mu_0}\,\frac{cot q_n h}{q_n}(-j\,q_0^2\,\mathbf{P}_n^T \cdot \mathbf{X} + \beta\mathbf{P}_n^T \cdot \mathbf{Z}) \tag{3.55f}$$

Similar results can be found for the components in the air region. For most purposes, it

is sufficient to consider the fundamental approximation only so that X_0 is the only finite amplitude term. The expressions (3.55) are then considerably reduced.

The dispersion characteristics of several *IDG* geometries were measured. The comparison between the measured and computed results are shown in Fig.3.5 and Fig.3.6 for the HE_{01} and EH_{11} mode supporting *IDG* guides, respectively. In Fig.3.7 the dispersion curves for the even modes above the cutoff of the X-band *IDG* are plotted, using two-term expansions.

The field magnitude plots of the fundamental HE_{01} mode taken across a transverse section are given in Fig.3.8. The field plots show that the fundamental mode is essentially *TE* with respect to y with the components E_x, H_y H_z. In the slot these terms dominate, the *TM* components are only excited in order to satisfy the boundary conditions imposed by the 90^0 edge. Also evident from the plots is the singularity due to the edge. The z-directed components, as expected, are not affected by the edge and show no singular behavior.

The measured loss of the HE_{01} mode supporting guide is 0.353 dB/m at 10 GHz and the Q-factor is 2929.4 [2]

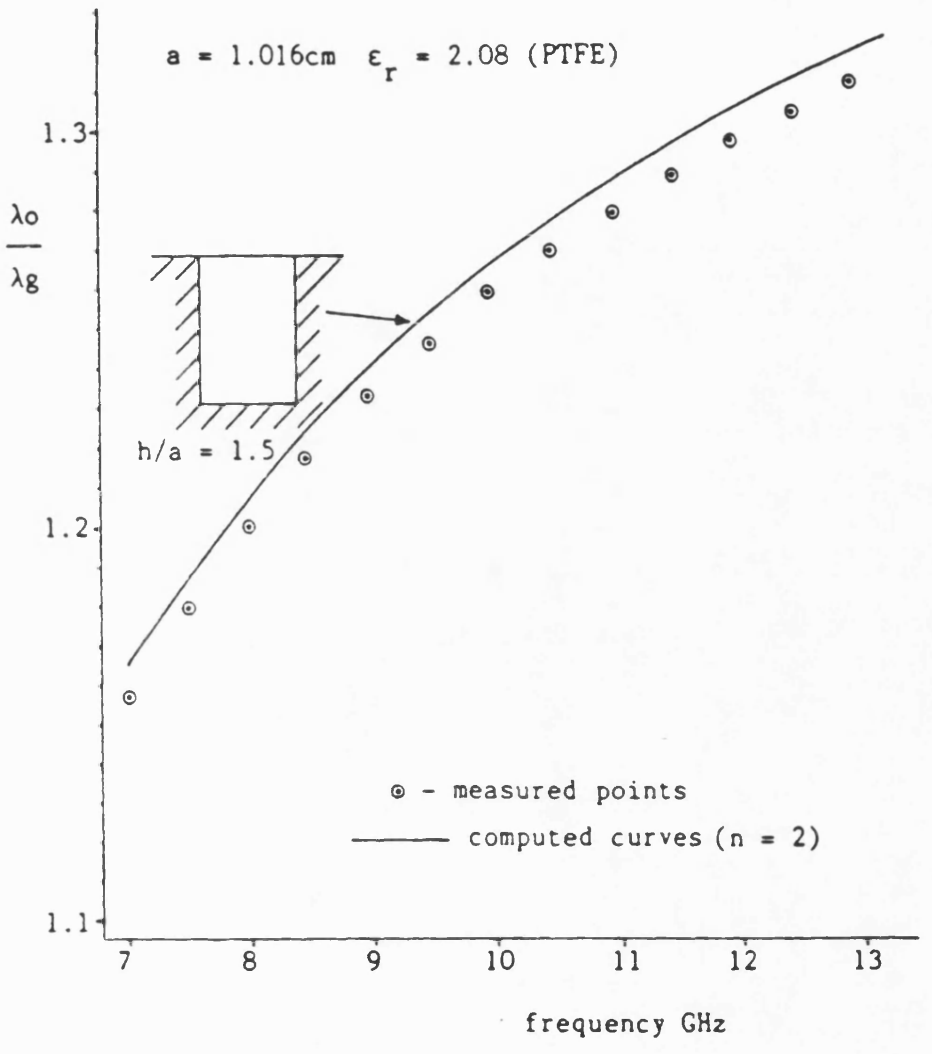

Figure3.5 A comparison of computed and measured dispersion curves for a deeper *IDG* sample at X-band.

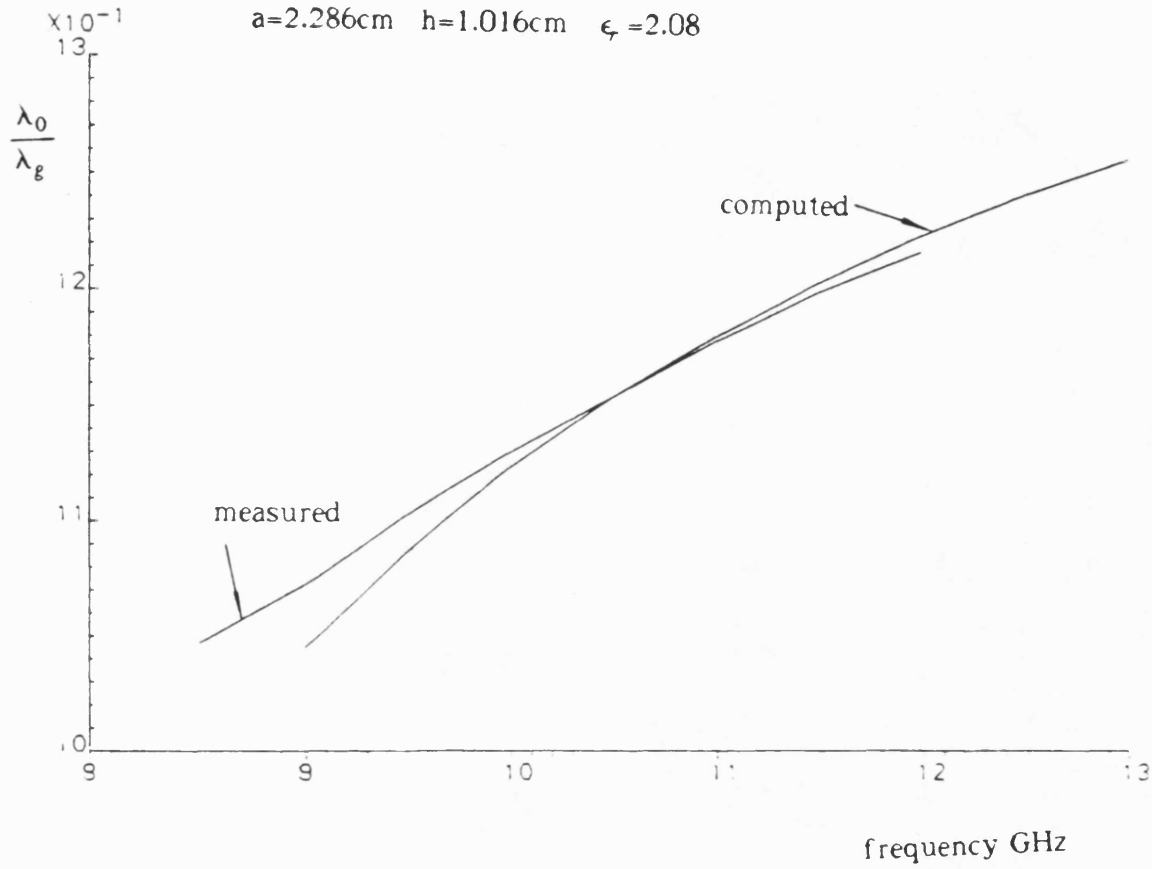

Figure3.6 A comparison of computed and measured dispersion curves for a shallower *IDG* sample at X-band.

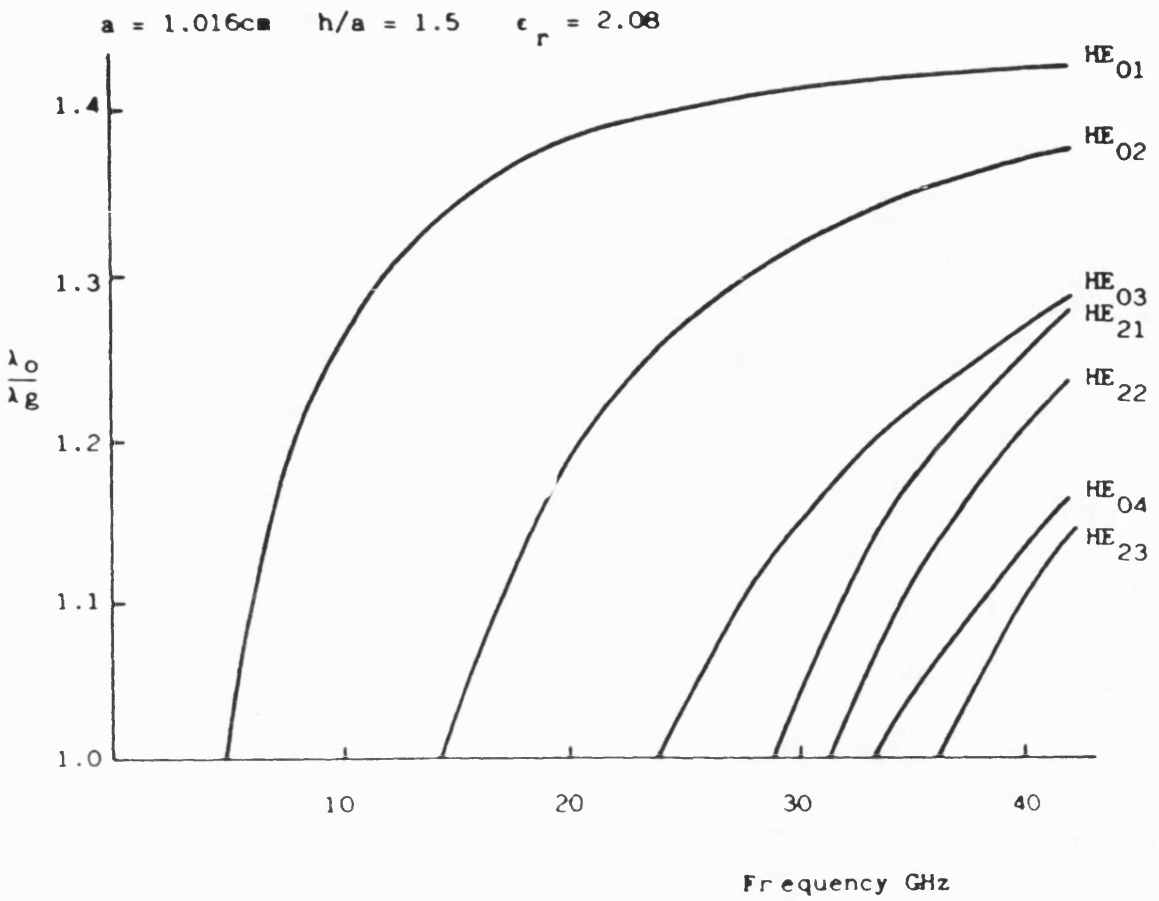

Figure3.7 Computed dispersion curves for the even modes of an x-band sample of *IDG* up to 40 *GHz* .

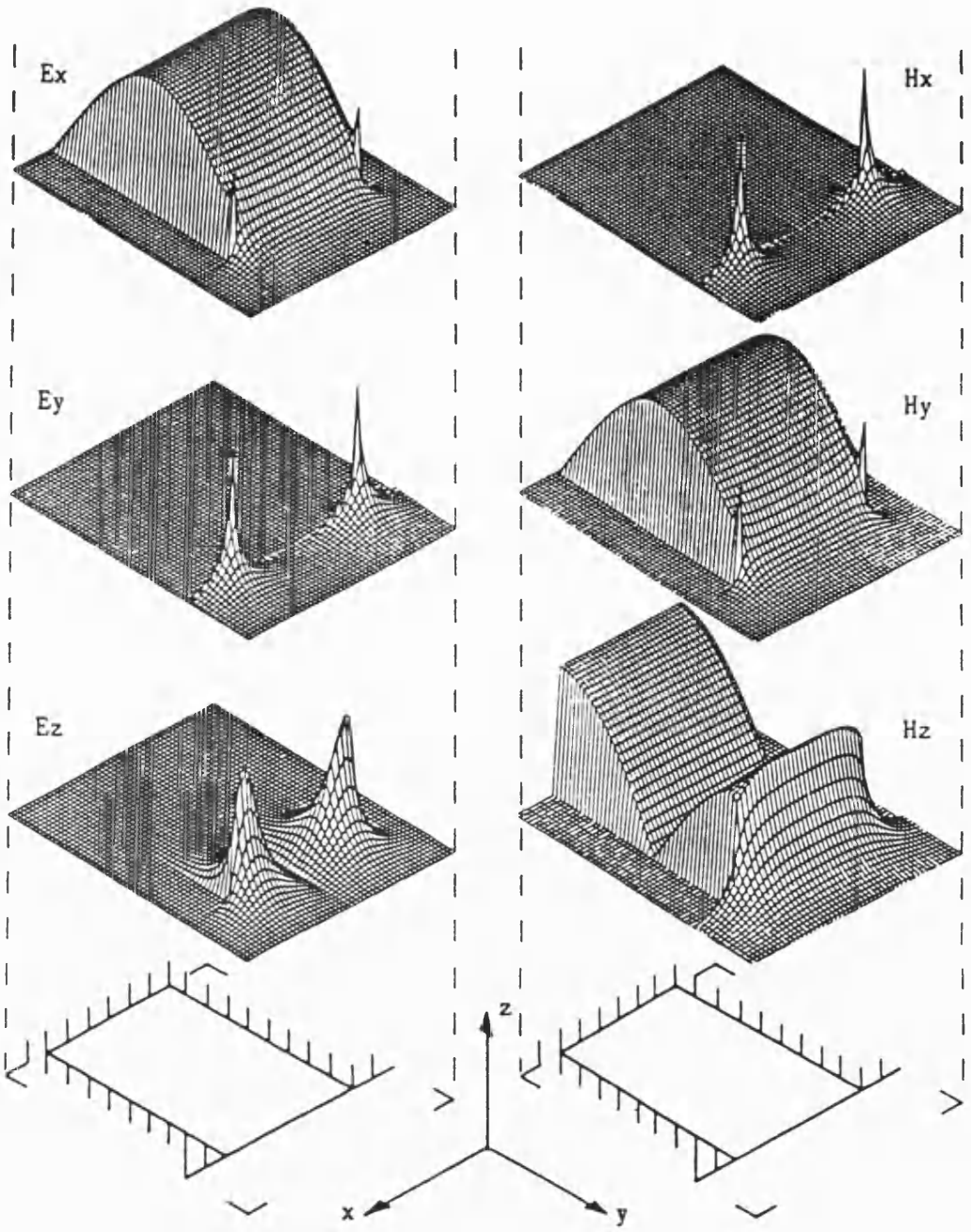

Figure3.8 The field components of the fundamental HE_{01} mode plotted as the magnitude values over the transverse guide section.

REFERENCES

[1] T. Itoh and B. Adelseck, " Trapped image guide for millimeter wave circuits ", *IEEE Trans. Microwave Theory and Tech., vol. MTT*-28, pp. 1433-1436, Dec. 1980.

[2] T. Rozzi and S. Hedges, " Rigorous analysis and network modeling of inset dielectric guide ", *IEEE Trans. Microwave Theory and Tech., vol. MTT*-35, pp. 823-834, Sep. 1987.

[3] T. Itoh, "Spectral domain immittance approach for dispersion characteristics of generalized printed transmission lines ", *IEEE Trans. Microwave Theory and Tech., vol. MTT*-28, pp.733-736, July, 1980.

[4] S. T. Peng and A. A. Oliner, "Guidance and leakage properties of a class of open dielectric waveguides ", Part 1, *IEEE Trans. Microwave Theory and Tech., vol. MTT*-29, pp. 843-855, Sept. 1981

[5] J. Kot and T. Rozzi, "Rigorous modeling of single and coupled rectangular dielectric waveguides by transverse resonance diffraction", in *Proc. 14th European Microwave Conf.* (Liege), Sept. 1981.

[6] N. Dagli and C. G. Fonstad, "Analysis of rib dielectric waveguides ", *IEEE J. Quantum Electron.*, vol. QE-21, pp. 315-321, Apr. 1985.

[7] M. Koshiba and M. Suzuki, "Vectorial wave analysis of dielectric waveguides for optical-integrated circuits using equivalent network approach", *IEEE J. Lightwave Technol.*, vol. LT-4, pp. 656-664, June 1986.

[8] R. E. Collin, *Field Theory of Guided Waves.* New York: McGraw-Hill, 1960, p.18.

[9] I. S. Gradshteyn and I. M. Ryshik, *Table of Integrals, Series* and *Products*. New York: Academic Press, 1980, p. 827.

CHAPTER 4

MODE COMPLETENESS, NORMALIZATION AND GREEN'S FUNCTION OF LSE MODES IN IDG

4.1 Introduction

The guided modes we found in the last chapter are sufficient to describe any guided field distribution in the *IDG*, provided the guide is uniform. They are not sufficient, however, to describe radiation phenomena. The complete set of modes of an open waveguide includes a finite number of guided modes and a continuum of radiation modes. Excitation of the latter takes place due to discontinuities, particularly, when these are located close to the air-dielectric interface. Therefore, with a view to analyzing practical components in *IDG*, it is necessary to obtain a complete spectral characterization, inclusive of the continuum. Once the complete spectrum is found, it is possible to construct the appropriate Green's function of the guide for use in the treatment of discontinuity problems. A mathematical difficulty arises at this point in as much as the spectral components need to be orthonormalized over the guide cross-section.

This trivial task in classical waveguide becomes non-trivial and tedious already for

guides of inhomogeneous, separable cross section, particularly if a continuum is involved.

In the *IDG*, the problem is essentially complicated by the inseparable nature of the two-dimensional cross-section, containing diffraction edges (the metal corners) at the interface between two distinct regions (the slot and the air region). For the one-dimensional separable case (e.g. the multilayer slab), an elegant method, based on the transverse equivalent circuit interpretation and the formal properties of the transverse Green's function, can be found in a textbook like [1].

A solution for the two-dimensional, nonseparable, open case such as the *IDG* was not reported before the work that led to this thesis.

The analysis in this chapter will be developed for the even $LSE(TE^y)$ polarization, having $E_y = 0$ and E_x as the main electric field component. We will deal first with the question of the normalization of the discrete spectrum in the same representation of the singular field over the slot aperture and then derive the orthonormalized continuum. The scalar Green function is subsequently obtained and applied to the scattering of a thin transverse dipole at the air-dielectric interface.

4.2 The Normalized Spectrum of the Slab Waveguide

If the effect of the metal corners of the slot could be ignored, i.e. the side walls were infinitely far removed from each other, the *IDG* would reduce to a dielectric slab over a ground plane. This structure is particularly simple, and allow us to study the spectrum and radiation properties of dielectric waveguide. It is therefore instructive to retrace the procedure involved in determining the normalized complete spectrum of the grounded slab, illustrated in Fig.4.1. A good discussion can be found in [1], [2] and [3].

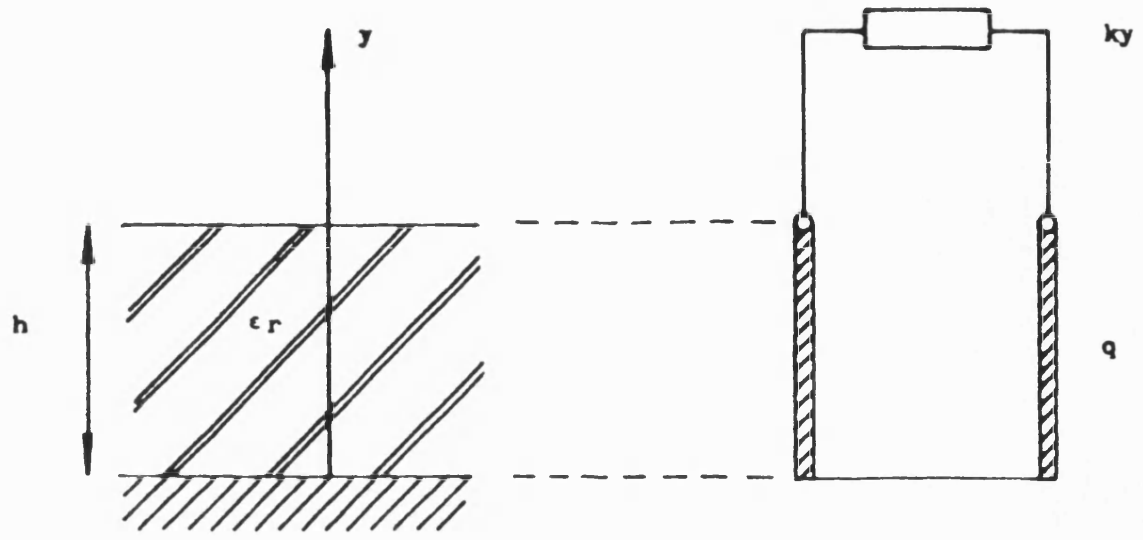

Figure 4.1 The metal-backed dielectric slab waveguide and its transverse equivalent circuit.

4.2.1 Relationship Between Characteristic Green's Function and Eigenvalue Problem

The general Sturm-Liouville differential operator L may be written as:

$$L f(y) = [\frac{d}{dy}(p(y)\frac{d}{dy}) - q(y) + \lambda w(y)]\, f(y)$$

For the Sturm-Liouville problem the characteristic Green function $g(y,y';\lambda)$ is defined by

$$L\ g(y,y';\lambda) = -\delta(y-y') \qquad y_1 < y,y' < y_2 \tag{4.1}$$

subject to the boundary conditions

$$(p\frac{d}{dy} + \alpha_{1,2})\ g(y,y';\lambda) = 0 \qquad y = y_{1,2} \tag{4.2}$$

The parameter λ is arbitrary but so restricted as to assure a unique solution of (4.1)

Fig.4.2 shows a network schematization of the characteristic Green function problem. The voltage and current on this transmission line satisfy the non-uniform transmission-line equations with the addition of a current source term $i(y') = -\delta(y-y')$

$$-d\frac{V(y,y')}{dy} = j\,k_y(y)\,Z(y)\,I(y,y') \tag{4.3a}$$

$$-d\frac{I(y,y')}{dy} = j\,k_y(y)\,Y(y)\,V(y,y') - \delta(y-y') \tag{4.3b}$$

where $Z(y) = 1/Y(y) = \frac{\omega\mu}{k_y(y)}$ for the case of a TE mode was considered. $k_y(y)$ is the propagation constant. The corresponding second-order differential equation for $V(y,y')$ has the form

$$\left(\frac{d}{dy}\frac{1}{\mu'(y)}\frac{d}{dy} + \varepsilon'(y)k_0^2 - \frac{\beta^2}{\mu'(y)}\right)V(y-y') = -j\,\omega\,\mu\,\delta(y-y') \tag{4.4}$$

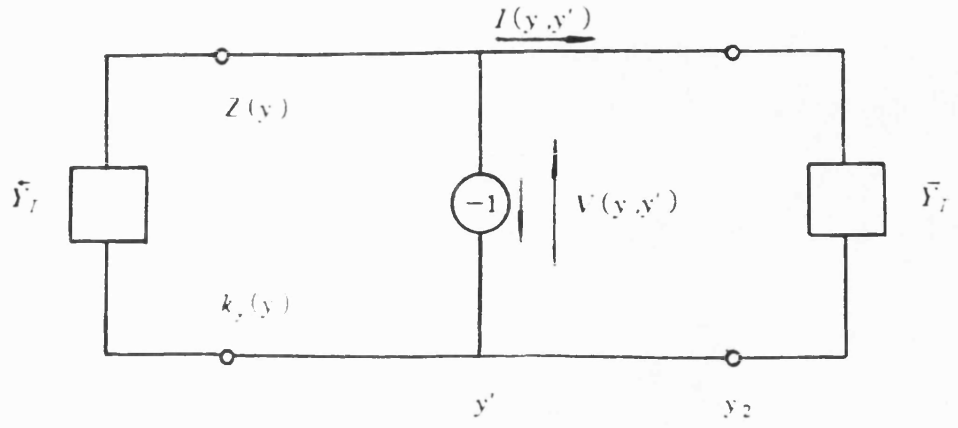

Figure 4.2 Non-uniform transmission line excited with a unit current generator.

where $\mu'(y) = \frac{\mu(y)}{\mu_0}$, $\varepsilon'(y) = \frac{\varepsilon(y)}{\varepsilon_0}$ are assumed. Comparing (4.1) and (4.4) and setting $\varepsilon'(y) = \varepsilon_r$, $\mu'(y) = 1$ we get the identifications

$$p(y) = w(y) = 1 \qquad q(y) = -\varepsilon_r k_0^2 \qquad \beta^2 = -\lambda$$

$$V(y,y') = j\,\omega\,\mu_0\; g(y,y';\lambda) \tag{4.5}$$

and the boundary conditions in (4.2) are rephrased by (4.3a) and (4.5) in terms of

$$\frac{I}{V} = \frac{j\,p\,dg/dy}{\omega\,\mu_0\,g} \tag{4.6}$$

Consequently, the termination admittances $\overleftarrow{Y}_t$ and $\overrightarrow{Y}_t$ are

$$\overleftarrow{Y}_t = -\frac{I}{V} = \frac{j\,\alpha_1}{\omega\,\mu} \tag{4.7a}$$

$$\overrightarrow{Y}_t = \frac{I}{V} = -\frac{j\,\alpha_2}{\omega\,\mu} \tag{4.7b}$$

Since the configuration in Fig.(4.2) can be viewed as a cavity, it is physically manifest that the voltage response g will be finite and well defined unless the choice of parameter λ is such that resonance can exist. In another word, for a fixed $\alpha_{1,2}$ and $y_{1,2}$ at $\lambda = \lambda_m$, the corresponding voltage or current will be infinite, i.e. resonances will exist. Since the resonant condition $\lambda = \lambda_m$ implies the persistence of a response even when the source is removed, the functional form of the resonant solution satisfies the homogeneous equation. Thus, information about the desired eigenvalues of the homogeneous equation is contained in the singularities of the characteristic Green's function g, and the problem of determining all possible resonances is directly related to the complete investigation of the singularities of $g(y,y';\lambda)$ in the complex λ-plane.

The characteristic Green's function can be expanded as

$$g(y,y';\lambda) = \sum_m a_m(y',\lambda)\,\psi_m(y) \tag{4.8}$$

where ψ_m is the eigenfunction of the homogeneous equation, i.e.

$$\frac{d}{dy} p \frac{d\psi_m(y)}{dy} - q\ \psi_m(y) = -\lambda\, w\ \psi_m(y) \tag{4.9}$$

Substituting (4.8), (4.9) into (4.1), we obtain

$$\sum_m a_m\ (\lambda - \lambda_m)\, w\ \psi_m(y) = -\delta\ (y - y') \tag{4.10}$$

Multiplying both sides of (4.10) by $\psi_n(y)$ and integrating over y yields

$$\sum_m \int_a^b a_m\ (\lambda - \lambda_m)\, w\ \psi_m(y)\ \psi_n(y)\ dy = -\int_a^b \psi_n(y)\ \delta\ (y - y')\ dy$$

Orthogonality gives

$$a_n\ (\lambda - \lambda_n) = -\psi_n(y')$$

therefore

$$g\ (y,y';\lambda)\ = -\sum_{m=1}^{\infty} \frac{\psi_m(y)\ \psi_m(y')}{\lambda - \lambda_m} \tag{4.11}$$

This representation of $g\ (y,y';\lambda)$ highlights the existence of singularities in the complex λ-plane at the eigenvalues λ_m. If (4.11) is integrated in the complex λ plane about a contour c inclosing all the singularities of g, then an application of Cauchy's theorem yields the following formal relationship

$$-\frac{1}{2\pi j} \oint_c g\ (y,y';\lambda)\ d\lambda = -\sum_m \psi_m(y)\ \psi_m(y') \left(-\frac{1}{2\pi j}\right) \oint_c \frac{d\lambda}{\lambda - \lambda_m}$$

$$= \sum_m \psi_m(y)\ \psi_m(y') = \frac{\delta\ (y - y')}{w\ (y)} \tag{4.12}$$

In the above discussion it has been assumed that the dimensions y_1 and y_2 are finite so that cavity resonances, which occur for discrete values of λ_m, characterize simple pole singularities of g. If one of the dimensions becomes infinite, the discrete resonances coalesce into a continuous spectrum; in this instance, $g\ (y,y';\lambda)$ possesses a branch-point singularity giving rise to the necessity of introducing a branch-cut in the complex λ-plane to ensure uniqueness of g.

4.2.2 Construction of Green's Function

(4.9) is an expression of Green's function as a series of eigenfunctions. We will now develop a non-series expression for Green's function. From (4.1) it can be seen that at $y = y'$, $\frac{d}{dy} p \frac{dg}{dy} = \infty$ when and only when g is continuous and $p \frac{dg}{dy}$ is a unit step, as shown in Fig.4.3. When $y \neq y'$ g can be written in terms of two solutions of the homogeneous equation, $\overleftarrow{V}(y)$ and $\overrightarrow{V}(y)$, satisfying the required boundary condition at y_1 and y_2, respectively.

$$L \overleftarrow{V}(y) = 0 \qquad y < y' \qquad (p \frac{d}{dy} + \alpha_1) \overleftarrow{V}(y) \Big|_{y=y_1} = 0 \tag{4.13a}$$

$$L \overrightarrow{V}(y) = 0 \qquad y > y' \qquad (p \frac{d}{dy} + \alpha_2) \overrightarrow{V}(y) \Big|_{y=y_2} = 0 \tag{4.13b}$$

The appropriate form of the solution is,

$$g(y,y';\lambda) = \begin{cases} A \overleftarrow{V}(y) \overrightarrow{V}(y') & : \quad y < y' \\ A \overleftarrow{V}(y') \overrightarrow{V}(y) & : \quad y > y' \end{cases}$$

The constant A must be determined so as to satisfy the condition $p \frac{dg}{dy} = -1$, i.e.

$$A\, p\, (\overleftarrow{V}(y') \overrightarrow{V}'(y) - \overrightarrow{V}(y') \overleftarrow{V}'(y)) \Big|_{y=y'} = -1$$

Hence

$$g(y,y';\lambda) = \frac{\overleftarrow{V}(y_<) \overrightarrow{V}(y_>)}{-p\, w(\overleftarrow{V}, \overrightarrow{V})} \tag{4.14}$$

where

$$y_< \equiv \min(y,y')$$

$$y_> \equiv \max(y,y')$$

$$w(\overleftarrow{V}, \overrightarrow{V}) = \overleftarrow{V} \overrightarrow{V}' - \overrightarrow{V} \overleftarrow{V}' \tag{4.15}$$

$w(\overleftarrow{V}, \overrightarrow{V})$ is called Wronskian determinant of $\overleftarrow{V}, \overrightarrow{V}$. It contains λ as a parameter and has

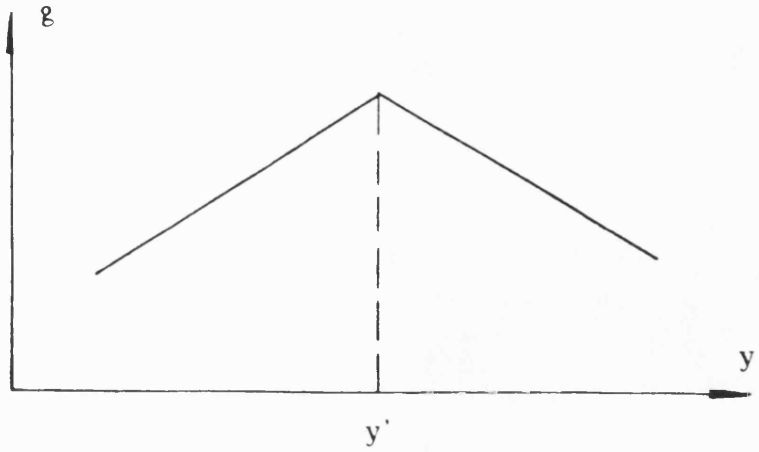

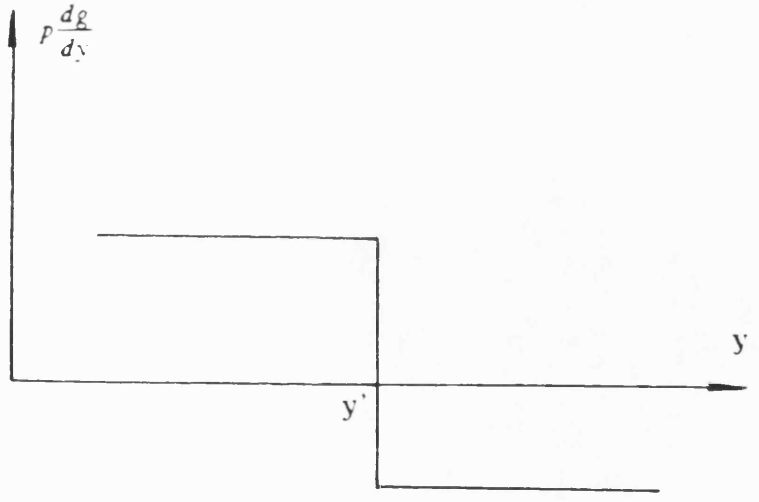

Figure 4.3 The behaviour of g in the vicinity of y=y'.

its poles at $\lambda = \lambda_m$. Since $\overleftarrow{V}$,$\vec{V}$ are linearly independent, the value of w is non-zero.

Multiplying (4.11a) by $\vec{V}$, (4.11b) by $\overleftarrow{V}$ and subtracting the resulting equations gives

$$\overleftarrow{V}\frac{d}{dy}p\frac{d}{dy}\vec{V} - \vec{V}\frac{d}{dy}p\frac{d}{dy}\overleftarrow{V} = \frac{d}{dy}(p\,w) = 0$$

i.e. the value of the denominator of (4.14) is constant for all value of y and can be evaluated at any convenient point y_0 in the interval $y_1 < y < y_2$. Normalizing $V(y)$ such that $V(y_0) = 1$, i.e.,

$$\overleftarrow{V}(y,y_0) = \frac{\overleftarrow{V}(y)}{V(y_0)}$$

$$\vec{V}(y,y_0) = \frac{\vec{V}(y)}{V(y_0)}$$

and recalling (4.7), the Green function in (4.14) can be rewritten as

$$g(y,y';\lambda) = \frac{\overleftarrow{V}(y_<,y_0)\,\vec{V}(y_>,y_0)}{j\omega\mu\overleftrightarrow{Y}(y_0)} \tag{4.16a}$$

where $\overleftrightarrow{Y}(y_0)$ denotes the sum of the admittances looking to the left and right of y_0.

$$\overleftrightarrow{Y}(y_0) = \overleftarrow{Y}(y_0) + \vec{Y}(y_0) = \frac{\overleftarrow{I}(y_0)}{\overleftarrow{V}(y_0)} + \frac{\vec{I}(y_0)}{\vec{V}(y_0)} \tag{4.16b}$$

The poles of $g(y,y';\lambda)$ in the complex λ plane occurring at $\lambda = \lambda_m$, which implies that the existence of a solution ψ_m of the homogeneous equation coincides with the vanishing of the total admittance of the equivalent network model.

In (4.16) simple poles in the complex λ-plane are situated at the zeros of $\overleftrightarrow{Y}(y_0)$, λ_m. The behavior of the denominator in the vicinity of a typical zero at λ_m is given by the Taylor series expansion

$$\overleftrightarrow{Y}(y_0,\lambda) = \overleftrightarrow{Y}(y_0,\lambda_m) + (\lambda - \lambda_m)\frac{\partial}{\partial\lambda_m}\overleftrightarrow{Y}(y_0,\lambda_m) + \cdots \tag{4.17}$$

where

$$\frac{\partial}{\partial\lambda_m}\overleftrightarrow{Y}(y_0,\lambda_m)\equiv\frac{\partial}{\partial\lambda}\overleftrightarrow{Y}(y_0,\lambda)\Big|_{\lambda=\lambda_m}$$

From (4.12), (4.5), (4.16a) and (4.17), we obtain the following delta-function representation for the *TE*-mode problem,

$$\begin{aligned}\mu'(y)\,\delta(y-y') &= -\frac{1}{2\pi j}\oint_c g(y,y';\lambda)\,d\lambda=\sum_m \psi_m(y)\,\psi_m(y')\\ &=-\frac{1}{2\pi j}\oint_c \frac{\overleftarrow{V}(y,y';\lambda)\,\vec{V}(y,y';\lambda)}{j\omega\mu_0\overleftrightarrow{Y}(y_0,\lambda)}d\lambda\\ &=\sum_m \frac{\overleftarrow{V}(y,y';\lambda_m)\,\vec{V}(y,y';\lambda_m)}{-j\omega\mu_0\dfrac{\partial}{\partial\lambda_m}\overleftrightarrow{Y}(y_0,\lambda_m)}\frac{1}{2\pi j}\oint_c\frac{d\lambda}{\lambda-\lambda_m}\\ &=\sum_m \frac{\overleftarrow{V}(y,y';\lambda_m)\,\vec{V}(y,y';\lambda_m)}{\omega\mu_0\dfrac{\partial}{\partial\lambda_m}\overleftrightarrow{B}(y_0,\lambda_m)}\qquad \overleftrightarrow{Y}=j\overleftrightarrow{B}\end{aligned}\tag{4.18}$$

Hence, the normalized mode functions $\psi_m(y)$ are given by:

$$\psi_m(y)=\frac{V(y,y_0;\lambda_m)}{\sqrt{\omega\mu_0(\partial/\partial\lambda_m)\overleftrightarrow{B}(y_0,\lambda_m)}}\tag{4.19}$$

4.2.3 Normalized Mode Function for the Slab Guide

The problem of finding a complete orthonormal set of functions has been reduced systematically to determining the solution of the corresponding inhomogeneous differential equation (4.1), completely investigating its singularities, and then inferring the desired representation by carrying out a contour integration in (4.12) about all the singularities of the characteristic Green's function in the complex λ-plane.

The normalized mode functions for the slab guide will now be investigated. If the expansion of the field takes place in terms of the transverse wavenumber in the air

region, k_y, taken as an independent quantity, the wavenumber in the z-direction, β, is determined by:

$$\beta^2 = k_0^2 - k_y^2 \tag{4.20}$$

The completeness of the *TE* spectrum of the slab guide can then be stated as:

$$\sum_s \psi_s(y)\,\psi_s(y') + \int_0^\infty dk_y\,\psi(y;k_y)\,\psi(y';k_y) \equiv \delta(y-y') \tag{4.21}$$

where the summation is over the finite number of surface waves, the integral over the continuum and the orthonormalization is such that

$$\int_0^\infty dy\,\psi_s(y)\,\psi_r(y) = \delta_{sr} \tag{4.22a}$$

$$\int_0^\infty \psi_s(y)\,\psi(y;k_y) = 0 \tag{4.22b}$$

In order to satisfy the boundary condition on $E_x \infty V$, the two independent solutions of the transverse transmission line equation can be written as:

$$\overleftarrow{V}(y) = \frac{\sin q(y+h)}{\sin qh} \tag{4.23}$$

where

$$q^2 = \varepsilon_r k_0^2 - \beta^2 = k_y^2 + (\varepsilon_r - 1)\,k_0^2 \tag{4.24}$$

satisfying the boundary condition for $y \le 0$ and

$$\overrightarrow{V}(y) = e^{-jk_y y} \qquad y \ge 0 \tag{4.25}$$

such that $\overleftarrow{V}(y) = \overrightarrow{V}(y) = 1$ at $y = 0$. We have then:

$$g = \frac{\overleftarrow{V}(y;k_y^2)\,\overrightarrow{V}(y';k_y^2)}{j\omega\mu_0 \overleftrightarrow{Y}(k_y^2)} \tag{4.26}$$

Where $\overleftrightarrow{Y}$ is the total admittance of the transverse equivalent circuit of Fig.(4.1b), given by

$$\omega \mu_0 \overleftrightarrow{Y} = k_y - jq \cot qh \tag{4.27}$$

By setting $\overleftrightarrow{Y} = 0$, we obtain the eigenvalue equation for the *TE*-mode

$$\tan qh = j\frac{q}{k_y} \tag{4.27b}$$

It is noted, for future use, that, with the above choice of voltage amplitudes, $\overleftrightarrow{Y}$ represents the complex power of the transverse equivalent circuit.

It can also be seen that the occurrence of a pole of g in the complex k_y^2-plane at $k_y^2 = k_{ys}^2$, say, coincides with the vanishing of the total susceptance of the transverse equivalent network. It is then possible to make the identification

$$\psi_s(y) = \frac{\overleftarrow{V}(y;k_{ys}^2)}{\left(-j\omega\mu_0 \frac{\partial}{\partial k_y^2} \overleftrightarrow{Y}\Big|_{k_{ys}^2}\right)^{1/2}} \qquad :y < 0 \tag{4.28}$$

and similarly for $y > 0$, yielding the well known expression for the *TE*-surface wave of a grounded slab.

$$\psi_s(y) = A_s \frac{\sin q_s(y+h)}{\sin q_s h} \qquad y \le 0 \tag{4.29a}$$

$$= A_s e^{-\gamma_s y} \qquad y \ge 0 \tag{4.29b}$$

with

$$A_s = \left(\frac{2}{h + \frac{1}{\gamma_s}}\right)^{1/2} \sin q_s h$$

$$\gamma_s + q_s \cot q_s h = 0 \tag{4.30}$$

A substantially analogous procedure leads to the determination of the component of the continuum $\psi(y;k_y)$. The only difference between the surface modes and the radiation modes is that we no longer require the fields to decay exponentially outside of the slab. For the continuum it is not sufficient to allow k_y of (4.25) to become real. Real values of

k_y result in traveling waves outside the slab. It is impossible to satisfy the boundary conditions with traveling waves. Standing waves are needed to satisfy the boundary value problem. Adding to it another traveling wave moving in the opposite direction provides us a standing wave.

Let us introduce in (4.27) the following quantity of convenience:

$$\cot \alpha = \frac{q}{k_y} \cot qh \tag{4.31}$$

and substitute (4.31) in (4.26). The resulting expression for a component of the continuum corresponding to the value k_y, $0 \le k_y < \infty$ of the y-directed wavenumber is then

$$\psi(y;k_y) = \sqrt{2/\pi} \sin \alpha \frac{\sin q(y+h)}{\sin qh} \qquad y \le 0 \tag{4.32a}$$

$$= \sqrt{2/\pi} \sin (k_y y + \alpha) \qquad y \ge 0 \tag{4.32b}$$

which satisfy implicitly the orthonormalization condition (4.22). It is noted that the angle α above represents in fact the phase shift a ray with propagation constant (k_y,β) undergoes upon impinging on the slab and reemerging from it.

4.2.4 The Range of the Guided and Radiation Modes

We have discovered that dielectric waveguides possess a discrete spectrum of guided modes and a continuous spectrum of radiation modes. We must, however, investigate the range of possible eigenvalue (propagation constants) of the two sets of modes.

From (4.20) and (4.24), for discrete modes k_y is imaginary, q is real. That limits the range of β to the following interval

$$k_0^2 < \beta_s^2 < \varepsilon_r k_0^2$$

Radiation modes are obtained for $0 \le k_y < \infty$. The range of possible β values for the radiation modes is composed of two parts. Corresponding to $0 \le k_y \le k_0$, we obtain

$$0 \le \beta \le k_0$$

This range of β describes propagating radiation modes. Corresponding to $k_0 \le k_y < \infty$, imaginary values of β are obtained.

$$\beta_r = -i\,|\beta_r|$$
$$0 < |\beta_r| < \infty$$

This range of β corresponds to evanescent radiation modes.

The ranges of the possible values of β for different modes are shown in Fig.(4.4a). The corresponding ranges on the λ-plane ($-\beta^2$-plane) and $\hat{\lambda}$-plane (k_y^2-plane) are shown in Figs.(4.4b) and (4.4c), respectively, where $\hat{\lambda} = \lambda + k_0^2 = k_0^2 - \beta^2 = k_y^2$.

The integration in (4.18) is represented diagrammatically in Fig.(4.4c). It may be seen that the contributions to the integral of the Green function arise from a finite number of poles corresponding to discrete, "surface wave", modes, plus an integral along the branch cut, taking a more general form of equation (4.18)

$$-\frac{1}{2\pi j}\oint_c g(y,y';\lambda)\,d\lambda = \frac{\delta(y-y')}{w(y)}$$

$$= \sum_m \psi_m(y)\,\psi_m(y') + \int_{\substack{branch\\ cut}} \psi(y;\hat{\lambda})\,\psi(y;\hat{\lambda})\,d\hat{\lambda} \qquad (4.33)$$

Having extracted the contribution of the discrete poles, there remains to evaluate the branch-line integral. This integral, I_c say, may be written as:

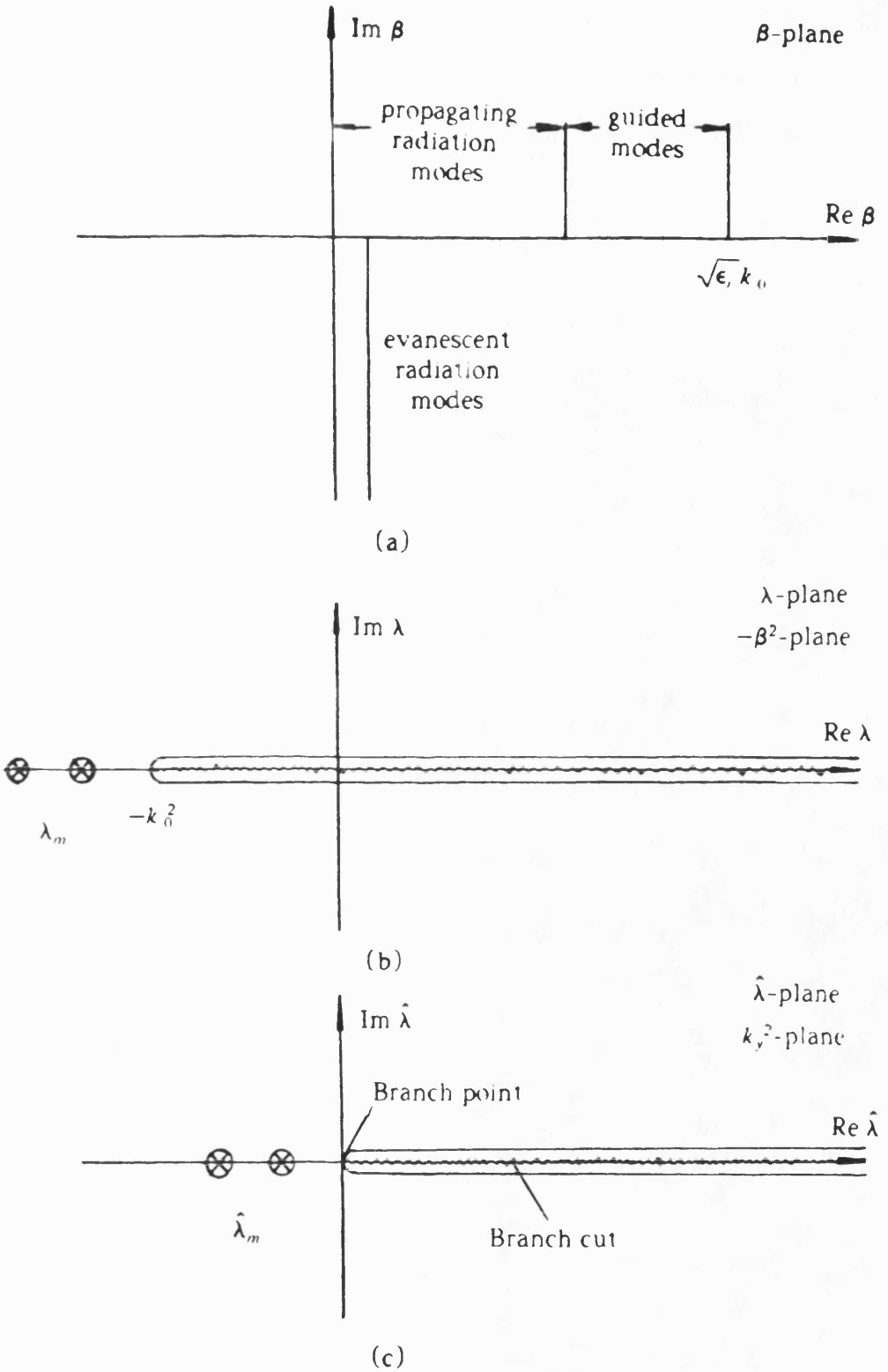

Figure 4.4 Spectral range of guided and radiation modes of dielectric waveguide

$$I_c = -\frac{1}{2\pi j}\left(\int_{\infty e^{j0}}^{0} + \int_{0}^{\infty e^{-j0}}\right) g(y,y';\lambda)\, d\hat{\lambda}$$

$$= -\frac{1}{2\pi j}\int_{0}^{\infty e^{-j0}} (g(\hat{\lambda} - k_0^2) - g(\hat{\lambda}\, e^{-j2\pi} - k_0^2))d\hat{\lambda}$$

$$= -\frac{1}{\pi}\mathrm{Im}\int_{0}^{\infty e^{-j0}} g(y,y';\hat{\lambda} - k_0^2)d\hat{\lambda}$$

$$= -\frac{2}{\pi}\mathrm{Im}\int_{0}^{\infty} k_y g(y,y';k_y^2 - k_0^2)dk_y \qquad (4.34)$$

Substituting (4.16a) into (4.34), we obtain

$$I_c = \frac{2}{\pi}\int_0^{\infty} k_y \,\mathrm{Re}\left(\frac{\overleftarrow{V}(y_<,y_0)\,\overrightarrow{V}(y_>,y_0)}{\omega\mu_0\,\overleftrightarrow{Y}(y_0,k_y^2)}\right)dk_y$$

$$= \int_0^{\infty} \psi(y,k_y)\,\psi(y',k_y)\,dk_y \qquad (4.35)$$

4.3 Normalization of the Discrete Spectrum of the IDG

We are now in a position to generalize the previous procedure to the two dimensional case such as *IDG* The unnormalized hybrid discrete modes were derived in [4] by means of the Transverse Resonance Diffraction method (*TRD*). We will now proceed to consider their normalization in such a manner that

$$\iint_s \psi_s(x,y)\,\psi_r(x,y)\,dx\,dy = \delta_{sr} \qquad (4.36)$$

For a relatively deep slot, we are using *LSE* description. As mentioned in Section 4.1, in this case $E_y = 0$. The fields then can be described by means of a magnetic Hertzian potential

$$\Pi_h = \mathbf{y}\, \psi_h\, e^{-j\beta z} \tag{4.37}$$

where **y** is the unit vector in the y-direction. From (4.37), the fields are given by

$$\mathbf{E} = -j\, \omega\, \mu_0\, \nabla \times \Pi_h \tag{4.38a}$$

$$\mathbf{H} = \varepsilon_r k_0^2\, \Pi_h + \nabla\nabla\cdot\Pi_h \tag{4.38b}$$

or, componentwise, omitting the propagation factor $e^{-j\beta z}$

$$H_x = \partial_x \partial_y \psi_h \tag{4.39a}$$

$$H_y = (\partial_y^2 + \varepsilon_r k_0^2)\, \psi_h \tag{4.39b}$$

$$H_z = -j\beta\, \partial_y \psi_h \tag{4.39c}$$

$$E_x = \omega\mu_0\, \beta\, \psi_h \tag{4.39d}$$

$$E_y = 0 \tag{4.39e}$$

$$E_z = -j\omega\mu_0\, \partial_x\, \psi_h \tag{4.39f}$$

The distribution of E_x at the interface $y = 0$ was expanded in terms of the even ordered Gegenbauer polynomials [5]

$$C_m^{1/6}(2x)$$

orthogonal in the range $0 \le x \le \frac{1}{2}$ with respect to the weight function

$$W(x) = (1 - (2x)^2)^{-1/3}$$

which implicitly satisfies the edge condition at the 90^0 corners, thus ensuring rapid convergence. We had, namely, the expression:

$$\psi_s(x, 0) = W(x) \sum_{m=0}^{2(M-1)} X_m\, C_m^{1/6}(2x) \tag{4.40}$$

The M-dimensional vector **X** resulted, within an undetermined constant, (its norm), from the application of the transverse resonance condition in the form of a diffraction integral (*TRD*). Owing to the convergence properties of (4.40), in fact, often just a single term suffices. Now we seek to determine that constant so that the normalization condition (4.36) is satisfied.

The field at the interface can also be expressed in terms of the discrete Fourier components in the slot as

$$\psi_s(x, 0) = \sum_{n=0}^{\infty} E_n \phi_n(x) \tag{4.41}$$

where,

$$\phi_n = \delta_n \cos n\pi x$$

where $\delta_0 = \sqrt{2}$ and $\delta_n = 2$ when $n > 0$ and

$$\int_0^{1/2} \phi_m \, \phi_n \, dx = \delta_{mn}.$$

By orthogonality over the slot, we have

$$E_n = \sum_{m=0}^{2(M-1)} P_{mn} \, X_m = \mathbf{P}_n^T \cdot \mathbf{X} \tag{4.42}$$

with

$$P_{mn} = \int_0^{1/2} W(x) \, C_m^{1/6}(2x) \, \phi_n(x) \, dx \tag{4.43}$$

$$= \frac{\delta_n \, (-1)^{m/2} \, \pi \, \Gamma(m + \frac{1}{3}) \, J_{m+1/6} \, (n\pi)}{2 \, m! \, \Gamma(1/6) \, (n\pi)^{1/6}}$$

as given in [4].

The field anywhere in the slot can therefore be expressed as

$$\psi_s(x,y) = \sum_{n=0}^{\infty} E_n \, \phi_n(x) \, \chi_n(y) \tag{4.44}$$

where $\chi_n = \dfrac{\sin q_n(y + h)}{\sin q_n h}$, $\quad q_n^2 = \varepsilon_r k_0^2 - \beta^2 - (n\pi)^2$

The field at the interface can also be expressed in terms of the continuous Fourier components in the air region as

$$\psi_s(x,0) = \int_0^\infty dk_x \, \tilde{E}(k_x)\sqrt{2/\pi} \cos k_x x$$

From which

$$\tilde{E}(k_x) = \mathbf{P}^T(k_x) \cdot \mathbf{X} \tag{4.45}$$

and the elements of the vector **P** are given by

$$P_m(k_x) = \int_0^{1/2} W(x)\, C_m^{1/6}(2x)\, \sqrt{2/\pi} \cos k_x x \, dx \tag{4.46}$$

$$= \sqrt{2/\pi}\, \frac{1}{\delta_n} P_{mn}$$

$n\pi = k_x$ as (4.43) is valid for any real n.

The field any where in the air region can then be expressed as:

$$\psi_s(x,y) = \int_0^\infty dk_x \sqrt{2/\pi} \cos k_x x \; e^{-jk_y y} \, \mathbf{P}^T(k_x) \cdot \mathbf{X} \tag{4.47}$$

It is noted explicitly that for a discrete mode, the value $k_{ls}^2 = k_0^2 - \beta_s^2$ is fixed by the transverse resonance condition [4]. As (4.47) is a Fourier expansion in k_x, taken now as an independent variable, we must choose k_y such as

$$k_{ys} = \sqrt{k_{ls}^2 - k_x^2} \qquad k_{ls} \geq k_x$$

$$= -j\sqrt{k_x^2 - k_{ls}^2}$$

The amplitudes $E_n, \tilde{E}(kx), X_m$ can be interpreted as voltages in the the equivalent network of Fig.4.5 as indicated. This network allows us to write by inspection the total transverse admittance matrix , as seen at the reference places of the interface, in the representation of (4.40). Looking into the slot region, this is elementwise:

$$\omega\mu_0 \overleftarrow{Y}_{km} = -j \sum_n q_n \cot q_n h \, P_{kn} \, P_{mn} \tag{4.48a}$$

or in matrix form

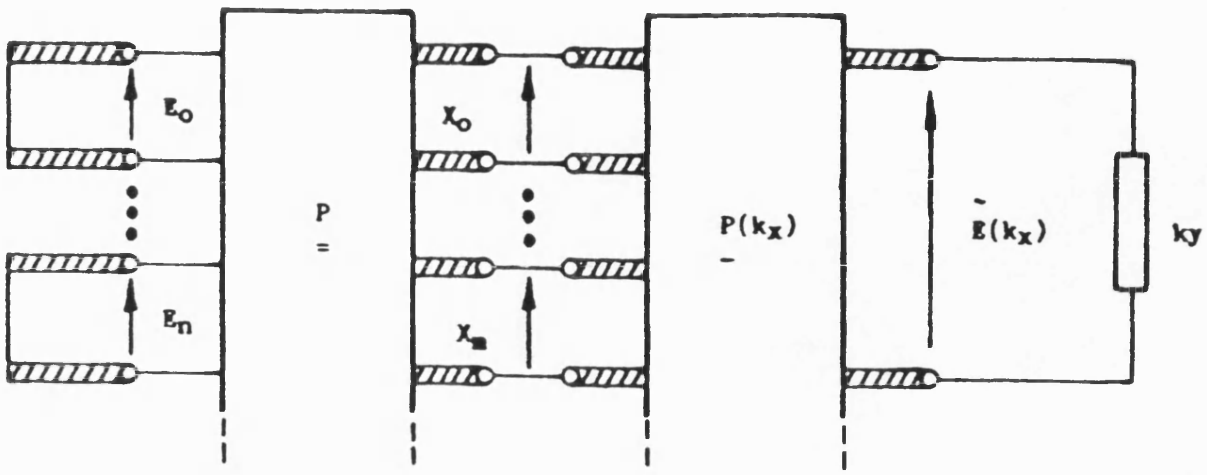

Figure 4.5 Transverse equivalent circuit for the orthonormalisation of the discrete modes of the *IDG*

$$\omega\mu_0 \overleftarrow{\mathbf{Y}} = -j \sum_n q_n \cot q_n h \, \mathbf{P}_n \cdot \mathbf{P}_n^T \tag{4.48b}$$

Similarly, looking into the air region,

$$\omega\mu_0 \overrightarrow{\mathbf{Y}} = \int_0^\infty k_y(k_x) \, \mathbf{P}(k_x) \cdot \mathbf{P}^T(k_x) \, dk_x \tag{4.49}$$

It is now recalled that the normalization factor in the denominator of (4.16a) is just $j\omega\mu_0$ times the complex power for unit voltage at the reference plane $y = 0$ in the one-port situation of Fig.(4.1b)

In the multiport situation of Fig.(4.5), where the voltage at the reference plane are expressed by the vector **X**, the equivalent is given by the scalar

$$p = j\omega \mu_0 \, \mathbf{X}^T \cdot \mathbf{Y} \cdot \mathbf{X} \equiv \omega\mu_0 \mathbf{X}^T \cdot \mathbf{B} \cdot \mathbf{X} \tag{4.50}$$

where

$$\overleftrightarrow{\mathbf{Y}} = \overleftarrow{\mathbf{Y}} + \overrightarrow{\mathbf{Y}} = j\overleftrightarrow{\mathbf{B}}$$

By partial differentiation with respect to k_y^2 at $k_y^2 = k_{ys}^2$ we obtain the actual normalization factor of the discrete modes

$$N_s = \frac{\partial p}{\partial k_y^2} \Big\lfloor_{k_{ys}^2} = \omega\mu_0 \, \mathbf{X}^T \cdot \frac{\partial \mathbf{B}}{\partial k_y^2} \Big\lfloor_{k_{ys}^2} \cdot \mathbf{X} \tag{4.51}$$

$$= \frac{\omega\mu_0}{2} \mathbf{X}^T \cdot \left(\sum_{n=0}^{\infty} \frac{1}{q_n} (q_n h \, \mathrm{cosec}^2 \, q_n h - \cot q_n h) \mathbf{P}_n \cdot \mathbf{P}_n^T - j \int_0^\infty \frac{dk_x}{k_{ys}} \mathbf{P}(k_x) \cdot \mathbf{P}^T(k_x) \right) \cdot \mathbf{X}$$

Upon use of (4.43), (4.47) it is straightforward to check by direct quadrature that the above expression just equals

$$N_s = \sum_n E_n^2 \frac{\partial}{\partial k_y^2} (-q_n \cot q_n h) + \int_0^\infty dk_x \tilde{E}^2(k_x) \frac{\partial}{\partial k_y^2} (-jk_y) \tag{4.52}$$

$$= \iint_s \psi_s^2(x,y) \, dx \, dy$$

where it is noted that the derivative of the susceptance for the n-th or k_x-Fourier component is, in fact, identical to the integral of the square of the y-dependence.

In conclusion, if the as yet unspecified norm of **X** is chosen so that $N_s = 1$ in (4.51), the orthonormalized distribution of the discrete mode is given by (4.43) for $y \leq 0$ and by (4.47) for $y \geq 0$.

4.4 Determination of the Orthonormalized Continuous Spectrum of the IDG

Unlike the discrete spectrum, derived previously in [4] within a normalization constant, N_s, which could always be determined by direct quadrature, the continuum was not reported before [6] was published. It constitutes, in fact, an example of a two-dimensional, non-separable problem which can not be reduced to a uniform spectral domain description because of the change of cross-section at the interface.

As the cross-section is two-dimensional, it is apparent that an expansion of the continuum can be written in terms of two independent wavenumbers, the third being fixed by the wave equation. We choose $(k_x, k_y) = \mathbf{k}_t$ as the two independent quantities and, correspondingly, develop the field in the air region in terms of partial waves of the type

$$\sqrt{2/\pi}\cos k_x x \;\; \sqrt{2/\pi}\sin(k_y y + \alpha) \tag{4.53}$$

which highlights the correspondence with the slab case as $k_x \to 0$. It is noted, however, that the 'phase shift' α, is now a function of both k_x and k_y because of the nonseparability caused by the presence of the corners.

We require that the components of the continuum satisfy the orthogonality conditions:

$$\iint_S \psi(x,y;k_x,k_y)\,\psi(x,y;k_x',k_y')\,dx\,dy = \delta(k_x-k_x')\cdot\delta(k_y-k_y')$$

$$\equiv \delta(\mathbf{k}_t-\mathbf{k}_t') \tag{4.54}$$

In the treatment of the discrete spectrum, we found it convenient to expand the field at the interface in terms of discrete basis functions individually satisfying the edge conditions at the metal corners. This is not required of individual components of the continuum, but only of the total field. Therefore in consideration of the partial waves expression (4.54) we now find it convenient to expand the field at the interface directly in terms of the x-dependence of the partial waves, i.e. a continuum in k_x. This fact imposes a generalization to the concept of the discrete transverse admittance matrix **Y** we met in the previous section as follows.

The transverse equivalent circuit appropriate to the new situation is shown in Fig.4.6. The discontinuous interface acts as an ideal transformer coupling slot components with a different wavenumber $n\pi$ and partial waves in air with different wavenumber k_x.

Consider an outward traveling partial wave in the air region with wavenumber $\mathbf{k}_t$ and Fourier amplitude $\tilde{E}(\mathbf{k}_t)$:

$$\vec{V}(x,y;\mathbf{k}_t) = \tilde{E}(\mathbf{k}_t)\sqrt{2/\pi}\,\cos k_x x\, e^{-jk_y y} \tag{4.55}$$

correspondingly, there exists a standing wave in the slot expressible as

$$\overleftarrow{V}(x,y;\mathbf{k}_t) = \sum_{n=0,2,\ldots}^{\infty} Q_n(k_x)\,\phi_n(x)\chi_n(y) \tag{4.56}$$

the scalar continuity condition is replaced by

$$\overleftarrow{V}(x,0;\mathbf{k}_t) = \vec{V}(x,0;\mathbf{k}_t) \tag{4.57}$$

which allows the coefficients Q_n in (4.56) to be determined by orthogonality of the ϕ_n's over the slot:

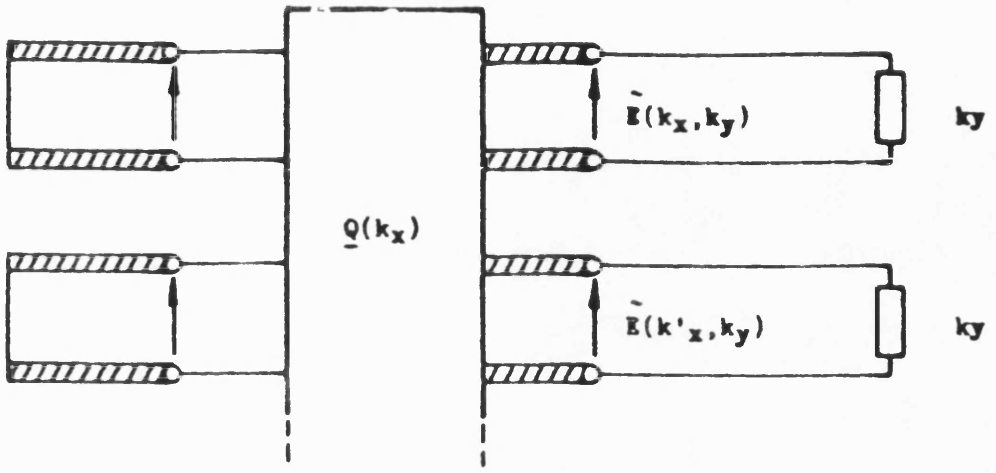

Figure 4.6 Transverse equivalent circuit for deriving the orthonormalised continuum of the *IDG*

$$Q_n(k_x) = \sqrt{2/\pi}\ \delta_n\ (-1)^{n/2} \sin\frac{k_x}{2}\ \frac{k_x}{k_x^2 - (n\pi)^2}\tilde{E}(\mathbf{k}_t) \tag{4.58}$$

Also from the equivalent circuit of Fig.4.6, the susceptance looking into the slot, as seen from reference planes at $y = 0^+$ is given by the parallel combination of the transverse transmission lines, corresponding to the various value of n in the slot, terminated by a short circuit at $y = -h$, as seen via the transformer Q, namely

$$\omega\mu_0\ \overleftarrow{B}\ (k_x, k_x') = -\sum_n q_n cot\ q_n h\ Q_n(k_x)\ Q_n(k_x') \tag{4.59}$$

In the air region, two different components k_x and k_x' do not couple and a component (a ray) with y-directed wavenumber k_y propagates in the positive y-direction with a characteristic admittance $k_y/\omega\mu_0$. These facts imply that the admittance is a delta function of k_x with amplitude k_y, namely

$$\omega\mu_0\ \overrightarrow{B}(k_x, k_x') = \frac{1}{j}\ k_y\ \delta\ (k_x - k_x') \tag{4.60}$$

Let $B(k_x, k_x') = \overleftarrow{B} + \overrightarrow{B}$. If $\tilde{E}(\mathbf{k}_t)$ is set equal to unity in (4.55) the complex power (times $-j\omega\mu_0$) corresponding to the component $\mathbf{k}_t = (k_x, k_y)$ is then given by

$$\begin{aligned} p(\mathbf{k}_t) &= \omega\mu_0\ \tilde{E}(\mathbf{k}_t) \int_0^\infty B(k_x, k_x')\ \tilde{E}(k_x', k_y)\ dk_x' \\ &= \omega\mu_0 \int_0^\infty B(k_x, k_x') dk_x' \end{aligned} \tag{4.61}$$

Hence, from (4.59) and (4.60)

$$p = \frac{1}{j}\ k_y - \sum_n q_n\ cot\ q_n h \sqrt{\pi/2}\ \delta_n\ Q_n(k_x) \tag{4.62}$$

as

$$\int_0^\infty Q_n(k_x)\ dk_x = \sqrt{\pi/2}\ \delta_n$$

It is again useful to define quantity of convenience $\alpha(k_x, k_y)$ such that

$$cot\ \alpha = \frac{1}{k_y} \sum_n q_n\ cot\ q_n h\ \sqrt{\pi/2}\ \delta_n\ Q_n(k_x) \tag{4.63}$$

using (4.63) in (4.26), we have then

$$\frac{2}{\pi} k_y \mathrm{Re}\left(\frac{\overleftarrow{V}\ \overrightarrow{V}}{k_y - jk_y cot\ \alpha} \right) = \sqrt{2/\pi} \sum_n Q_n\ \phi_n(x)\ \chi_n(y) \sin\alpha \cdot \frac{2}{\pi} \cos k_x x' \sin(k_y y' + \alpha)$$

$$\equiv \psi(x,y;\mathbf{k}_t)\ \psi(x',y';\mathbf{k}_t) \tag{4.64}$$

from which the components of the continuum can be identified as

$$\psi(x,y;\mathbf{k}_t) = \sqrt{2/\pi} \sin\alpha(\mathbf{k}_t) \sum_n Q_n(k_x)\ \phi_n(x)\ \chi_n(y) \ :\quad y \le 0$$

$$= \frac{2}{\pi} \cos k_x x \sin(k_y y + \alpha) \ :\quad y \ge 0 \tag{4.65}$$

It can be checked by direct integration that the orthonormalization condition (4.54) over the cross-section is indeed satisfied by (4.65) (See Appendix 4.1).

4.5 The Green Function of the IDG

Having constructed the complete, orthonormalized spectrum of the *IDG* for E^x polarization, we are now in a position to formulate its scalar Green's function. The latter is a prerequisite for the solution of discontinuity problems.

The scalar Green's function $G(\mathbf{r}-\mathbf{r}')$ is the solution of the inhomogeneous wave equation with a delta function source located at $\mathbf{r}'$, namely

$$\nabla^2 G + \varepsilon_r k_0^2\ G = \delta(\mathbf{r}-\mathbf{r}') \tag{4.66}$$

with the boundary conditions appropriate to E_x. This should not be confused with the two dimensional g used in section 4.2, which refers to the transverse wave equation, in the process of determining the spectrum of the guide.

In as much as the normalized mode spectrum is now known, the Green function, solution of (4.66) is found by the classical method of expansion in eigen modes [7], right and left of the source function ($z \leq z'$ and $z \geq z'$).

By imposing the continuity of G at the source point $z = z'$ and by condition that its derivative be discontinuous there by the unit step, we recover the classical expression for the eigenmode expansion of the Green function valid at each side of the source point:

$$G(\mathbf{r},\mathbf{r}') = \sum_s \frac{1}{2j\beta_s}\, \psi_s(x,y)\, \psi_s(x',y')\, e^{-j\beta_s |z-z'|} \tag{4.67}$$

the summation being over the spectrum. Referring in particular, to a waveguide with a single bound mode and making explicit the contribution of the continuum, (4.67) can be rewritten as

$$G(\mathbf{r},\mathbf{r}') = \frac{1}{2j\beta_s}\, \psi_s(x,y)\, \psi_s(x',y')\, e^{-j\beta_s |z-z'|} + \int_0^\infty dk_x \int_0^\infty dk_y \frac{e^{-j\beta|z-z'|}}{2j\beta}\, \psi(x,y;\mathbf{k}_t)\, \psi(x',y';\mathbf{k}_t) \tag{4.68}$$

where $\beta = \sqrt{k_0^2 - k_t^2}$.

The evaluation of the double integral in the wavenumber space is conveniently carried out by trigonometric transformations, as illustrated in Fig.4.7. These are

$$\beta = k_0 \cos\eta \tag{4.69a}$$

$$k_t = k_0 \sin\eta \tag{4.69b}$$

$$k_x = k_t \cos\theta \tag{4.69c}$$

$$k_y = k_t \sin\theta \tag{4.69d}$$

owing to (4.69), we have

$$\frac{dk_x\, dk_y}{\beta} = \frac{k_t dk_t\, d\theta}{\beta} = k_t d\eta\, d\theta$$

Regarding the path of integration in the η and θ planes, in as much as we have chosen

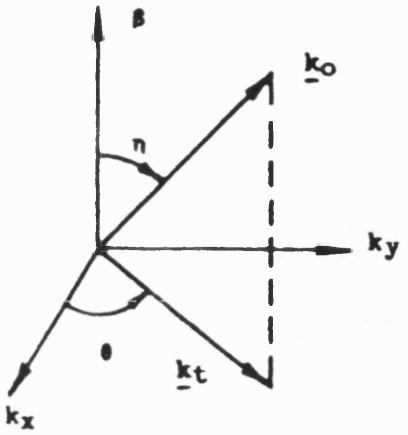

Figure 4.7 Trigonometric decomposition of the wavenumber.

expansions in terms of k_x, k_y real and such that $0 \le k_x, k_y < \infty$, θ is a real angle

$$0 \le \theta \le \frac{\pi}{2}$$

The integration in the complex η-plane, however, runs over the real interval

$$0 \le \mathrm{Re}\,\eta \le \frac{\pi}{2}, \quad \mathrm{Im}\,\eta = 0$$

and then over the imaginary interval:

$$\mathrm{Re}\,\eta = \frac{\pi}{2}, \quad 0 \le \mathrm{Im}\,\eta < \infty$$

If the non-radiative continuum, corresponding to $k_t > k_0$ is neglected, then so is the contribution of the latter interval and η is a real angle

$$0 \le \eta \le \frac{\pi}{2}$$

The above trigonometric transformation is in fact a preliminary to the evaluation of the far field radiated by a dipole.

4.6 Scattering by a Small, Thin, Transverse Dipole on the Air-Dielectric Interface.

The transverse electric field at the air-dielectric interface $y = 0$, is near its maximum value. The interface also constitutes the most accessible plane of the guide. This is therefore an ideal location for a source, such as a dipole, placed across the slot aperture or for a discontinuity, such as a metal strip or disk, with a view to realising circuit elements or a leaky wave antenna. As an example of application of the Green function(4.68) we shall therefore consider the scattering by a small, thin transverse current element, representing an independent source of an induced one, located at $z = 0$, sufficiently thin and small to be representable as

$$J(x,z) = J_0\,\delta(z) \quad 0 \le |x| < l/2$$
$$= 0 \qquad\quad l/2 \le |x| \tag{4.70}$$

with constant J_0. The scalar Green's function (4.68) is that pertaining to an x-directed electric field distribution assumed as the source of the e.m. field. If the source term is constituted by an x-directed electric current J, then the electric field E_x is related to G through the x-component of the vector potential A, given by

$$A_x(\mathbf{r}) = -\mu_0 \int_{-l/2}^{l/2} G(\mathbf{r}; x',0,0)\, J(x')\, dx' \tag{4.71}$$

and the resulting scattered field is

$$E_x^s = -j\,\omega\, A_x + \frac{1}{j\,\omega\,\mu_0\varepsilon_r\varepsilon_0}\,\frac{\partial^2}{\partial x^2}\,A_x \tag{4.72}$$

$$= j\,\omega\,\mu_0 \int_{-l/2}^{l/2} (1 + \frac{1}{\varepsilon_r k_0^2}\,\frac{\partial^2}{\partial x^2})\, G\, J(x')\, dx' \tag{4.73}$$

$$= \frac{\omega\,\mu_0}{2}\, J_0 \cdot \left(\frac{\tilde{\psi}_s(x,y)}{\beta_s} D_s\, e^{-j\beta_s |z|} + \int_0^{\pi/2} d\eta \int_0^{\pi/2} d\theta\, k_0 \sin\eta\, \tilde{\psi}(x,y;\eta,\theta)\, D(\eta,\theta)\, e^{-jk_0 \cos\eta |z|} \right)$$

where

$$\tilde{\psi}_s = (1 + \frac{1}{\varepsilon_r k_0^2}\,\frac{\partial^2}{\partial x^2})\,\psi_s \tag{4.74a}$$

$$\tilde{\psi}(x,y;\eta,\theta) = (1 + \frac{1}{\varepsilon_r k_0^2}\,\frac{\partial^2}{\partial x^2})\,\psi(x,y;\eta,\theta) \tag{4.74b}$$

which can be evaluated directly from (4.44), (4.47) and (4.65) according as $y < 0$ (slot region, where $\varepsilon_r = 2.08$) or $y > 0$ (air region, where $\varepsilon_r = 1$).

In (4.73) we have

$$D_s = 2 \int_0^{l/2} dx' \psi_s(x',0) \approx X_0\, l(1 + (\frac{l}{3})^2) \tag{4.75}$$

using the expansion (4.40) with a single term, and

$$D(\eta,\theta) = 2\int_0^{l/2} \psi(x',0;\eta,\theta)\, dx'$$

$$= \frac{4}{\pi} \sin\alpha(\eta,\theta) \frac{\sin(\sin\eta\cos\theta \frac{k_0 l}{2})}{k_0 \sin\eta\cos\theta} \tag{4.76}$$

where

$$cot\,\alpha = \frac{1}{k_0 \sin\eta\cos\theta} \sum_{n=0,2,\ldots}^{\infty} \sqrt{\pi/2}\, \delta_n\, Q_n\, q_n\, cot\, q_n h \tag{4.77a}$$

$$q_n^2 = v^2 - (n\pi)^2 + k_0^2 \sin^2\eta \tag{4.77b}$$

$$Q_n = \sqrt{2/\pi}\, \delta_n\, (-1)^{(n/2)} \sin(\frac{k_0}{2} \sin\eta\cos\theta) \frac{k_0 \sin\eta\cos\theta}{(k_0 \sin\eta\cos\theta)^2 - (n\pi)^2} \tag{4.77c}$$

In spite of its apparent complexity, the double integral (4.73) is in fact amenable to straightforward numerical integration. Moreover the trigonometric form of the integrand lends itself naturally to the evaluation of the far field by the saddle point method.

4.7 Far Field Pattern of the Dipole. Excitation of the Fundamental Mode.

The evaluation of the far field is effected by going over to cylindrical coordinates in the radiation integral in (4.73), as shown in Fig.4.8:

$$x = R\cos\gamma$$

$$y = R\sin\gamma$$

so that

$$k_x x + k_y y = k_0 R \sin\eta\cos(\theta - \gamma) \tag{4.78}$$

Upon using the symmetry of the integrand with respect to θ, the radiation integration in (4.73) can be rewritten as

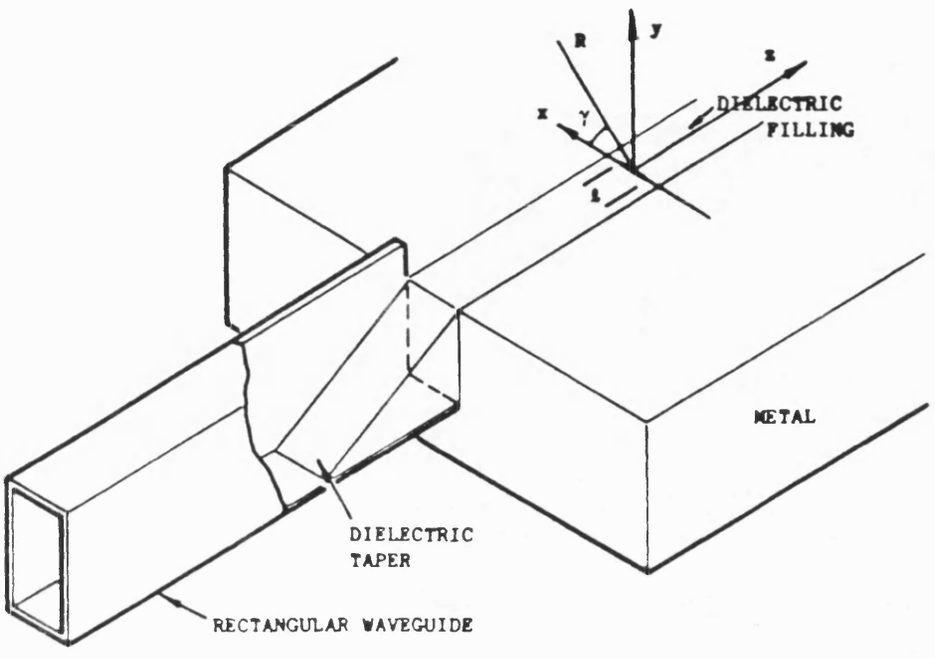

Transverse dipole on IDG

Figure 4.8 Transverse dipole on *IDG* ,
showing transition from rectangular waveguide.

$$E_x^s = \frac{j\omega\mu_0}{4\pi} J_0 \int_0^{\pi/2} d\eta \int_{-\pi}^{\pi/2} d\theta\, k_0 \sin\eta\,(1-\sin^2\eta\cos^2\theta)\, D(\eta,\theta)$$
$$\cdot e^{-j\alpha} \cdot e^{-jk_0 R\sin\eta\cos(\theta-\gamma)} \tag{4.79}$$

there is no pole in the integrand, so that when $k_0R \gg 1$, by using the saddle point method (see Appendix 4.2) we obtain

$$E_x^s \approx -\frac{\omega\mu_0 J}{2R} \sin^2\gamma\, D(\frac{\pi}{2}, \gamma)\, e^{-j\alpha(\pi/2,\gamma)}\, e^{-jk_0 R} \tag{4.80}$$

the radiation pattern is then given by

$$f(\gamma) = \left| \frac{E_x^s(\gamma)}{E_x^s(\pi/2)} \right|^2 = \sin^4\gamma \left| \frac{D(\pi/2,\gamma)}{D(\pi/2,\pi/2)} \right|^2 \tag{4.81}$$

From (4.76) and (4.77), we deduce

$$D(\pi/2,\ \gamma) = \frac{4}{\pi} \sin\alpha(\pi/2,\gamma)\, \frac{\sin(\frac{k_0 l}{2}\cos\gamma)}{k_0\cos\gamma} \tag{4.82a}$$

$$D(\pi/2,\pi/2) = \frac{2l}{\pi} \tag{4.82b}$$

hence, the resulting radiation pattern is:

$$f(\gamma) = \left(\frac{\pi}{2l} \sin^2\gamma\, D(\pi/2,\gamma) \right)^2 \tag{4.83}$$

showing the influence of the *IDG* geometry on the radiation pattern while $\sin^2\gamma$ represents the usual pattern of a dipole in an infinite space. The radiation pattern is plotted in Fig.4.9 for various value of $k_0 l$, l/a.

The dipole also excites a forward- and a backward- traveling wave in the fundamental mode, whose amplitude is determined by multiplying (4.73) by ψ_s and integrating over s. This is

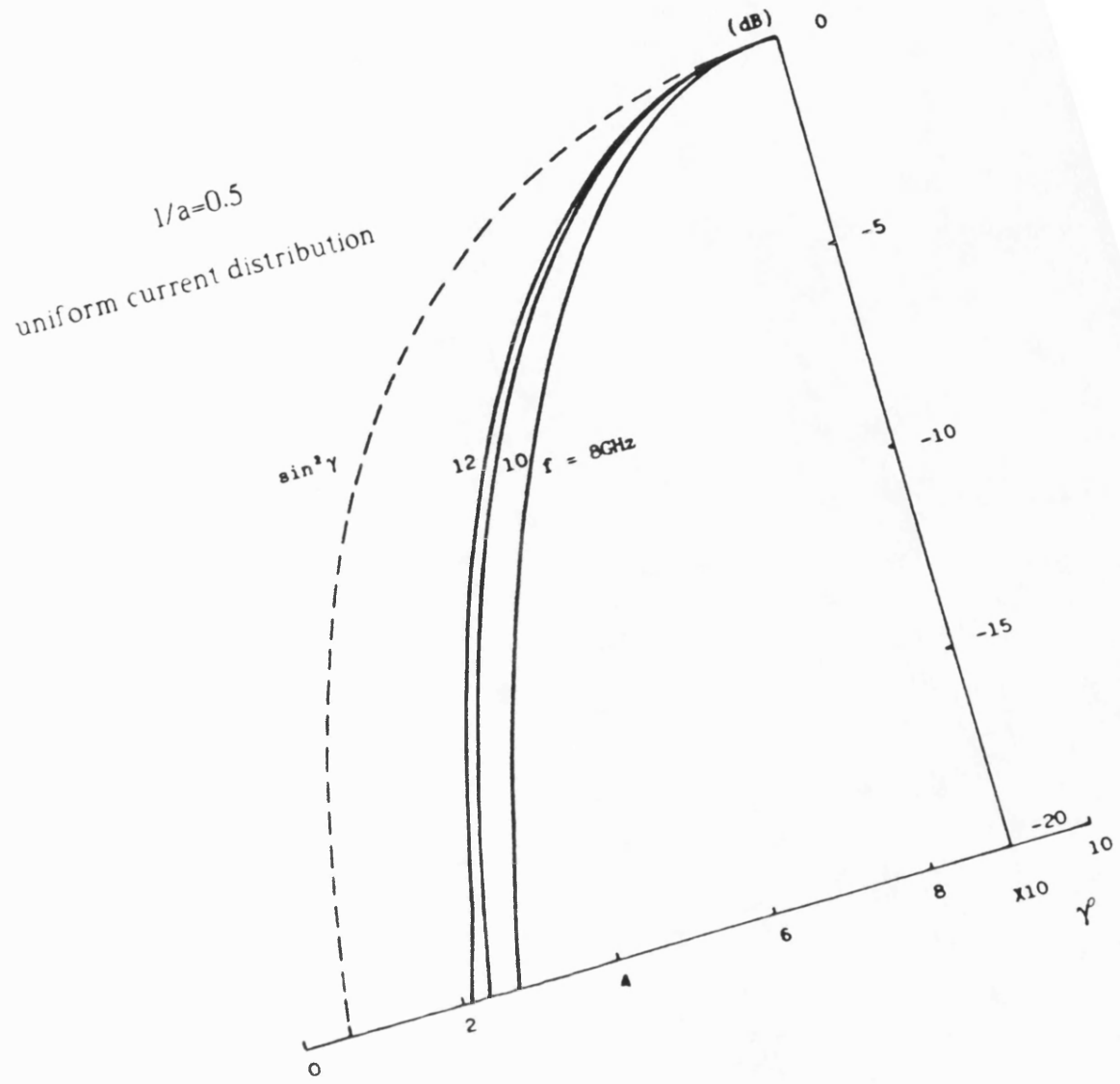

Figure 4.9 Far field pattern for the dipole of Fig.4.8

$$A_s^+ = A_s^- \approx \frac{\omega\mu_0}{2} J_0 \frac{D_s}{\beta_s} \iint_s \psi_s \, \psi_s \, dx \, dy \tag{4.84}$$

$$= \frac{\omega\mu_0}{2} J_0 \frac{D_s}{\beta_s}$$

where we have neglected weak overlapping terms of ψ_s with $\tilde{\psi}$ (radiation resistance) and $\frac{\partial^2}{\partial x^2} \psi_s$ (coupling different Fourier components in the slot).

In the above J_0 may be the amplitude of an independent source, say a dipole, or that of an induced one, say the current induced on a metal strip by the fundamental mode ψ_s itself, incident with unit amplitude. In the latter case, J_0 is determined rigorously by the condition that the total field on the metal strip vanishes.

Within the scope of small dipole approximation adopted in this section $J_0 = H_{zs}$ and again neglecting second derivatives with respect of x, i.e. by assuming the propagating mode to be pure *TE* rather than *LSE* and separable, and only retaining the contribution of the slot region, we further obtain

$$J_0 \approx \frac{1}{\omega\mu_0} \sum_n q_n \cot q_n h \, P_{0n}^2 \tag{4.85}$$

Hence by substituting the above approximate amplitude in (4.84), we can identify A_s^- with the reflection coefficient Γ of the metal strip, i.e.

$$\Gamma = A_s^- \approx \frac{\sum q_n \cot q_n h \, P_{0n}^2}{2\,\beta_s} \, l \, (1 + (l/3)^2) \tag{4.86}$$

which is valid for thin strips $l/a < 1$. When two identical dipoles are located a quarter wavelength apart, cancellation of the overall reflection coefficient occurs. This effect is illustrated in Fig.4.10, showing the magnitude of the reflection coefficient versus frequency for various dipole lengths, computed from (4.86) by elementary network analysis. The spacing between the two dipoles (0.6 cm) is such that $f_0 = 9.875 GHz$ corresponds to a quarter wavelength in the guide.

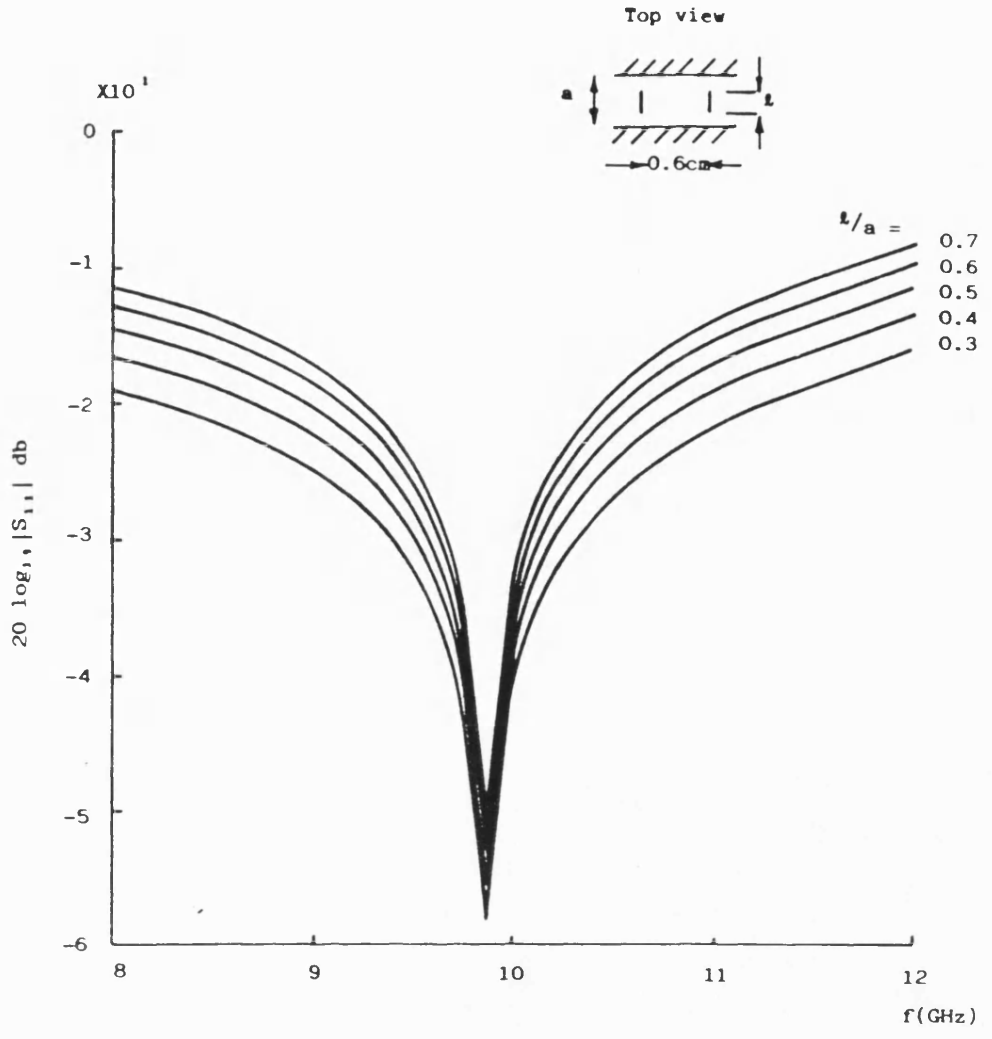

Figure 4.10 Reflection coefficient of a pair of dipoles for various dipole lengths.

Appendix 4.1 Direct Check on Orthonormality of the Continuum

We want to verify the condition

$$\iint_S dx\, dy\ \psi(x,y;\mathbf{k}_t)\ \psi(x,y;\mathbf{k}_t') = \delta(\mathbf{k}_t - \mathbf{k}_t') \tag{A4.1}$$

is satisfied by direct integration.

Define by I_1 the integral over the slot cross-section. This is given by

$$I_1 = \int_0^{1/2} dx \int_{-h}^{0} dy \sum_n Q_n(k_x)\, Q_n(k_x') \sin\alpha \sin\alpha'$$

$$\phi_n(x)\, \phi_n'(x)\, \frac{2}{\pi}\, \frac{\sin q_n(y+h)}{\sin q_n h}\, \frac{\sin q_n'(y+h)}{\sin q_n' h} \tag{A4.2}$$

where

$$\alpha' = \alpha(k_x', k_y')\ ;\quad q_n^2 = (\varepsilon_r - 1)\, k_0^2 - k_t^2 - (n\pi)^2.$$

By orthogonality of the ϕ_n and integration over y, we have

$$I_1 = \sum_n Q_n(k_x)\, Q_n(k_x') \cdot \frac{\sin\alpha}{\sin q_n h} \cdot \frac{\sin\alpha'}{\sin q_n' h} \cdot \frac{1}{\pi}$$

$$\left(\frac{\sin(q_n - q_n')h}{q_n - q_n'} - \frac{\sin(q_n + q_n')h}{q_n + q_n'} \right) \tag{A4.3}$$

$$= \frac{2}{\pi}\, \frac{\sin\alpha \sin\alpha'}{k_t^2 - k_t'^2} \sum_n Q_n(k_x)\, Q_n(k_x')\, (q_n' \cot q_n' h - q_n \cot q_n h)$$

In the air region, we have

$$I_2 = \int_0^{\infty} dk_x \int_0^{\infty} dk_y \frac{2}{\pi} \cos k_x x \cos k_x' x\, \frac{2}{\pi} \sin(k_y y + \alpha) \sin(k_y' y + \alpha')$$

$$= \delta(k_x - k_x') \left(\delta(k_y - k_y') - \frac{1}{\pi} \left(\frac{\sin(\alpha - \alpha')}{k_y - k_y'} - \frac{\sin(\alpha + \alpha')}{k_y + k_y'} \right) \right)$$

$$= \delta(k_x - k_x') \left(\delta(k_y - k_y') - \frac{2}{\pi}\, \frac{\sin\alpha \sin\alpha'}{k_y^2 - k_y'^2} (k_y' \cot\alpha' - k_y \cot\alpha) \right) \tag{A4.4}$$

Satisfaction of (A4.1) implies

$$I_1 + I_2 = \delta (k_x - k_x') \, \delta (k_y - k_y') \tag{A4.5}$$

If the second term in (A4.4) equals I_1, this is indeed the case. It is now verifiable that (A4.5) holds provided α is chosen such that

$$k_y \cot \alpha \, \delta (k_x - k_x') = \sum_n Q_n(k_x) \, Q_n(k_x') \, q_n \cot q_n h \tag{A4.6}$$

Integrating with respect to k_x' from 0 to ∞, we recover

$$k_y \cot \alpha = \sum_n \sqrt{\pi/2} \, \delta_n \, Q_n(k_x) \, q_n \cot q_n h \tag{A4.7}$$

which is just our definition (4.63) of α.

Appendix 4.2 The Evaluation of (4.79) by Using the Saddle Point Method (SPM)

The SPM is applicable, in general, to the integrals of the form:

$$f(z) = \int_{b_1}^{b_2} g(t)\, e^{z\, h(t)} dt \tag{A4.8}$$

where z is large and positive. The result of (A4.8) by using the SPM is:

$$f(z) \approx i\sqrt{2\pi/a\, z}\, g(t_0)\, e^{z\, h(t_0) - i\frac{\phi_0}{2}} \tag{A4.9}$$

where

$$h'(t_0) = 0 \tag{A4.10}$$

$$h''(t_0) = a\, e^{j\phi_0} \tag{A4.11}$$

There is no pole in the integrand of (4.79), moreover, $k_0 R$ is large and positive. Therefore, we can use the SPM to evaluate the double integral. If we use the SPM over θ first with η as a parameter and then use it over η, we find:

$$\theta_0 = \gamma \tag{A4.12}$$

$$\eta_0 = \pi/2 \tag{A4.13}$$

Substituting (A4.12), (A4.13) and the corresponding coefficiency into (4.79) yields (4.80).

REFERENCES

[1] L. Felsen and N. Marcuvitz, " Radiation and Scattering of Waves ", Prentice Hall 1973, Ch. 3, pp. 278-282.

[2] V.V. Shevchenko, " Continuous Transitions in Open Waveguides " The Golem Press 1971.

[3] D. Marcuse, " Light Transmission Optics "

[4] T. Rozzi and S. Hedges, " Rigorous analysis and network modeling of inset dielectric guide ", *IEEE Trans. Microwave Theory and Tech., vol. MTT*-35, pp. 823-834, Sep. 1987.

[5] I. S. Gradshteyn and I. M. Ryshik, *Table of Integrals, Series* and *Products*. New York: Academic Press, 1980, p. 827. Antennas ", *Military Microwaves* pp.123-138 June 1985.

[6] T. Rozzi and L. Ma, " Mode Completeness, Normalization, and Green's Function of the Inset Dielectric Guide ", *IEEE Trans. Microwave Theory and Tech., vol. MTT*-36, pp. 542-551, Mar. 1988.

[7] R. E. Collin, *Field Theory of Guided Waves*. New York: McGraw-Hill, 1960, p.18.

CHAPTER 5

EQUIVALENT NETWORK OF TRANSVERSE DIPOLE ON IDG APPLICATION TO LINEAR ARRAY

5.1 Introduction

Inset dielectric guide (*IDG*) is an alternative to Image Line, retaining most of its advantages without its main disadvantages. In particular, it is possible to realize low-cost leaky wave antennas with very pure polarization properties in *IDG* by laying thin metal strips (dipoles) on the air-dielectric interface.

The scattering properties of a single thin metal strip were analyzed in the previous chapter where the edge singularities were taken into proper account. In this chapter, a variational expression for the equivalent circuit of the radiating dipole will be derived and this information will be applied to the design of a tapered linear array by network methods. The array was built and tested and its performance was in excellent agreement with the theory.

5.2 Feasibility of IDG Leaky-Wave Antenna

This work was inspired by the previous successful realization of integrated leaky wave antennas constructed on a dielectric waveguide [1]-[5].

The possibility of realising low-cost, easy to fabricate, relatively high-quality antennas of the leaky-wave type based on the *IDG* configuration was the object of a feasibility study in [6]. It is very easy to lay thin, transverse metal strips on the air-dielectric interface, as shown in Fig.5.1, which act as dipole radiators. The operation principle is as follows: in the fundamental mode the main component of the electric field is x-directed and is not far from the maximum at the air-dielectric interface. Induced currents are therefore easily set up in the strips without twisting of the field lines, as is the case in microstrip patch antennas and image line antennas, operating in the fundamental *LSM*-mode. The strips in turn act as x-directed dipole radiators.

In order to verify feasibility, a 12-element linear array was coarsely designed and tested. As shown in Fig.5.1, the reflection due to the dipoles in the feed waveguide can be reduced by pairing two dipoles at a quarter wavelength apart, so as to achieve negative interference of the reflected wave, as shown in the theoretical curve of Fig.4.10 for a single pair of dipoles.

Constructive interference (array effect) is obtained by spacing each pair a guided wavelength apart. This is in accordance with well known design principles in the literature.

The launcher is matched by tapering the dielectric into the *IDG*, as shown in Fig.5.1. To achieve an approximate uniform amplitude distribution the lengths of the dipoles are tapered. To a smaller extent, the widths of the dipoles can also be adjusted.

Experiment took place, taking advantage of a Hewlett-Packard automated

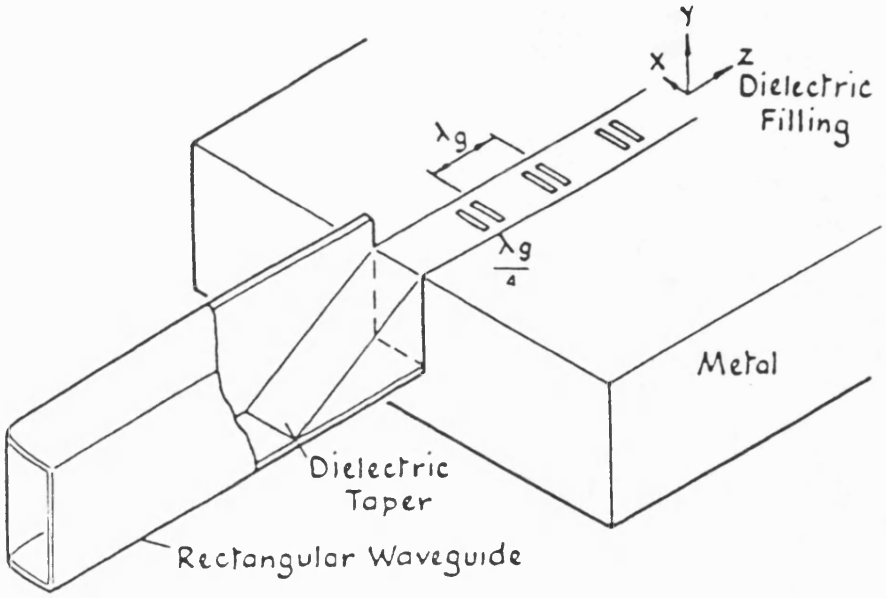

Figure 5.1 Layout of a vertically polarised leaky-wave array on *IDG* showing transition from rectangular waveguide.

microwave network analyzer capable of operating up to 26.5 *GHz*, as well as a full size anechoic chamber. For ease of manufacturing and measurement, we built a prototype at x-band (10 *GHz*).

The swept frequency reflection and transmission measurements were carried out on a Hewlett-Packard automated microwave network analyzer. The reflection is shown in Fig.5.2a. In Fig.5.2b, the transmission coefficient of the array (lower trace) is compared with that of the same length of *IDG* without dipole (upper trace). It can be seen that, at midband, the difference between the two traces is at least 10 *dB*. The measured patterns for the main polarization is shown in Fig.5.3 (upper trace). For a $9\lambda_0$ long array, a half power beamwidth of about 7^0 is achieved, which compares very favorable with the performance of a slotted waveguide antenna of the same length. The highest sidelobe level of (–12.7 *dB*) is close to the theoretical value of –13.5 *dB* for an in-phase array of uniform amplitude.

The lower trace in Fig.5.3 shows the cross-polarization. It can be seen that cross-polarization component is at least 23 *dB* lower than main lobe level.

For any open structure, the discontinuity occurring at the junction of the close guide (launcher) and the open guide (under test) excites higher order modes and causes reflection into the close guide and radiation into the space. Radiation from the launcher usually affects the pattern seriously. However, in this case, the discontinuity is relatively weak, and the effect of the launcher on the pattern is relatively small, as can be seen from the difference between *LHS* and *RHS* radiation pattern. This is because the field distribution of the fundamental mode in *IDG* is similar to that in rectangular waveguide.

This experiment showed that the metal strip *IDG* antenna offers promise as a low-cost, high quality microwave, millimeter wave antenna with good match and pure polarization properties.

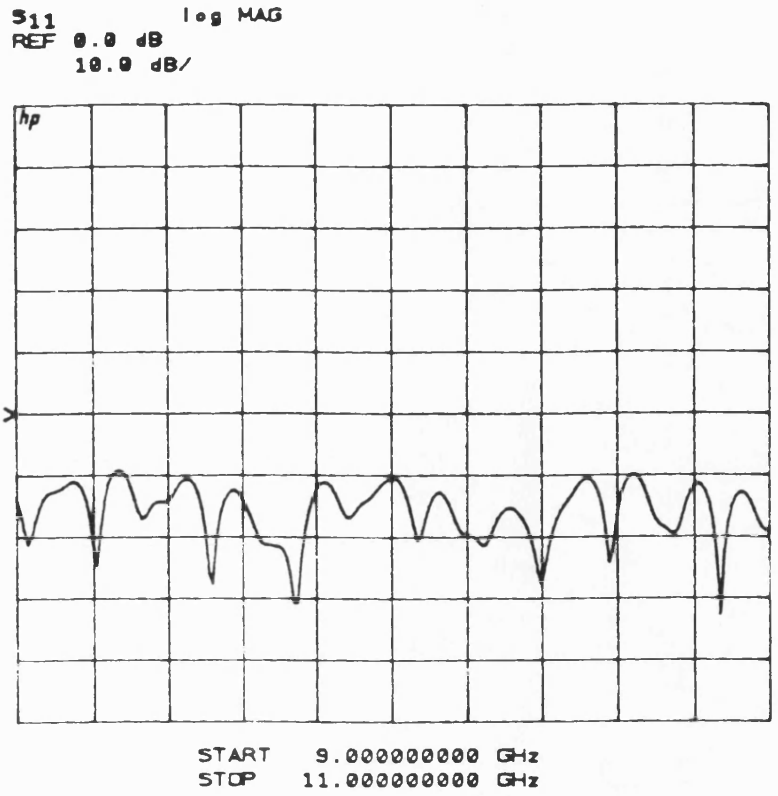

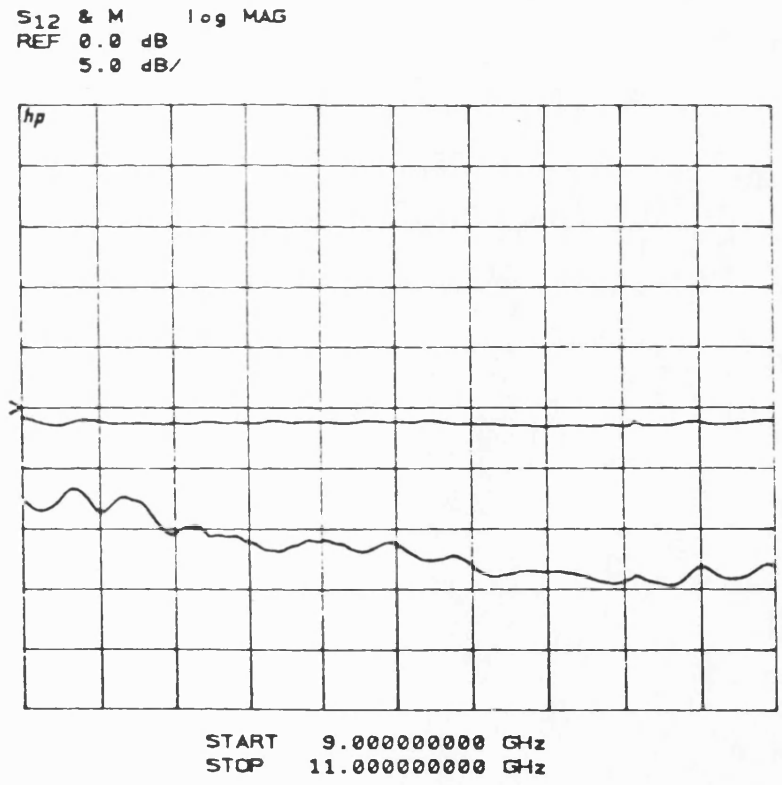

Figure 5.2 Reflection and tranmission coefficient of a 12-element uniform array.

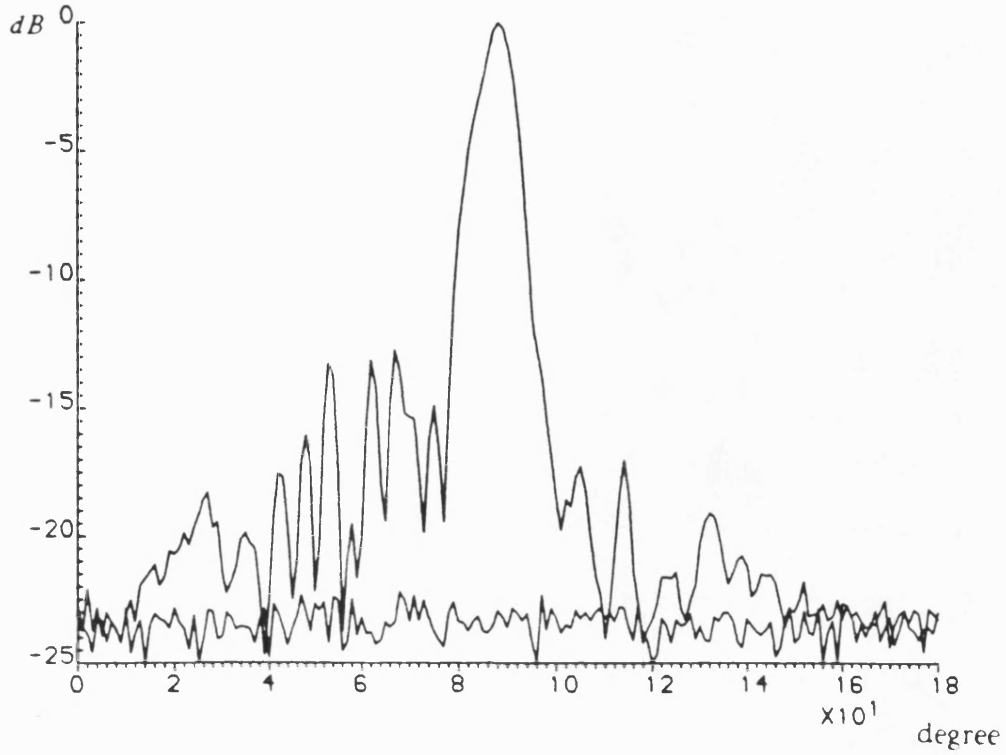

Figure 5.3 Far field pattern of a 12-element uniform array with the cross polarisation pattern.

5.3 Equivalent Network of a Thin Transverse Dipole

After this successful feasibility study, we were motivated to derive the equivalent network of the discontinuity introduced by the dipole so as to realize a rigorously designed aperture distribution of a linear array. We will describe the discontinuity by a lumped element on an equivalent transmission line circuit which gives rise to a reflected and a transmitted wave of amplitudes Γ and T respectively. Since for a monomode propagating waveguide we are only interested on the effect produced on the surface mode, the detailed nature of the diffraction field around the discontinuity is not required at this stage.

Fig.5.4a illustrates a metal strip of length l and centered at x=0. The strip is assumed to be perfectly conducting and of negligible thickness in the y and z directions. The solution to this problem will be formulated in terms of a variational expression involving the current on the strip. Since the strip is thin, and for a TE^y polarized monomode propagating guide H_x is negligible, the current is directed along the x axis only. The scattered field in the guide may be evaluated in terms of the currents on the strip by using the Green function given in Chapter 4. The scattered field is thus given by

$$E_x^s(x) = j\omega\mu_0 \int_{-l/2}^{l/2} dx' \left(1 + \frac{1}{k_0^2}\frac{\partial^2}{\partial x^2}\right) G(x,x') J(x') \tag{5.1}$$

From the distribution of E_x, we know that the second derivative of G is negligible, if the strip is not very long. The total field E_x in the guide is the sum of the incident and scattered field and must vanish on the perfectly conducting strip. The resulting integral equation for the current distribution $J(x)$ is therefore:

$$E_x^i + E_x^s = \psi_s(x, 0)$$
$$+ j\omega\mu_0 \int_{-l/2}^{l/2} dx' G(x, x') J(x') = 0 \quad \text{on strip} \tag{5.2}$$

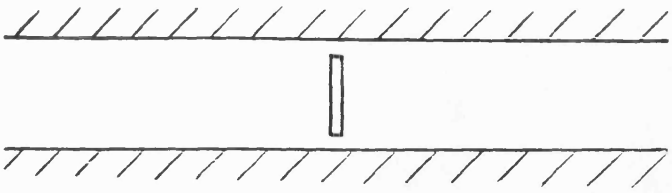

(a)

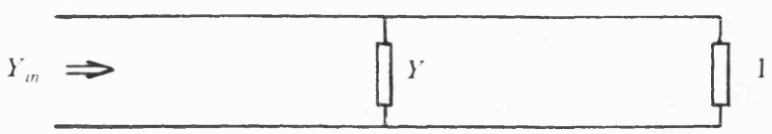

(b)

Figure 5.4 A thin strip on the top of *IDG* and its equivalent circuit.

For a monomode guide at $y = y' = 0$ (air-dielectric interface) and for $z = z' = 0$, (thin dipole), the following simplified form is valid

$$G(x,x') = j\omega\mu_0 \left(\frac{1}{2j\beta_s}\psi_s(x,0)\,\psi_s(x',0) + \int_0^\infty dk_x \int_0^\infty dk_y \frac{1}{2j\beta}\,\psi(x,0)\,\psi(x',0)\right) \tag{5.3}$$

where $\psi_s(x,y)$ denotes the normalized distribution of the discrete *IDG* mode with propagation constant β_s, $\psi(x,y)$ that of a continuous component with wave numbers k_x, k_y in the x, y direction respectively.

The reflected dominant mode is given by

$$\frac{\omega\mu_0}{2\beta_s}\,\psi_s(x,0)\int_{-l/2}^{l/2} dx'\psi_s(x',0)\,J(x') = \Gamma\,\psi_s(x,0) \tag{5.4}$$

Substituting the Green function and (5.4) into (5.2) we obtain:

$$(1+\Gamma)\psi_s(x,0) = -j\omega\mu_0 \int_0^\infty dk_x \int_0^\infty dk_y \frac{1}{2j\beta}\psi(x,0)\int_{-l/2}^{l/2} dx'\psi(x',0)\,J(x') \tag{5.5}$$

Multiplying both sides of (5.5) by $J(x)$, integrating over strip and dividing both sides by $\left(\int_{-l/2}^{l/2} dx\,\psi_s(x,0)\,J(x)\right)^2$ we get

$$\frac{1+\Gamma}{\int_{-l/2}^{l/2} dx\,\psi_s(x,0)\,J(x)} = -j\omega\mu_0 \frac{\int_0^\infty dk_x \int_0^\infty dk_y \frac{1}{2j\beta}\left(\int_{-l/2}^{l/2} dx\,\psi(x,0)\,J(x)\right)^2}{\left(\int_{-l/2}^{l/2} dx\,\psi_s(x,0)\,J(x)\right)^2} \tag{5.6}$$

Rewriting (5.4) as $\int_{-l/2}^{l/2} dx\,\psi_s(x,0)\,J(x) = \Gamma\frac{2\beta_s}{\omega\mu_0}$ and substituting into (5.6) yields

$$Z = \frac{1+\Gamma}{-2\Gamma} = j\beta_s \frac{\int_0^\infty dk_x \int_0^\infty dk_y \frac{1}{2j\beta}\left(\int_{-l/2}^{l/2} dx\,\psi(x,0)\,J(x)\right)^2}{\left(\int_{-l/2}^{l/2} dx\,\psi_s(x,0)\,J(x)\right)^2} \tag{5.7}$$

This expression of the shunt impedance Z is readily shown to be stationary.

At the edge of an infinitely thin perfectly conducting strip ($x = \pm l/2$), the tangential magnetic field (H_z) and hence the normal current density (J_x) vanishes as $r^{1/2}$, where r is the radial distance from the edges $x = \pm l/2$. Hence we may set:

$$J(x) = J_0 \sqrt{1-(2x/l)^2}$$

This single term, in fact, is sufficient unless the strip end comes close to the 90^0 metal corner of the guide or other strong interaction effects are present.

For the sake of convenience, we set

$$U = \int_{-l/2}^{l/2} dx\, \psi(x, 0)\, J(x)$$

$$U_s = \int_{-l/2}^{l/2} dx\, \psi_s(x, 0)\, J(x)$$

Then (5.7) becomes

$$Z = j\,\beta_s \frac{\int_0^\infty dk_x \int_0^\infty dk_y \frac{1}{2j\beta} U^2}{U_s^2}$$

By going over to cylindrical coordinates

$$Z = \beta_s \frac{\int_0^{\pi/2} d\theta \int_0^\infty dk_t \frac{k_t}{2\beta} U^2}{U_s^2}$$

It is noted that for $k_t < k_0$, β is real, corresponding to the propagating continuous modes. This contribution gives rise to radiation and is represented by the real part of Z. For $k_t > k_0$, β is pure imaginary, corresponding to non-propagating continuous modes. Their contribution is purely reactive, i.e. power storage (mainly inductive) in the neighborhood of the strip, and is represented by the imaginary part of Z.

Introducing the additional change of variable

$$k_t = k_0 \sin\eta\,; \quad \beta = k_0 \cos\eta$$

the two contributions are conveniently separated out as

$$R = \frac{\beta_s}{2} k_0 \frac{\int_0^{\pi/2} d\theta \int_0^{\pi/2} d\eta \sin\eta\, U^2(\theta,\eta)}{U_s^2} \tag{5.8a}$$

$$X = \frac{\beta_s}{2} K_0 \frac{\int_0^{\pi/2} d\theta \int_{\pi/2}^{\pi/2+j\infty} d\eta \sin\eta\, U^2(\theta,\eta)}{U_s^2} \tag{5.8b}$$

the two regions on k_t-plane and the route of the integral over η are shown in Fig.5.5.

Using the expression for ψ and ψ_s in (4.65) and (4.41), integrating by parts and canceling the common factor of U and U_s, we recover:

$$U = \int_{-l/2}^{l/2} dx\, \psi(x,0) J(x) = -\sin\alpha \frac{J_1(\frac{k_x l}{2})}{k_x}$$

$$= -\sin\alpha \frac{J_1(\frac{k_0 l}{2}\cos\theta\sin\eta)}{k_0 \cos\theta \sin\eta}$$

and

$$U_s = \int_{-l/2}^{l/2} dx\, \psi_s(x,0) J(x) = -\sum_n E_{xn}\delta_n \frac{1}{n\pi} J_1(\frac{n\pi l}{2})$$

The angular integrals (5.8) are easy to evaluate numerically. The value of the dipole resistance R and reactance X, normalized to the characteristic impedance of the fundamental *IDG* mode $Z_0 \approx \frac{\omega\mu_0}{\beta_s}$, are given in Fig.5.6 vs. the normalized dipole length l/a, for different values of frequency.

It is noted that R/Z_0 is fairly insensitive to dipole length. X/Z_0 decreases with l/a, as

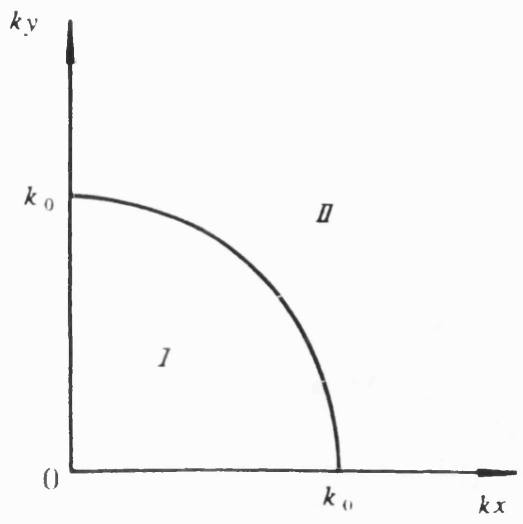

(a). Two regions corresponding to propagating and non-propagating continuous modes.

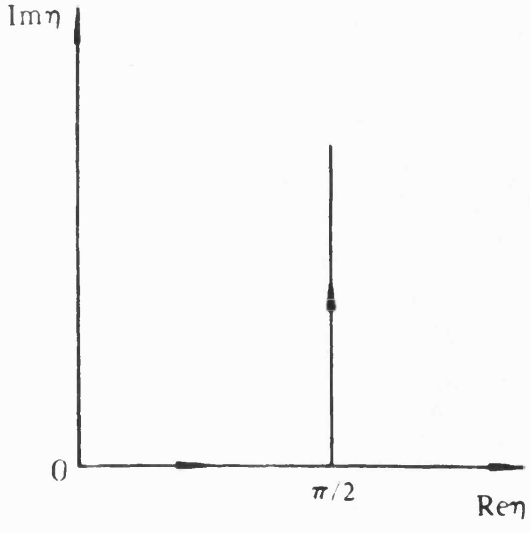

(b). Path of integration for the continuous modes.

Figure 5.5

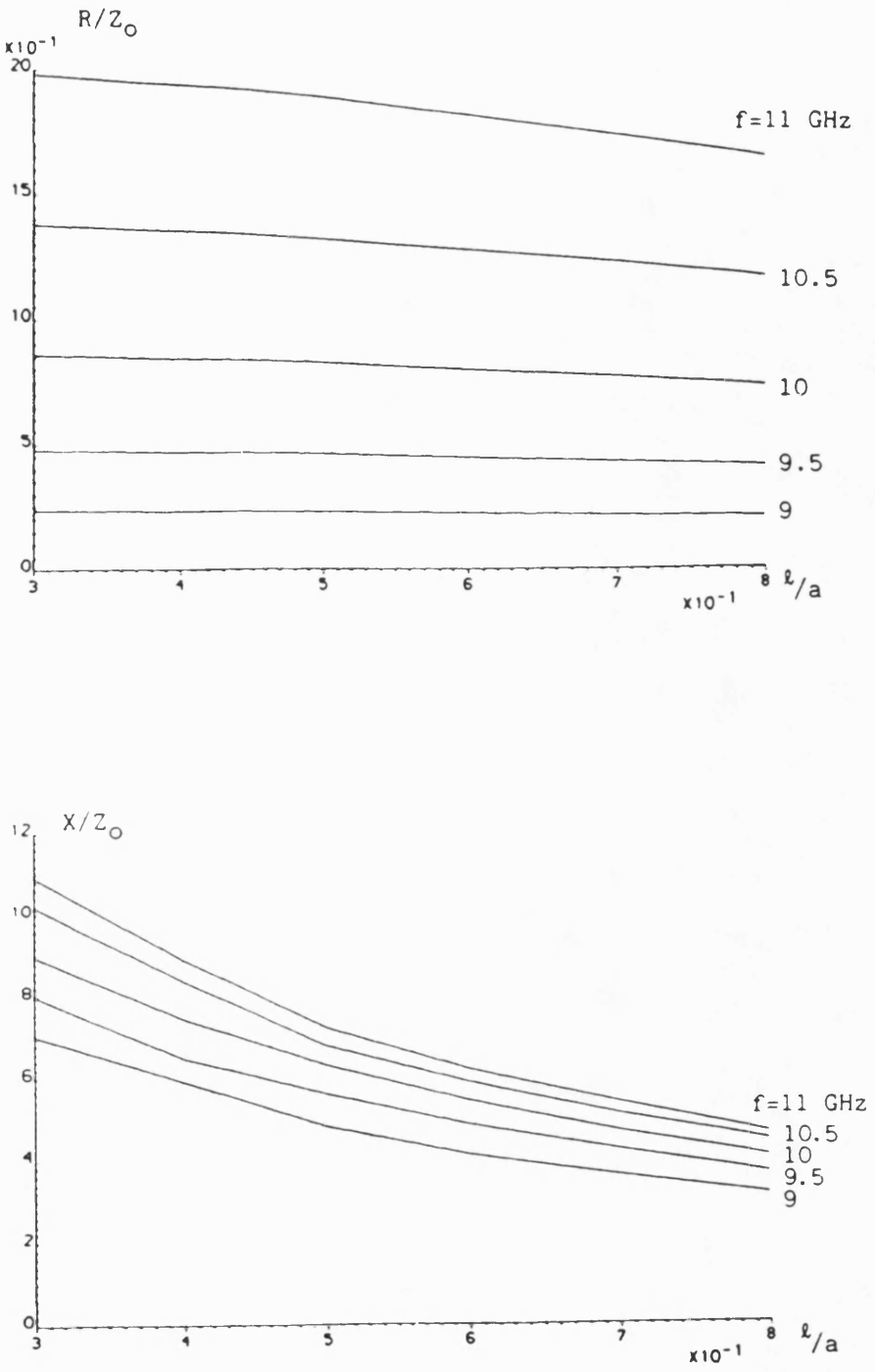

Figure 5.6 Normalised resistance and reactance of a single transverse dipole on *IDG*

it should, since the shunt discontinuity increases with dipole length.

5.4 Array Design

The above theory can be applied to the design of a one-dimensional array of dipoles in order to realize a leaky-wave antenna, as shown in Fig.5.1.

The phase shift associated with the shunt reactance, however, must be corrected for. The circuit between reference planes $A-A'$ in Fig.5.7 represents a pair of dipoles separated by a line length θ_1.

The reflection coefficient Γ_p of the pair is given by

$$\Gamma_p \approx \Gamma(1 + T^2 e^{-2j\theta_1}) \tag{5.9}$$

where Γ, T are the reflection, transmission coefficient of a single strip:

$$\Gamma = \frac{-Y}{2+Y};\ T = \frac{2}{2+Y}; \qquad Y = 1/Z = G - jB;\ (B>0)$$

Perfect matching cannot actually be achieved by just varying θ_1 due to the presence of losses. A minimum of $|\Gamma_p|$, however, is achieved when θ_1 is chosen so that

$$\theta_1 = \frac{1}{2}\tan^{-1}\frac{2B\,(G+2)}{4G+4-B^2} \tag{5.10}$$

The value of θ_1 in degrees as a function of l/a is given in Fig.5.8.

When (5.10) is satisfied, the residual reflection of the pair, $|\Gamma_p|$ is less than 7.10^{-3} for $l/a < 0.8$ over the band.

Moreover, the radiation loss of the pair, which is an important parameter in the array design, is given by

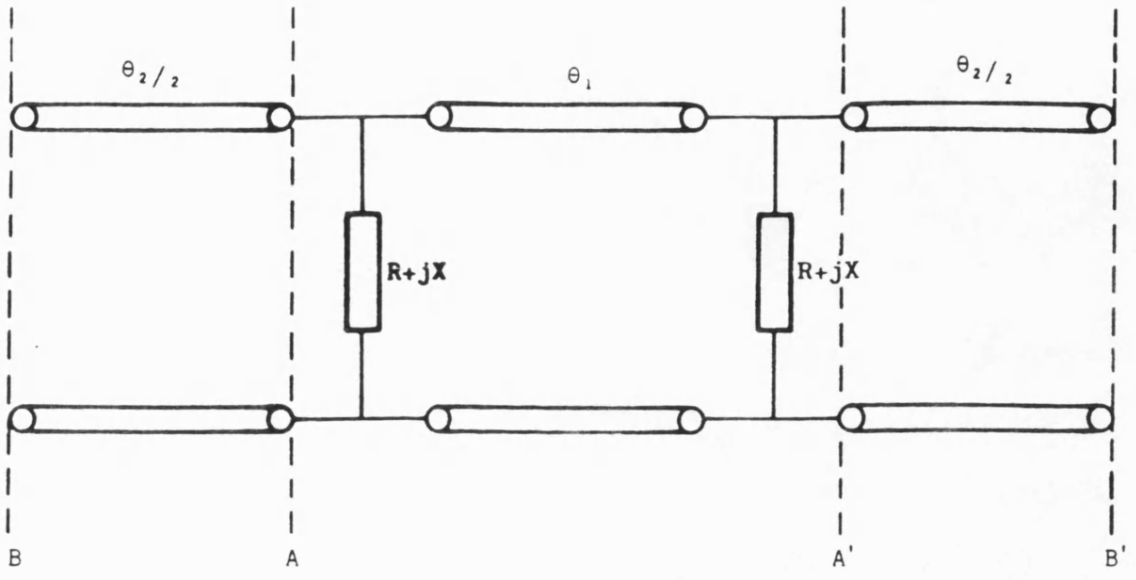

Figure 5.7 Equivalent network of a pair of dipoles.

$$L_{rad} = 1 - |\Gamma_p|^2 - |T_p|^2 \approx 1 - |T_p|^2 \qquad (5.11)$$

where Γ_p is defined in (5.9) and

$$T_p = T^2 \, e^{-j\theta_1}$$

$|T_p|$ vs. l/a is given in Fig.5.9.

Constructive interference (array effect) is obtained by spacing each pair a guided wavelength apart (nominally). This is in accordance with well known design principles in the literature.

The actual spacing θ_2 between two successive pair has to be corrected for the phase shift associated to Γ_p. The circuit between reference planes B and B' of Fig.(5.7) represents a pair of dipoles between two lengths of transmission line $\theta_2/2$. In order for the array effect to take place, the spacing θ_2 must be such that

$$\theta_2 = 2\pi - \theta_1 - 2arg\, T \qquad (5.12)$$

The resulting value θ_2 are plotted in Fig.5.10 associated with l/a.

5.5 Design Example, Experimental Verification

In order to demonstrate the application of the above theory, we designed a 23-element array, based on a Taylor distribution, to operate at $f_0 = 10\,GHz$. The design goal was to obtain a 4^0-wide main lobe at the $3\,dB$ points with sidelobes lower than $-20\,dB$. The guide dimension were $a = 10.16\,mm$, $h = 15.24\,mm$. The dielectric used was teflon (ε_r=2.08), which is easy to machine, although use of a denser dielectric may be profitable with a view to reducing the antennas' width and depth.

As discussed in Chapter 2, in order to synthesize such a far field pattern, the radiation loss distribution of the array elements, each being a pair of dipoles as described

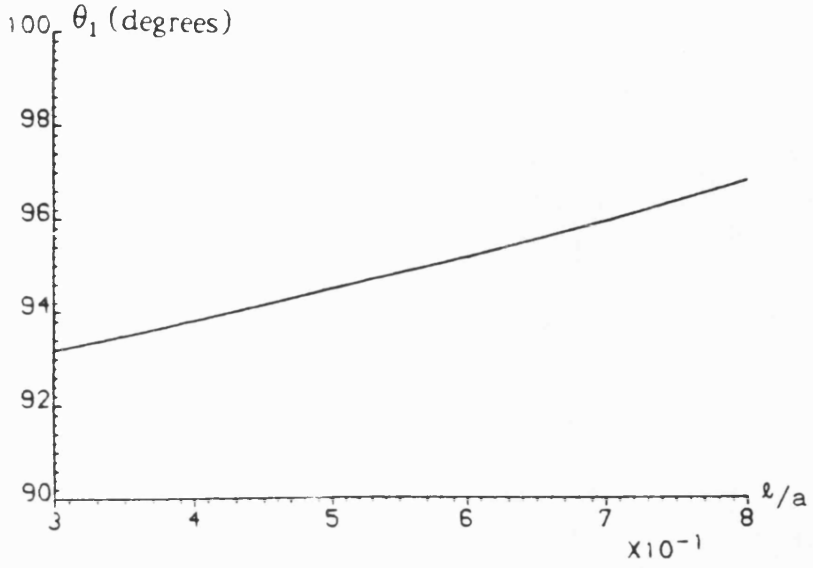

Figure 5.8 Plot of θ_1 vs. l/a

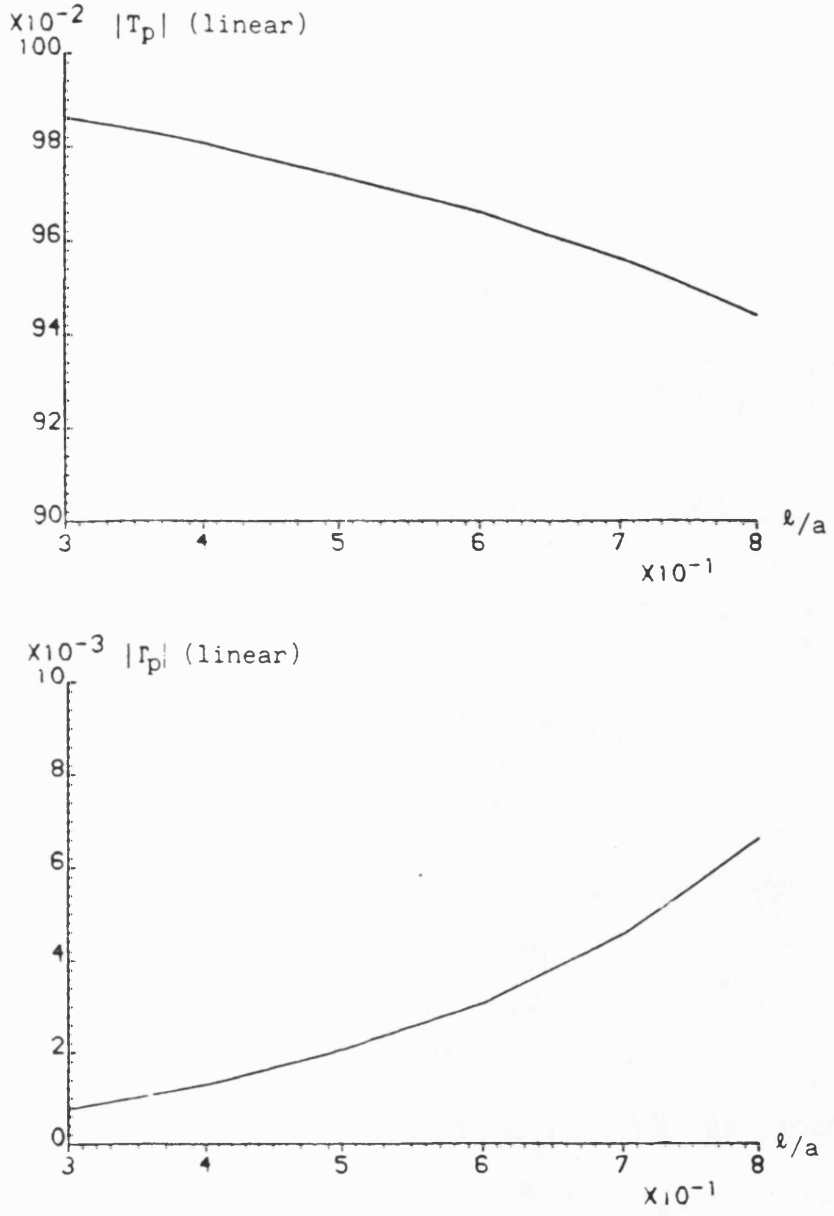

Figure 5.9 Plots of T and Γ vs. l/a

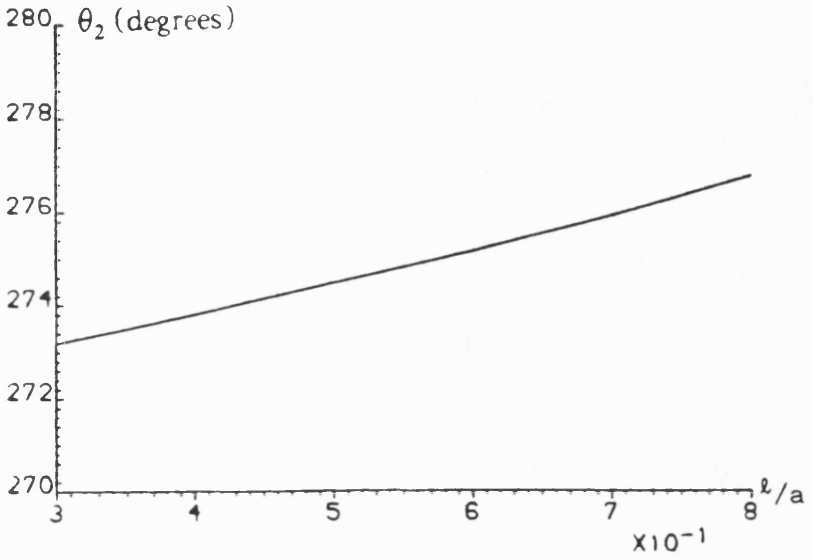

Figure 5.10 Plot of θ_2 vs. l/a

in the previous section, is as given in table 5.1.

We kept all the strip widths as $2mm$, whilst the lengths l/a were chosen according to Fig.5.9, so as to realize the above distribution. The resulting dipole lengths are also given in table 5.1.

For each dipole length, using Fig.5.8 we can derive the electrical distance between the two identical dipoles of the same pair. This can be converted to physical distances using the fact that $\lambda_{g0} = 23.66mm$. Also, using Fig.5.10, the distances between successive pair can be found (see table 5.1).

Without precision fabrication facilities, it was difficult to realize the spacings accurately. The overall array length, however, could be accurately controlled and small deviations were expected to compensate each other. The overall length of the array was $500mm$. The antenna was terminated with a piece of absorbing material. Excitation takes place at one end from a waveguide transition, as shown in detail in Fig.5.1. The resulting array was built and its photograph is shown in Fig.1.2.

The scattering parameters were tested on the network analyzer. The antenna features, as predicted, good broadband match and radiation efficiency, as shown in Fig.5.11.

The radiation pattern, measured in a test range, is plotted in Fig.5.13 and the test diagram is shown in Fig.5.12. The main lobe is indeed less than 4^0-wide at the $-3dB$ points, and the sidelobes less than $-21dB$ overall. Finally, in Fig.5.14 the radiation pattern in the orthogonal plane (x-y) is also shown, for the completeness sake, and compared with the computed characteristics of a single dipole given in Chapter 4.

In this chapter we have derived the equivalent network of thin radiating transverse dipoles in *LSE*-polarized Inset Dielectric Guide. The information is presented in a form

easy to use in synthesis and its application to the design of a 23-element linear array is demonstrated. The array was built and tested, showing excellent performance in agreement with the theoretical prediction. It is felt that *IDG* antennas show good promise for high-performance, low-cost millimetric applications.

Array Parameters						
N	L_{rad}	l/a	θ_1	θ_2	R/Z_0	X/Z_0
1	0.020	0.23	92.8	272.8	0.860	10.0
2	0.020	0.23	92.8	272.8	0.860	10.0
3	0.021	0.24	92.8	272.8	0.855	9.9
4	0.023	0.26	92.9	272.9	0.850	9.6
5	0.026	0.29	93.1	273.1	0.850	9.0
6	0.033	0.35	93.5	273.5	0.837	8.1
7	0.042	0.43	94.0	274.0	0.825	7.0
8	0.053	0.51	94.5	274.6	0.807	6.1
9	0.064	0.58	95.0	275.0	0.790	5.6
10	0.074	0.64	95.5	275.4	0.775	5.1
11	0.083	0.69	95.8	275.8	0.760	4.6
12	0.092	0.73	96.2	276.2	0.745	4.4
13	0.101	0.76	96.5	276.5	0.732	4.2
14	0.108	0.80	96.8	276.8	0.718	4.0
15	0.112	0.81	96.9	276.9	0.710	3.9
16	0.112	0.81	96.9	276.9	0.710	3.9
17	0.104	0.78	96.6	276.6	0.725	4.1
18	0.094	0.74	96.3	276.3	0.740	4.4
19	0.087	0.70	95.9	275.9	0.755	4.6
20	0.084	0.69	95.8	275.8	0.759	4.6
21	0.086	0.70	95.9	275.9	0.755	4.6
22	0.094	0.74	96.3	276.3	0.740	4.4
23	0.104	0.78	96.6	276.6	0.725	4.1

Table 5.1

Parameters for a 23 Element Taylor Array

Number of equal level sidelobes $\bar{n} = 4$

sidelobe level $SL = -20\ dB$

power approaching to the load $P_0 = 17\%$

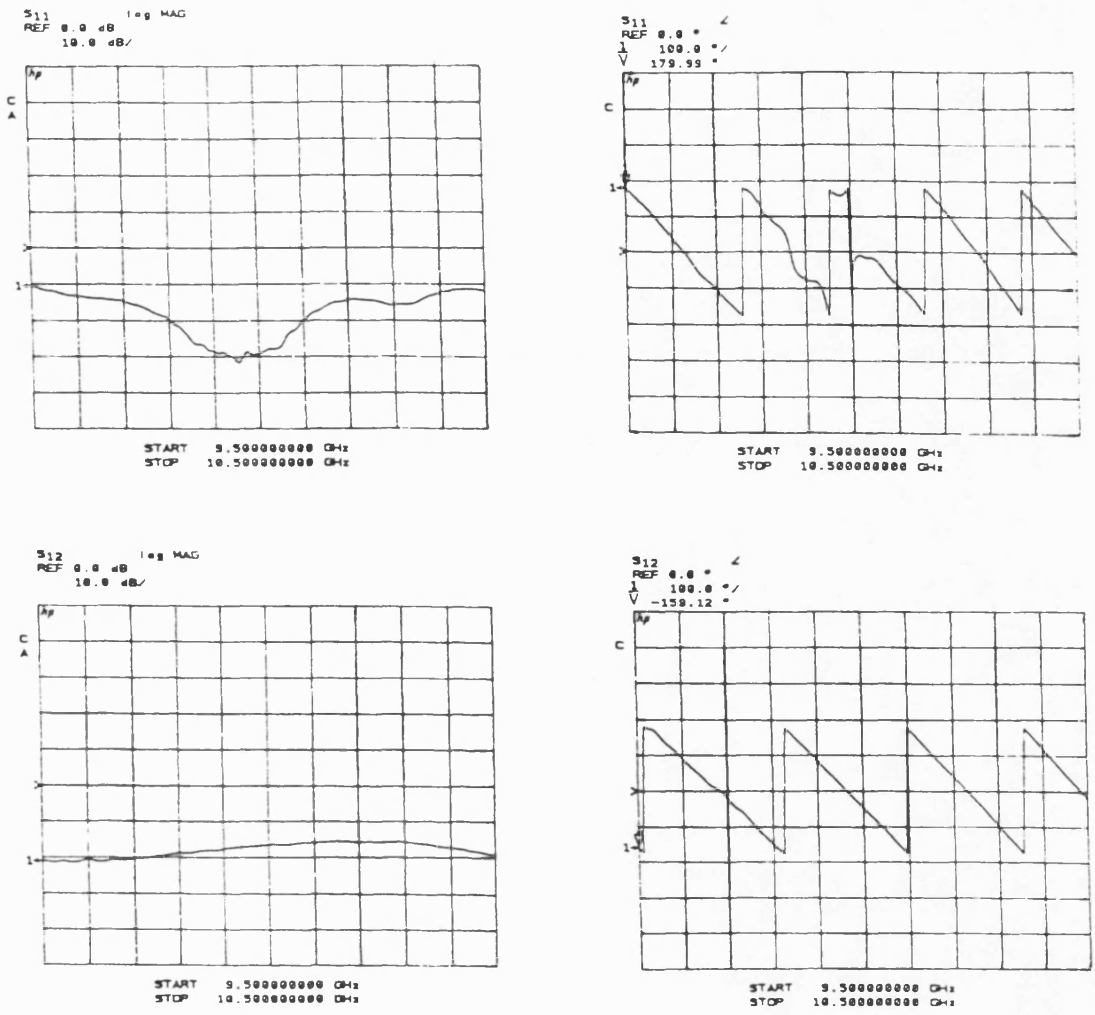

Figure 5.11 Reflection and transmission coefficient of a 23-element Taylor array.

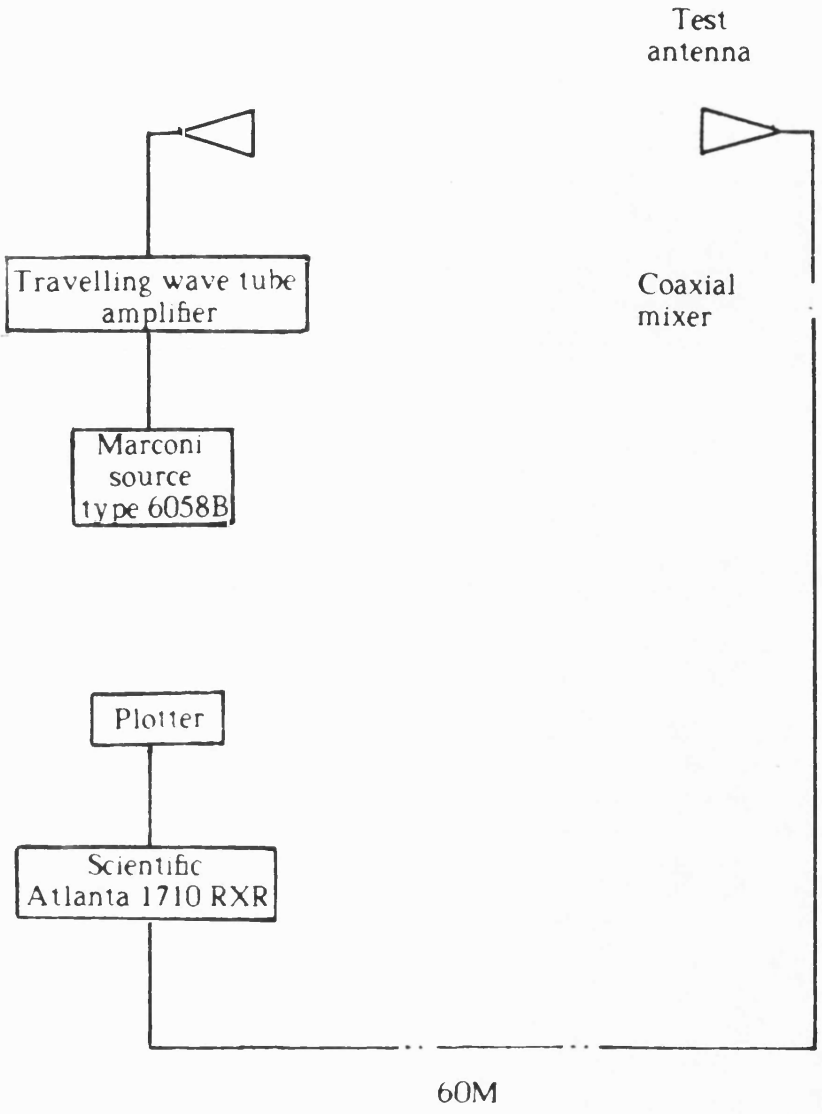

Figure 5.12 Far field pattern test diagram.

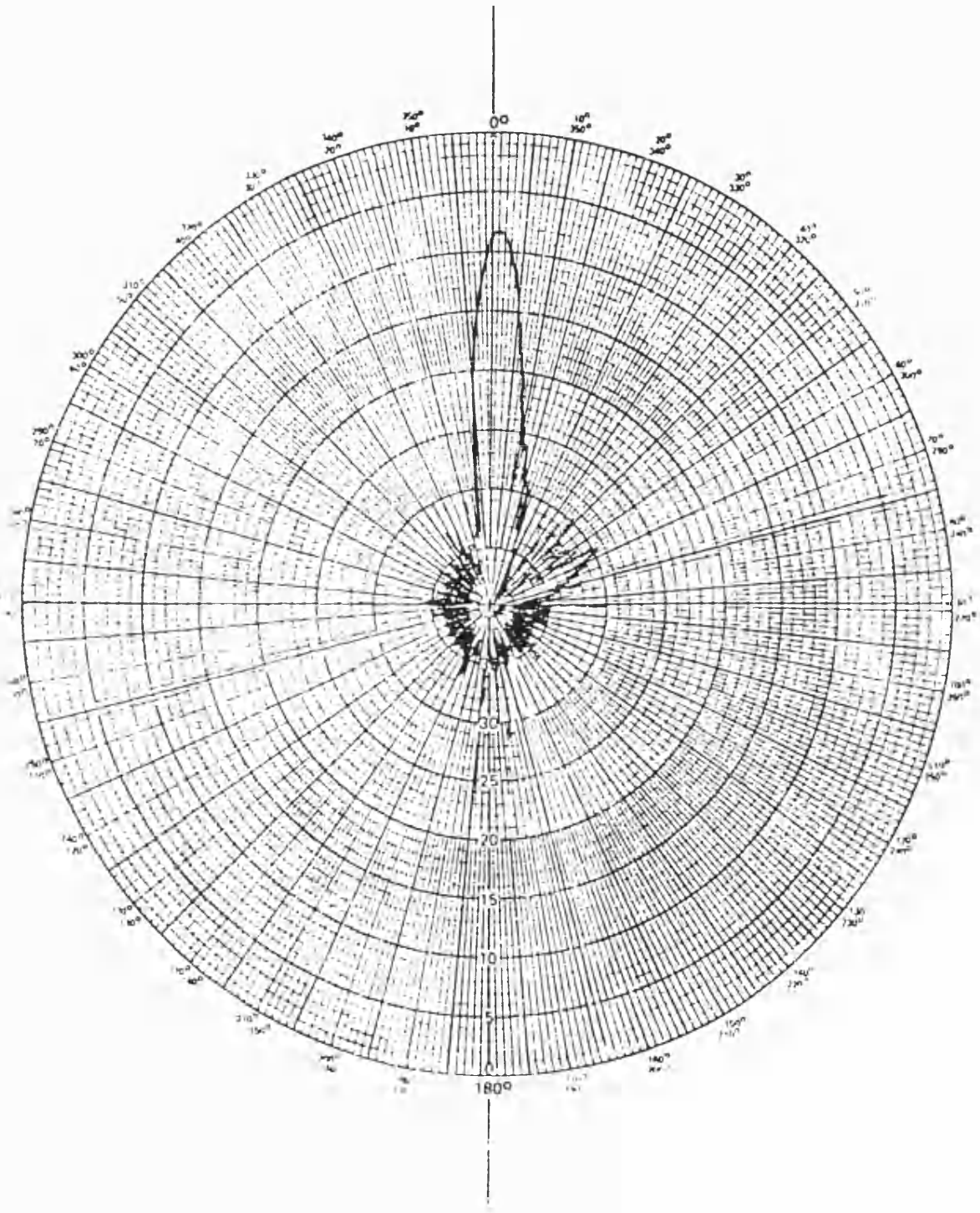

Figure 5.13 Far field pattern of a 23-element Taylor array. (yz-plane)

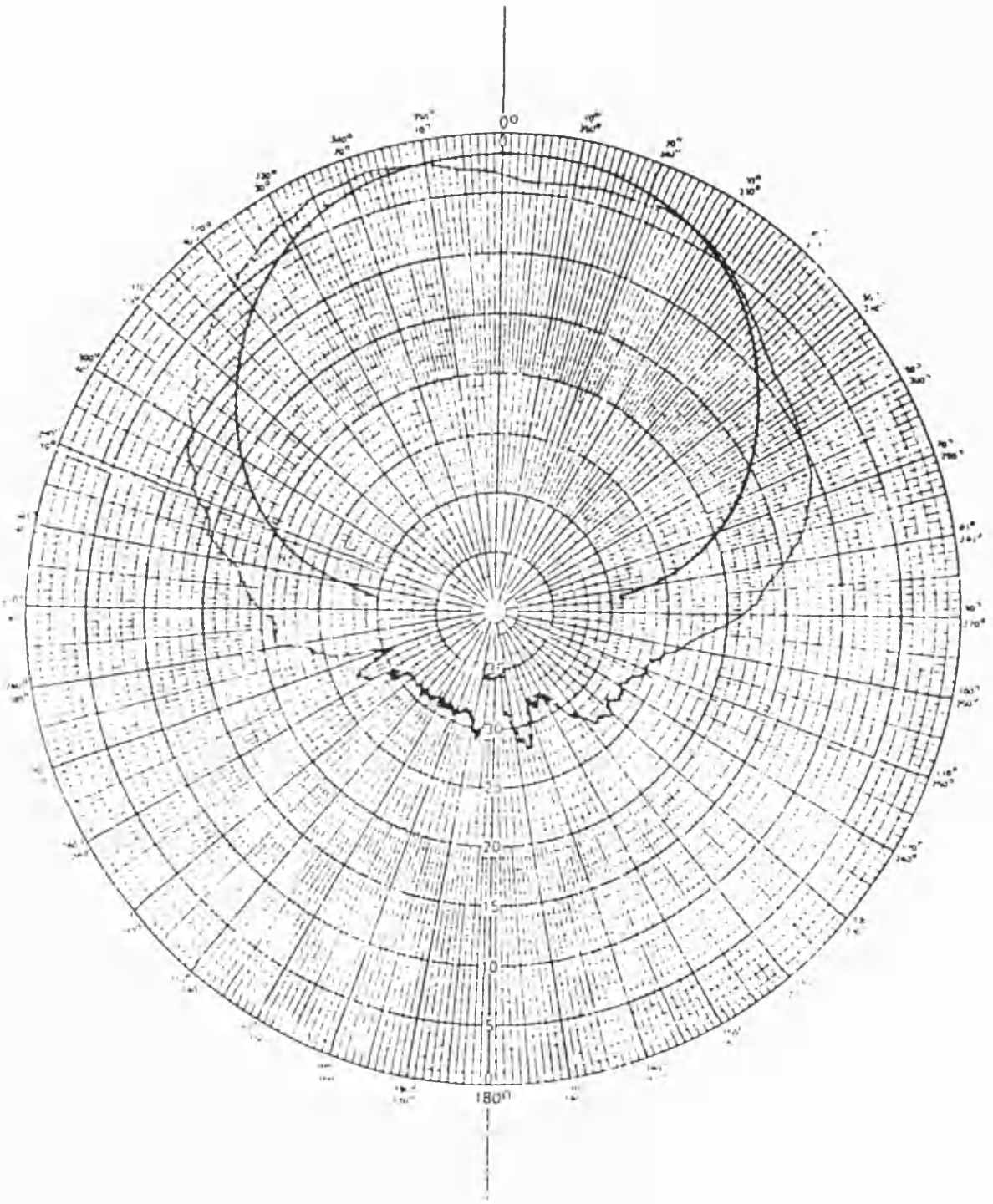

Figure 5.14 Far field pattern of a 23-element Taylor array (xy-plane) compared with the computed pattern of a single dipole.

REFERENCES

[1] R. M. Knox, "Dielectric waveguide integrated circuits - An overview", *IEEE Trans. Microwave Theory and Tech., vol. MTT*-24, pp.806-814, Nov. 1976.

[2] T. Itoh, "Application of gratings in dielectric waveguide for leaky wave antennas and band-reject filters", *IEEE Trans. Microwave Theory and Tech., vol. MTT*-25, pp.1134-1138, Dec. 1977.

[3] R. Mittra, R.Kastner, "A spectral domain approach for computing the radiation characteristics of a leaky wave antenna for millimeter waves", *IEEE Trans. Antenna and Propag. vol. AP*- 23, pp.652-654, July, 1981.

[4] A. A. Oliner and M. Guglielmi, "A practical theory for dielectric image guide leaky wave antennas loaded by periodic metal strips", Proc. 17th European Microwave Conf., Rome, Sept. 7-11 1987, pp. 549,554.

[5] K. Solbach, "E-band leaky wave antenna using dielectric image line with etched radiating elements", 1979, *IEEE MTT–S* Intern. Microwave Symp. Digest, pp.214-216.

[6] T. Rozzi and L. Ma, "Scattering by dipoles in I.D.G. and application to millimetric leaky wave antennas" Proc. 17th European Microwave Conf., Rome, Sept. 7-11 1987, pp.543-548.

CHAPTER 6

LSM CASE OF IDG, MODE COMPLETENESS, NORMALIZATION AND GREEN'S FUNCTION.

6.1 An Analysis of the Dispersion Characteristics

6.1.1 Expression of Field Components

There are two useful manners of single mode operation for *IDG*. The first one, as has been discussed, is to operate in the H_{01} mode in relatively deep slots. The field distribution in this mode is very similar to that in one half of a conventional rectangular waveguide, operating in its lowest H_{10} mode. The second manner of single mode operation is in the E_{11} mode in shallow, broad slots ($a>h$). In this mode the field distribution is similar to that of an image guide and the *LSM* approximation is suitable. In the *LSM* approximation, there is no H-component perpendicular to the dielectric interface. The fields can be described by means of a y-oriented electric Hertzian potential:

$$\Pi_e = \mathbf{y}\, \psi_e\, e^{-j\beta z} \tag{6.1}$$

where **y** is the unit vector in the y-direction. From (6.1), the fields are given by

$$\mathbf{E} = \nabla\,\nabla\cdot\,\Pi_e + \varepsilon_r k_0^2\,\Pi_e \tag{6.2a}$$

$$\mathbf{H} = j\,\omega\,\varepsilon_0\varepsilon_r \nabla\times\Pi_e \tag{6.2b}$$

or, componentwise, omitting the propagation factor $e^{-j\beta z}$

$$E_x = \partial_x\partial_y\psi_e \tag{6.3a}$$

$$E_y = (\partial_y^2 + \varepsilon_r k_0^2)\,\psi_e \tag{6.3b}$$

$$E_z = -j\beta\,\partial_y\psi_e \tag{6.3c}$$

$$H_x = -\omega\varepsilon_0\varepsilon_r\beta\,\psi_e \tag{6.3d}$$

$$H_y = 0 \tag{6.3e}$$

$$H_z = j\omega\varepsilon_0\varepsilon_r\partial_x\,\psi_e \tag{6.3f}$$

The x-dependence of ψ_e in the slot is chosen as

$$\phi_n(x) = 2\cos n\pi x \qquad n=1,3,5,... \tag{6.4}$$

so as to give the normalization

$$\int_0^{1/2} \phi_n(x)\,\phi_m(x) = 1$$

In order to get a convergent dispersion equation, we choose E_x as the main field component and derive all else from it. Let us consider the slot region first. If we set

$$E_x = \sum_{n=1,3,...} E_{xn}\,2\sin n\pi x\,\frac{\sin q_n(y+h)}{\sin q_n h} \tag{6.5}$$

i.e.

$$\psi_e(x,y) = \sum_{n=1,3,...} f(n)\,\phi_n(x)\frac{\cos q_n(y+h)}{\sin q_n h} \tag{6.6}$$

then according to (6.3) the H_z component is given by

$$H_z = j\omega\varepsilon_0\varepsilon_r\partial_x\psi_e$$

$$= -j\omega\varepsilon_0\varepsilon_r \sum_{n=1,3,...} E_{xn}2\sin n\pi x\,\frac{1}{q_n}\frac{\cos q_n(y+h)}{\sin q_n h} \tag{6.7}$$

For each slot component n, we define an input admittance of the slot as seen from the interface as follows:

$$Y_n = \frac{H_z}{E_x} = \frac{-j\omega\varepsilon_0\varepsilon_r}{q_n} cot\ q_n h \tag{6.8}$$

Under normal operating conditions, $q_1^2 > 0$, whereas $q_{3,5,...}^2 < 0$. Hence, for $n > 1$,

$$Y_n = \frac{j\omega\varepsilon_0\varepsilon_r}{|q_n|} \coth |q_n|\ h$$

For the air region, we define the x-dependence of ψ_e analogously to (6.4), with a continuous expression in terms of the wavenumber k_x:

$$\phi(x,k_x) = \sqrt{2/\pi}\ \cos k_x x \tag{6.9}$$

The field components are then given by:

$$E_x\ (x,y) = \int_0^\infty e_x(k_x)\ \sqrt{2/\pi}\ \sin k_x x\ e^{-jk_y y}\ dk_x \tag{6.10}$$

$$H_z\ (x,y) = j\omega\varepsilon_0 \int_0^\infty e_x(k_x)\sqrt{2/\pi}\ \sin k_x x\ \frac{1}{-jk_y} e^{-jk_y y}\ dk_x \tag{6.11}$$

For each component k_x, an admittance is defined as:

$$Y(k_x) = -\frac{H_z}{E_x} = \frac{\omega\varepsilon_0}{k_y(k_x)} \tag{6.12}$$

Hence, for a bound mode, $k_0 < \beta_s < \sqrt{\varepsilon_r}\, k_0$,

$$k_y^2(k_x) = k_0^2 - \beta_s^2 - k_x^2 < 0$$

$$k_y(k_x) = -j\sqrt{\beta_s^2 - k_x^2 - k_0^2}$$

$$Y(k_x) = j\frac{\omega\varepsilon_0}{|k_y(k_x)|}$$

The signs in (6.8) and (6.12) are consistent with positive power flow into each region from the interface.

6.1.2 Resonant Condition

At each side of the interface $y = 0$, the transverse field components may be linked by an admittance operator

$$H_z(x, 0) = \hat{Y}^s E_x(x',0) \tag{6.13}$$

$$-H_z(x, 0) = \hat{Y}^a E_x(x',0) \tag{6.14}$$

where the integral operators $\hat{Y}^s$, $\hat{Y}^a$, are defined such that

$$H_z(x, 0) = \hat{Y}^s E_x(x',0)$$

$$\equiv \int_0^{1/2} Y^s(x,x'; y=y'=0)\, E_x(x',0)\, dx' \tag{6.15}$$

The quantity Y^s denotes the kernel of the integral operator $\hat{Y}^s$ and similarly for Y^a.

Due to the continuity of the tangential components across the interface, (6.13) and (6.14) can be added to give

$$(\hat{Y}^s+\hat{Y}^a)\, E_x(x, 0) = 0$$

$$\int_0^{1/2} dx'(Y^s(x,x'; y=y'=0) + Y^a(x,x'; y=y'=0))\, E_x(x',0) = 0 \tag{6.16}$$

The explicit form of the admittance operators can be derived as follows. At $y=0^-$, from (6.5)

$$E_x(x, 0) = \sum_{n=1,3,\ldots} E_{xn}\, 2 \sin n\pi x$$

hence

$$E_{xn} = \int_0^{1/2} E_x(x, 0) 2 \sin n\pi x\ dx \tag{6.17}$$

Substituting (6.8) and (6.17) into (6.7) gives

$$H_z(x,0) = \int_0^{1/2} \sum_{n=1,3,\ldots} Y_n \, 2\sin n\pi x \; 2\sin n\pi x \; E_x(x',0)\, dx' \tag{6.18}$$

Comparing (6.18) with (6.15) gives

$$Y^s = \sum_{n=1,3,\ldots} Y_n \, 2\sin n\pi x \; 2\sin n\pi x \tag{6.19}$$

The admittance operator for the air region is found similarly.

$$Y^a = \int_0^{\infty} Y(k_x)\, \sqrt{2/\pi}\, \sin k_x x \; \sqrt{2/\pi}\, \sin k_x x'\, dk_x \tag{6.20}$$

6.1.3 Ritz-Galerkin Formulation

The integral equation (6.16) may be solved by the Galerkin method. In order to achieve rapid convergence, the boundary condition at the 90^0 edge $W(x) = (1-(2x)^2)^{-1/3}$ is chosen as the weight function. This choice, in turn, leads naturally to the set of Gegenbauer polynomials $C_m^{1/6}(2x)$, m=1,3,..., which are orthogonal with respect to the weight function W. The order 1/6 is such that :

$$\frac{1}{N_m N_n} \int_0^{1/2} (1-(2x)^2)^{-1/3}\, C_m^{1/6}(2x)\, C_n^{1/6}(2x) dx = \delta_{nm} \tag{6.21}$$

where N_m is the normalization factor of the m-th polynomial. We can now expand all of the quantities appearing in the integral equation (6.16) in terms of a finite number (m=1,3,...M) of the above functions, namely

$$E_x(x,0) = W \sum_{m=1,3,\ldots}^{M} X_m C_m^{1/6} \tag{6.22}$$

$$2\sin n\pi x = \sum_{m=1,3,\ldots}^{M} P_{mn} C_m^{1/6} \tag{6.23}$$

$$\sqrt{2/\pi}\, \sin k_x x = \sum_{m=1,3,\ldots}^{M} P_m(k_x) C_m^{1/6} \tag{6.24}$$

In (6.22), X_m is the unknown m-th amplitude factor. The coefficients in (6.23) and

(6.24) are given by:

$$P_{mn} = \int_0^{1/2} W\, C_m^{1/6}\, 2 \sin n\pi x \; dx \tag{6.25}$$

$$P_m(k_x) = \int_0^{\infty} W\, C_m^{1/6}\, \sqrt{2/\pi}\, \sin k_x x \; dx \tag{6.26}$$

where m and n are odd. These expressions are very similar to those for the *LSE* case.

By substituting (6.22) to (6.24) into the integral equation (6.16), we can recast the latter as standard matrix equation of order $(\frac{M+1}{2})\times(\frac{M+1}{2})$:

$$\mathbf{Y} \cdot \mathbf{X} \equiv (\mathbf{Y}^s + \mathbf{Y}^a) \cdot \mathbf{X} = 0 \tag{6.27}$$

From (6.22) to (6.24), the matrices $\mathbf{Y}^{s,a}$ corresponding to the operators $\hat{Y}^{s,a}$ are given, componentwise by :

$$(\mathbf{Y}^s)_{km} = \sum_{n=1,3,\ldots}^{\infty} Y_n P_{kn} P_{mn} \tag{6.28}$$

$$(\mathbf{Y}^a)_{km} = \int_0^{\infty} Y(k_x)\, P_k(k_x)\, P_m(k_x)\, dk_x \tag{6.29}$$

Nontrivial solutions of (6.16) are obtained by setting

$$\det \mathbf{Y}\,(\beta) = 0 \tag{6.30}$$

which is the dispersion equation for the discrete modes of the guide. At a root β_s, the corresponding null eigenvectors of **Y**, $\mathbf{X}(\beta_s)$, give the relative amplitudes of the discrete modes at $y = 0$, according to (6.22), from which all remaining components everywhere in the guide can be derived via (6.3).

6.1.4 Computed and Measured Results

Two X-band samples of *IDG* were available for measurement. The dimensions of the guide are the same as standard X-band waveguide, i.e., a=2.286 cm, h=1.016 cm,

and the relative dielectric constant of the filling material, *PTFE*, is $\varepsilon_r = 2.08$. Comparison between the measured and computed values of λ_0/λ_g is given in Fig.6.1, where three basis terms were used. The coefficients of the eigenvector, X_m, are given in Table 6.1. It can be seen that the convergence property of (6.22) is very good; two term expansion is sufficient. The field magnitude plots of E_{11} mode are given in Fig.6.2.

6.1.5 Normalization of the Discrete Modes

The amplitudes X_m of the eigenvector of (6.16) give the relative amplitudes of the basis components. To get a proper amplitude ratio between discrete and continuous modes, the mode function needs to be normalized. The normalization condition for discrete modes can be written as:

$$\int_{section}\int dxdy\, A^2\, \psi_s^2 = 1 \tag{6.31}$$

where ψ_s can be any field component, and the constant A is to be found so as to satisfy the condition (6.31). Since we are using Green's function expressed with normalized mode functions to analyze the scattered field of a longitudinal dipole, it is convenient to choose the expressions for E_z as mode functions:

$$\psi_{s1} = -j\,\beta_s \sum_{n=1,3,\ldots} E_{xn}\,\frac{1}{n\pi} 2\cos n\pi x\,\frac{\sin q_n(y+h)}{\sin q_n h} \quad in \quad slot \tag{6.32}$$

$$\psi_{s2} = -j\,\beta_s \int_0^\infty dk_x\, e_x(k_x)\frac{1}{k_x}\sqrt{2/\pi}\cos k_x x\, e^{-|k_y|\,y} \quad in \quad air \tag{6.33}$$

so that the normalization condition becomes

$$I_1 + I_2 = \int_0^{1/2} dx \int_{-h}^{0} dy\, \psi_{s1}^2 + \int_0^\infty dx \int_0^\infty dy\, \psi_{s2}^2 = \frac{1}{A^2} \tag{6.34}$$

and

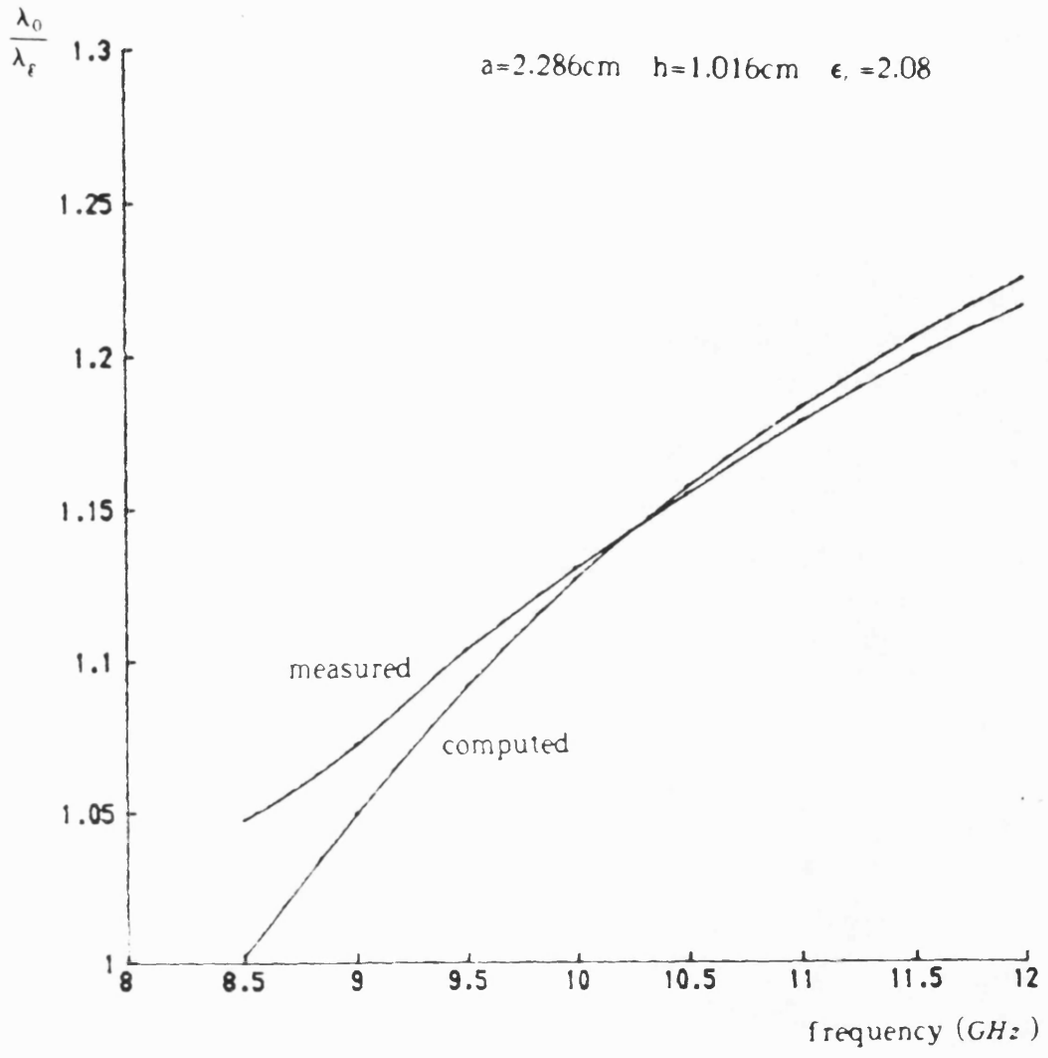

Figure 6.1 A comparison of computed and measured dispersion curves for a shallower *IDG* sample at X-band.

(M = 3)

The normalised coefficients of eigenfunction				
frequency	λ_0/λ_g	X_1	X_3	X_5
9.0	1.0448	1.0000	-0.8021	-0.0104
9.5	1.0867	1.0000	-0.8032	-0.0095
10.0	1.1225	1.0000	-0.8069	-0.0093
10.5	1.1531	1.0000	-0.8117	-0.0095
11.0	1.1794	1.0000	-0.8170	-0.0098
11.5	1.2022	1.0000	-0.8226	-0.0103
12.0	1.2221	1.0000	-0.8282	-0.0109
12.5	1.2396	1.0000	-0.8337	-0.0116
13.0	1.2550	1.0000	-0.8393	-0.0124

Table 6.1

Computed Eigenvalue and Coefficients of Eigenvector

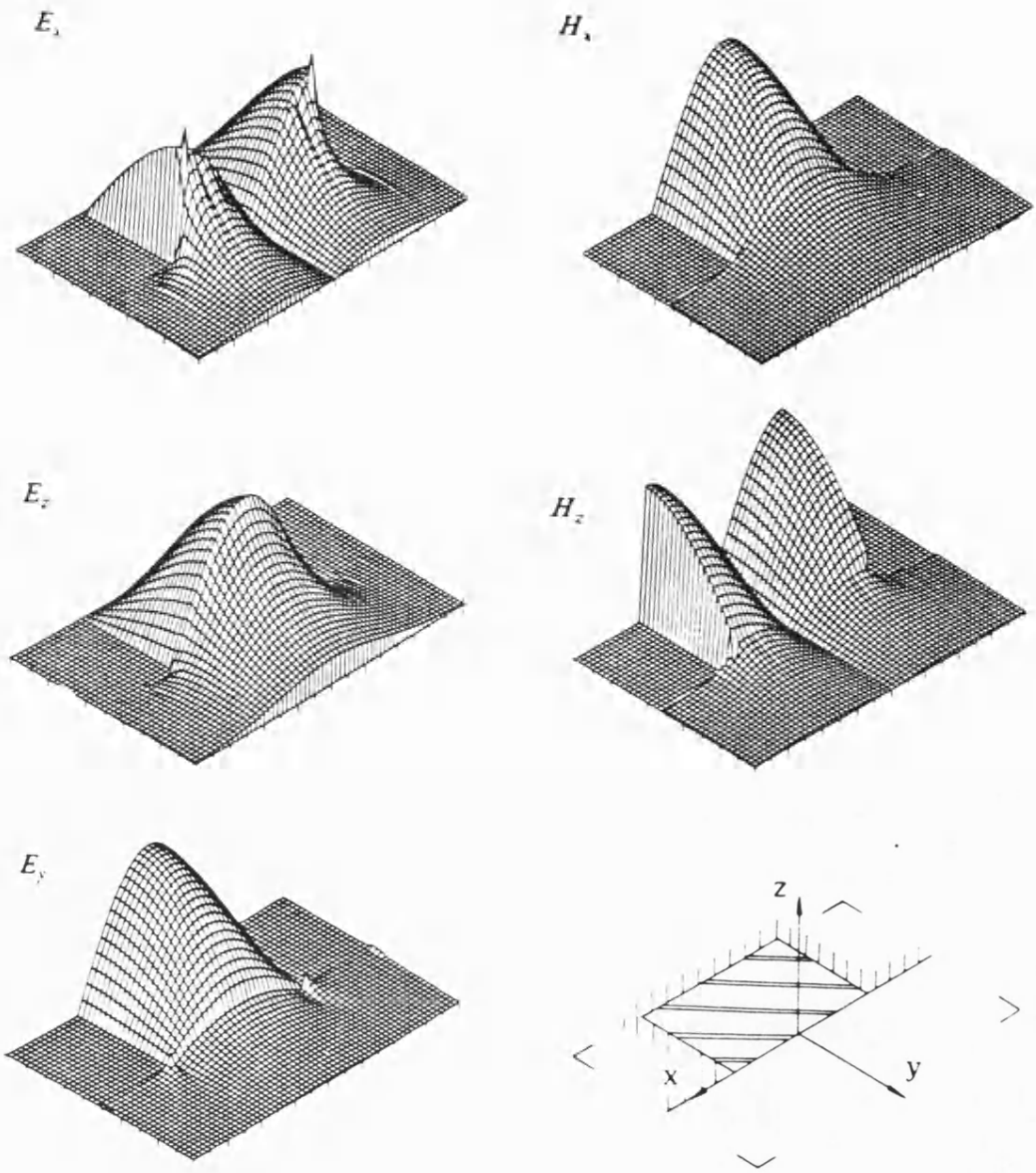

Figure 6.2 The field magnitude plots of E_{11} mode over the transverse guide section.

$$I_1 = -\beta_s^2 \sum_{n=1,3,\ldots} \left(\frac{\sum_{m=1,3,\ldots} P_{mn} X_m}{n\pi} \right)^2 \left(\frac{h}{2\sin^2 q_n h} - \frac{1}{2 q_n \tan q_n h} \right) \tag{6.35}$$

$$I_2 = -\beta_s^2 \int_0^\infty dk_x \left(\frac{\sum_{m=1,3,\ldots} P_m(k_x) X_m}{k_x} \right)^2 \frac{1}{2|k_y|} \tag{6.36}$$

The computed result is $A = j4.424912$.

6.2 The Continuous LSM Spectrum, Mode Completeness, Green's Function.

Besides the discrete modes discussed before, the *IDG* being an open two-dimensional structure, its complete spectrum contains a continuous part. Each (E_z) component of the continuum is a phase-shifted plane wave in the air region of the type

$$\psi_2(x,y;k_x,k_y) = \sqrt{2/\pi}\cos k_x x \ \sqrt{2/\pi}\sin(k_y y + \alpha) \tag{6.37}$$

where the phase-shift α is a function of both k_x and k_y due to the nonseparable nature of the problem.

It is noted that now k_x, k_y are taken as the independent variables of the expansion.

In the slot region, the E_z field can be expressed as

$$\psi_1(x,y;k_x,k_y) = \sum_{n=1,3,\ldots} a_n \, 2\cos n\pi x \sqrt{2/\pi} \frac{\sin q_n(y+h)}{\sin q_n h} \tag{6.38}$$

where

$$q_n^2 = (\varepsilon_r - 1) k_0^2 - (n\pi)^2 + k_x^2 + k_y^2 \tag{6.39}$$

It is the purpose of this section to derive the amplitudes and the phase-shift α in such a way that the orthonormalization condition

$$\int\int_{section} \psi(x,y;k_x,k_y)\, \psi(x,y;k_x,k_y)\, dx\, dy = \delta(k_x - k_x')\, \delta(k_y - k_y') \tag{6.40}$$

is satisfied.

This process has been carried out in detail, from first principles, in Appendix 4.1 for the *LSE* case and since it is here substantially analogous, its steps are retraced briefly. Continuity of (6.37) and (6.38) at $y=0$ imposes the condition

$$a_n = Q_n(k_x) \sin \alpha \tag{6.41}$$

where

$$Q_n(k_x) = \int_0^{1/2} \phi_n(x)\, \phi(x,k_x)\, dx$$

$$= \frac{2\sqrt{2}}{\sqrt{\pi}} (-1)^{\frac{n+1}{2}} \frac{n\pi \cos \frac{k_x}{2}}{k_x^2 - (n\pi)^2}$$

$Q_n(k_x)$ is interpreted as the 'ideal transformer box' from the airwaves (6.37) to the 'slot modes' (6.38) at the interface $y=0$, as shown in Fig.(4.5). Two air waves such as (6.37), corresponding to different wavenumbers $\mathbf{k}_t = (k_x,k_y)$, do not couple in the air region. The discontinuous interface $y = 0$, however, couples different values of k_x. The phase shift α describes the composite effect on an air wave of the presence of the slot, i.e. diffraction at the interface and multiple reflection in the slot. In circuit terms, the impedance of the slot, as seen by the above air wave at the interface, including the scattering into other airwaves, is given by:

$$\sum_{n=1,3,\ldots} q_n \cot q_n h\, Q_n(k_x) \int_0^{\infty} dk_x\, Q_n(k_x)$$

$$= \sum_{n=1,3,\ldots} q_n \cot q_n h\, Q_n(k_x) \sqrt{2\pi} \equiv k_y \cot \alpha$$

This expression for α does not converge when n tends to infinity. However, from (6.37) and (6.38) the expressions for E_x can be written as

$$E_x = \partial_x \frac{\Psi}{-j\beta} = \sum_n a_n \frac{n\pi}{j\beta} 2 \sin n\pi x \sqrt{2/\pi} \frac{\sin q_n(y+h)}{\sin q_n h} \quad \text{in slot}$$

$$= \frac{k_x}{j\beta} \sqrt{2/\pi} \sin k_x x \sqrt{2/\pi} \sin (k_y y + \alpha) \quad \text{in air}$$

The continuity of E_x at $y=0$ yields

$$a_n = Q_n(k_x)\sin\alpha$$

$$Q_n(k_x) = \frac{2\sqrt{2}}{\sqrt{\pi}}(-1)^{\frac{n+1}{2}}\frac{k_x^2}{n\pi}\frac{\cos\frac{k_x}{2}}{k_x^2-(n\pi)^2}$$

From the normalization condition of E_z we obtain

$$\delta(k_x - k_x')k_y\cos\alpha = \sum Q_n(k_x)\,Q_n(k_x')q_n cot\ q_n h \tag{6.42}$$

Dividing both sides of (6.42) by k_x^2 and integrating over k_x' we find

$$cot\alpha = 4\frac{k_x^4}{k_y}\cos\frac{k_x}{2}\sum_n(-1)^{\frac{n+1}{2}}\frac{q_n\,cotq_n h}{(n\pi)^3(k_x^2-(n\pi)^2)} \tag{6.43}$$

It is possible to check from first principles, or from direct integration, that with the above choice of $\alpha=\alpha(\mathbf{k}_t)$, the orthonormalization (6.40) holds and, moreover, that continuum is orthogonal to the discrete spectrum derived in the previous section. Hence we have established the complete *LSM*-spectrum of the *IDG*, which satisfies the completeness relationship

$$\sum_s \psi_s(x,y)\,\psi_s(x',y') + \int_0^\infty dk_x \int_0^\infty dk_y\ \psi(x,y;\mathbf{k}_t)\,\psi(x',y';\mathbf{k}_t)$$

$$=\delta(x-x')\,\delta(y-y') \tag{6.44}$$

As mentioned in Chapter 4, as long as the normalized mode spectrum is known, the Green function can be written like (4.68).

6.3 Scattering by a Longitudinal Dipole on the Air-Dielectric Interface.

The longitudinal electric field at the air-dielectric interface, $y=0$, is at its maximum value. The interface also constitutes the most accessible plane of the guide. This is therefore an ideal location for a source, such as a dipole, placed across the slot aperture or for a discontinuity, such as a metal strip or disk, with a view to realising circuit elements or a leaky wave antenna. Having derived the Green function we shall therefore

consider the scattering by a thin longitudinal current element, representing an independent source or an induced one, located at the origin, sufficiently thin to be representable as

$$\mathbf{J}(x,z) = \mathbf{a}\, J_0\, J_z(z)$$

where J_0 is a constant and $J_z(z')$ can be written as

$$J_z(z) = \sqrt{1-(2z/l)^2}\; e^{-j\beta_z z} \tag{6.45}$$

The scalar Green function (6.47) is that pertaining to a z-directed electric field distribution assumed as the source of the electro-magnetic field. If the source term is constituted by a z-directed electric current **J**, then the electric field E_z is related to G through the z-component of the vector potential A_z, given by

$$A_z(\mathbf{r}) = -\mu_0 \int_{-l/2}^{l/2} dz'\, G(0,y,z;0,0,z')\, J_z(z')$$

and the resulting scattered field in the air region is

$$\begin{aligned} E_z^s &= -j\omega A_z + \frac{1}{j\omega\mu_0\varepsilon_0}\frac{\partial^2}{\partial z^2}A_z \\ &= j\omega\mu_0 \int_{-l/2}^{l/2} dz\, (1 + \frac{1}{k_0^2}\frac{\partial^2}{\partial z^2})\, G\, J_0\, J_z(z') \end{aligned} \tag{6.46}$$

The coordinate system is shown in Fig.(6.3b). Ignoring the contribution from the surface mode and the evanescent radiation modes to the scattered far field we get

$$\begin{aligned} E_z^s \approx j\omega\mu_0 J_0 & \int_0^{\sqrt{k_0^2 - k_x^2}} dk_y \int_0^{k_0} dk_x \frac{1}{2j\beta}\psi(0,y)\,\psi(0,0) \\ & \int_{-l/2}^{l/2} dz'\, (1 + \frac{1}{k_0^2}\frac{\partial^2}{\partial z^2})\; e^{-j\beta|z-z'|}\, J_z(z') \end{aligned} \tag{6.47}$$

where ψ is the normalized mode function for E_z of the continuous spectrum in the air region.

A method can be used here which is analogous to that used in the *LSE* case. To

evaluate the far field pattern in yz-plane at $x=0$, we define η and θ as shown in Fig.(6.3a). From the wavenumber conservation $k_x^2 + k_y^2 + \beta^2 = k_0^2$, we have $dk_x = -(\beta/k_x)\, d\beta$, and then

$$\int_0^{\sqrt{k_0^2 - k_x^2}} dk_y \int_0^{k_0} dk_x \frac{1}{\beta} = -\int_0^{\sqrt{k_0^2 - \beta^2}} dk_y \int_0^{k_0} d\beta \frac{1}{k_x}$$

$$= -\int_0^{\pi/2} d\eta \int_0^{\pi/2} d\theta\, k_{yz} \tag{6.48}$$

From Fig.(6.3b) for the region $0 < \gamma < \pi/2$, assuming R large, then $z \geq l/2 \geq z'$. Hence, in the Green's function, we may set

$$e^{-j\beta|z-z'|} = e^{-j\beta z}\, e^{j\beta z'} \tag{6.49}$$

Then

$$\Psi(x,y,z) = \psi(x,y)\, e^{-j\beta z}$$

$$\Psi(x',y',z') = \psi(x',y')\, e^{j\beta z'}$$

$$E_z^s(0,y,z) = -\frac{\omega\mu_0}{2} \int_0^{\pi/2} d\eta \int_0^{\pi/2} d\theta\, k_0 \sin\eta\, \Psi(0,y,z)\, D_r \tag{6.50}$$

where

$$D_r(\eta, \theta) = \int_{-l/2}^{l/2} dz'\, \Psi(0,0,z')\, J_0\, J_z(z') \tag{6.51}$$

$$\Psi(\eta, \theta) = (1 + \frac{1}{k_0^2}\frac{\partial^2}{\partial z^2})\, \Psi(0,y,z)$$

$$= (1 - \sin^2\eta \cos^2\theta)\, \Psi(0,y,z) \tag{6.52}$$

Substituting (6.37) and (6.45) into (6.51) gives

$$D_r(\eta,\theta) = \int_{-l/2}^{l/2} dz' 2/\pi \sin\alpha\, J_0 \sqrt{1 - (2z'/l)^2}\; e^{-j(\beta_s - \beta)z'}$$

After making use of the parity of the integrand, integrating by parts and changing the variable, D_r becomes

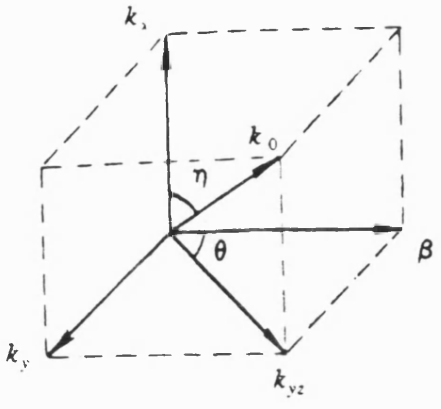

$$k_z = k_0 \cos\eta$$
$$k_{yz} = k_0 \sin\eta$$
$$\beta = k_{yz} \cos\theta$$
$$k_y = k_{yz} \sin\theta$$

(a) The trigonometric decomposition of the wavenumber.

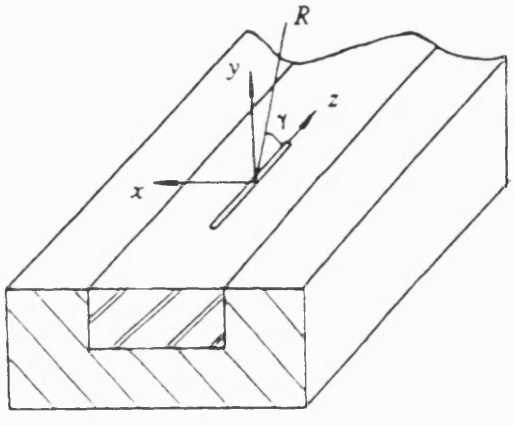

$$z = R \cos\gamma$$
$$y = R \sin\gamma$$

(b) Coordinate system.

Figure 6.3 The trigonometric decomposition of the wavenumber and the coordinate system used in the evaluation of the far field pattern.

$$D_r(\eta, \theta) = J_0\, l \sin\alpha \frac{J_1(\frac{\beta_s - \beta}{2} l)}{(\frac{\beta_s - \beta}{2} l)} \tag{6.53}$$

Now the double integral in (6.50) can be evaluated directly by numerical integration. Furthermore, the trigonometric form of the integrand leads itself naturally to the evaluation of the far field by the saddle point method. From (6.43), it can be seen that α is an odd function of θ, therefore, the integrand in (6.50) is an even function of θ, that is $\sin(k_y y + \alpha)\sin\alpha$. From the parity, we obtain

$$\int_0^{\pi/2} d\theta \sin(k_y y + \alpha)\sin\alpha = \frac{j}{2}\int_{-\pi/2}^{\pi/2} d\theta\, e^{-j(k_y y + \alpha)} \sin\alpha$$

so that E_z^s can be written as

$$E_z^s = -\frac{\omega\mu_0}{2}\int_0^{\pi/2} d\eta \int_{-\pi/2}^{\pi/2} d\theta\, k_0 \sin\eta(1 - \sin^2\eta\cos^2\theta)$$
$$\frac{2}{\pi}\frac{j}{2} e^{-j(k_y y + \beta z + \alpha)} D_r \tag{6.54}$$

Going over to cylindrical coordinates as shown in Fig.(6.3b):

$$z = R\cos\gamma$$

$$y = R\sin\gamma$$

so that

$$\beta z + k_y y = k_0 R \sin\eta\cos(\theta - \gamma)$$

the relative value of E_z^s can be rewritten as

$$E_z^s = \frac{-j\omega\mu_0 J_0 l}{2\pi}\int_0^{\pi/2} d\eta \int_{-\pi/2}^{\pi/2} d\theta \sin\eta\,(1 - \sin^2\eta\cos^2\theta)$$
$$D_r\, e^{-j\alpha}\, e^{-j R k_0 \sin\eta\cos(\theta - \gamma)} \tag{6.55}$$

By making use of the saddle point method (see appendix 4.2) we deduce

$$E_z^s = -\omega\mu_0 J_0\, l\, \frac{e^{-jk_0R}}{R} \sin^2\gamma\, D_r(\pi/2,\, \gamma)\, e^{-j\alpha(\pi/2,\, \gamma)} \tag{6.56}$$

The radiation patterns are plotted in Fig.(6.4) for various values of dipole length and frequency and are compared with that of an isolated dipole in free space, i.e. $\sin^2\gamma$. It can be seen that the pattern is not sensitive either to dipole length or frequency.

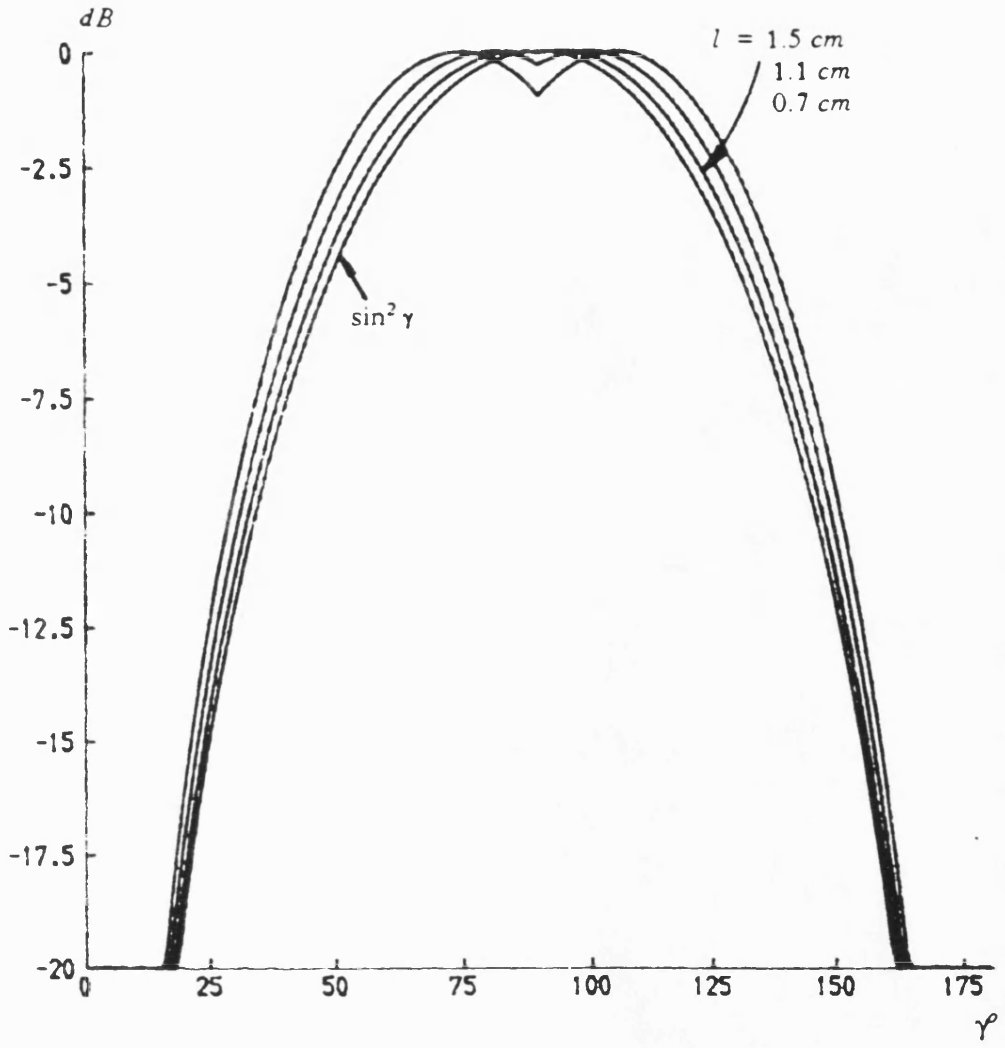

Figure 6.4a Far field pattern for various dipole lengths compared with that of an isolated dipole in free space ($\sin^2 \gamma$).

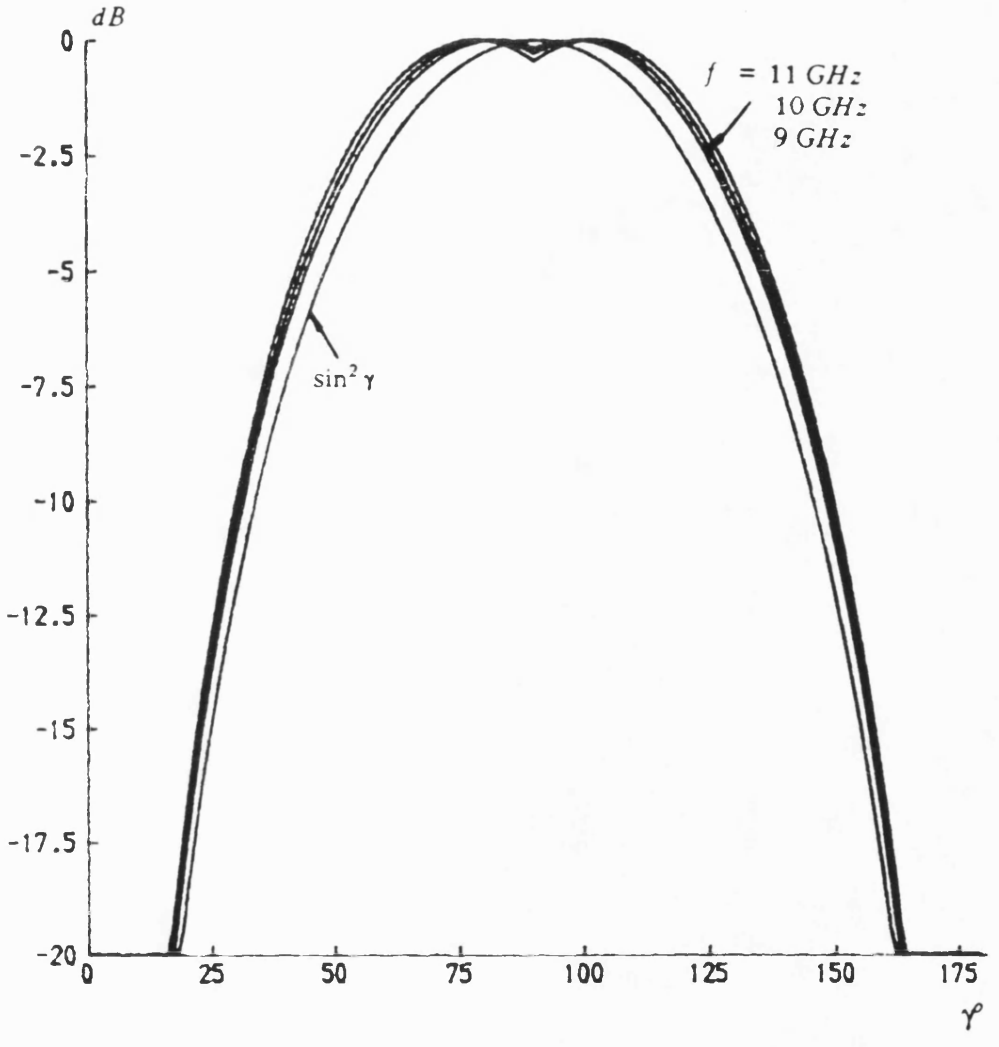

Figure 6.4b Far field pattern for various frequencies compared with $\sin^2 \gamma$.

CHAPTER 7

EQUIVALENT NETWORK OF A SINGLE LONGITUDINAL DIPOLE, ARRAY DESIGN AND TEST.

7.1 Introduction

The array composed of transverse strips on *IDG* operating in the *LSE* mode, as discussed in Chapter 5, offers a fan beam at microwave or millimeter wave frequency. It radiates a vertically polarized wave. Consider this kind of wave incident on a plane boundary separating two nonmagnetic isotropic media with dielectric constant ε_1 and ε_2. There is an incident angle θ_b, called the Brewster angle,[1]

$$\theta_b = \tan^{-1}\sqrt{\varepsilon_2/\varepsilon_1} \tag{7.1}$$

at which there is no reflected power. If reflected power is used as signal, the region around the Brewster angle will become a blind region. For horizontally polarized waves, there is no Brewster angle. That makes it preferable in some applications.

Longitudinal dipoles on *IDG* supporting an *LSM* mode can constitute an array with a very pure horizontal polarization. From the field distributions shown in Fig.(6.2) we can see that the maximum of H_x and the zero of H_z are at the center of the air-dielectric interface. Therefore if a longitudinal metallic strip is located near the center of the guide

as shown in Fiq.6.3b, a z-directed current will be induced efficiently, and the x-directed current will be negligible. As shown in Fiq.6.3b, the center of the strip is at $(x_0,0,0)$, and the width and length of the strip are w and l respectively.

The current distribution can be written as

$$\mathbf{L}_z(x,z) = \mathbf{z}\, I_z(x)\, J_z(z)$$

where **z** is the unit vector in the z direction. $I_z(x)$ and $J_z(z)$ are proportional to the distributions of H_x in the x and z directions respectively.

At the edge of the strip, $x = \pm\frac{w}{2}$, H_x being transverse to the edge, is singular to the order –1/2. At $z = \pm l/2$, H_x, being parallel to the edge, has a zero of the order 1/2. The absolute value of the current is not important. Therefore the current distributions can be written as

$$I_z(x) = \frac{1}{\sqrt{1-(2x/w)^2}} \tag{7.2}$$

$$J_z(z) = \sqrt{1-(2z/l)^2}\; e^{-j\beta_s z} \tag{7.3}$$

7.2 Equivalent Π Network for a Longitudinal Dipole

Compared with the equivalent network of a transverse dipole in the *LSE* case, a simple shunt admittance, the equivalent network of a longitudinal dipole in the *LSM* case is more complicated because of the distribution of the current along the z-axis. An equivalent Π circuit for a symmetrical two port network satisfying reciprocity is used as shown in Fig.7.1. Its *Y* parameters can be written in matrix form as:

$$\begin{bmatrix} I_1 \\ I_2 \end{bmatrix} = \begin{bmatrix} Y_{11} & Y_{12} \\ Y_{12} & Y_{11} \end{bmatrix} \begin{bmatrix} V_1 \\ V_2 \end{bmatrix} \tag{7.4}$$

We shall use "even/odd" mode analysis by placing a magnetic/electric wall on the plane of symmetry z=0. For an even current distribution $J_{ze}(z)$, V_1=V_2. Hence, from

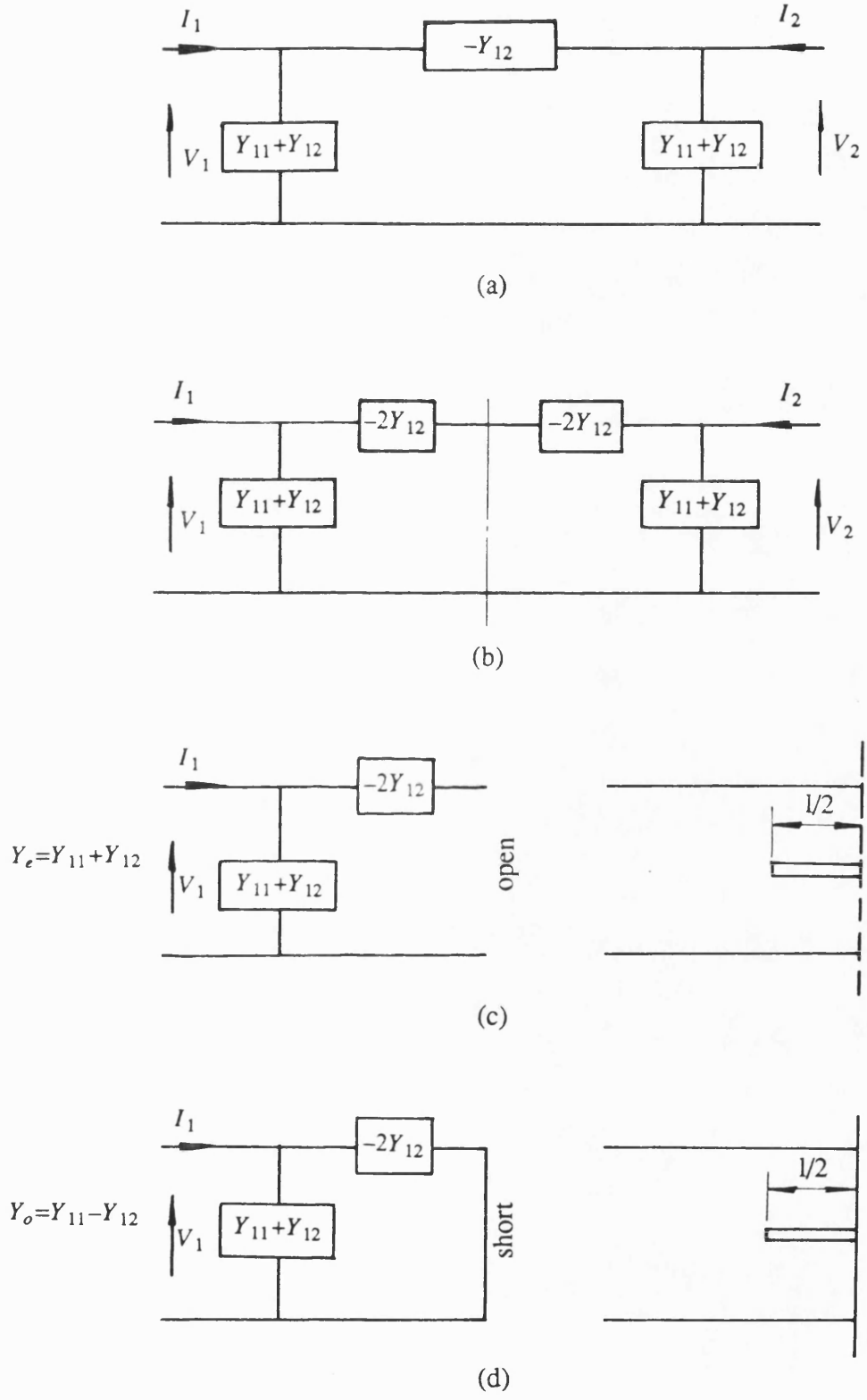

Figure7.1 Equivalent Π network of a longitudinal dipole.

(7.4) we obtain:

$$Y_e = Y_{11}+Y_{12} \tag{7.5}$$

For an odd current distribution $J_{zo}(z)$, $V_1 = -V_2$, then

$$Y_o = Y_{11}-Y_{12} \tag{7.6}$$

If we can obtain Y (or the reflection coefficient Γ) for the even and odd cases respectively, then Y_{11} and Y_{12} can be found from (7.5) and (7.6) as:

$$Y_{11} = \frac{Y_e+Y_o}{2} \tag{7.7}$$

$$Y_{12} = \frac{Y_e-Y_o}{2} \tag{7.8}$$

For the Π network shown in Fig.7.1, the *ABCD* parameters can be deduced directly by Kirchoff's laws. The result is

$$\begin{bmatrix} A & B \\ C & D \end{bmatrix} = \begin{bmatrix} -\dfrac{Y_{11}}{Y_{12}} & -\dfrac{1}{Y_{12}} \\ -\dfrac{Y_{11}^2 - Y_{12}^2}{Y_{12}} & -\dfrac{Y_{11}}{Y_{12}} \end{bmatrix} \tag{7.9}$$

and the expressions for the reflection and transmission coefficients of the dipole are

$$\Gamma = \frac{A+B-C-D}{A+B+C+D} = \frac{-1+Y_{11}^2-Y_{12}^2}{-2\,Y_{11}-1-Y_{11}^2+Y_{12}^2} \tag{7.10}$$

$$T = \frac{2}{A+B+C+D} = \frac{2\,Y_{12}}{-2\,Y_{11}-1-Y_{11}^2+Y_{12}^2} \tag{7.11}$$

7.3 The Analysis of the Network Parameters

The amplitude of the reflected fundamental mode for $z < -l/2$ is given by

$$\int_{-l/2}^{l/2} dz' \int_{-w/2}^{+w/2} dx' \frac{\omega\mu_0}{2\beta_s}\left(1-\frac{\beta_s^2}{\varepsilon_r k_0^2}\right) \psi_s(x,y)\, \psi_s(x',0)\, e^{-j\beta_s(z'-z)} J_z(z') I_z(x')$$

$$= \Gamma(z)\, \psi_s(x,y)\, e^{-j\beta_s z} = \Gamma_0\, \psi_s(x,y)\, e^{j\beta_s z} \tag{7.12}$$

where the reflection coefficient $\Gamma_0 = \Gamma(z)\, e^{j2\beta_s z}$ is defined by this equation. It can be imagined as the reflection caused by a hypothetical discontinuity located at $z = 0$.

From (7.12)

$$\Gamma_0 = \frac{\omega\mu_0}{2\beta_s}\left(1-\frac{\beta_s^2}{\varepsilon_r k_0^2}\right) \int_{-w/2}^{+w/2} dx'\, \psi_s(x',0)\, I_z(x') \int_{-l/2}^{l/2} dz'\, e^{-j\beta_s z'}\, J_z(z') \tag{7.13}$$

On the dipole, the total tangent electric field E_z must be zero, i.e.

$$E_z^i(x, 0, z) + E_z^s(x, 0, z) = 0 \tag{7.14}$$

The above equation can be rewritten as

$$\psi_s(x, 0) e^{-j\beta_s z}$$

$$+\frac{\omega\mu_0}{2\beta_s} \int_{-w/2}^{+w/2} dx'\, \psi_s(x, 0)\, \psi_s(x',0)\, I_z(x') \int_{-l/2}^{l/2} dz'\, \left(1 + \frac{1}{k_0^2}\frac{\partial^2}{\partial z^2}\right) e^{-j\beta_s |z-z'|} J_z(z')$$

$$+\int_0^\infty dk_x \int_0^\infty dk_y \frac{\omega\mu_0}{2\beta} \int_{-w/2}^{+w/2} dx'\, \psi(x, 0; k_t)\, \psi(x',0; k_t)\, I_z(x')$$

$$\int_{-l/2}^{l/2} dz'\, \left(1 + \frac{1}{k_0^2}\frac{\partial^2}{\partial z^2}\right) e^{-j\beta |z-z'|} J_z(z') = 0 \tag{7.15}$$

where ψ_s and ψ are the mode functions for discrete and continuous modes. ψ is evaluated for $y \geq 0$, hence $\varepsilon_r = 1$. At $y=0$, they are given as follows:

$$\psi_s(x, 0) = j\beta_s \int_0^\infty dk_x \frac{e_x(k_x)}{k_x} \sqrt{2/\pi} \cos k_x x$$

$$\psi(x, 0) = \sqrt{2/\pi} \cos k_x x \sqrt{2/\pi} \sin \alpha$$

and

$$cot\alpha = 4\,\frac{k_x^4}{k_y}\,\cos\frac{k_x}{2}\sum_n (-1)^{\frac{n+1}{2}}\,\frac{q_n\,cotq_n h}{(n\pi)^3\,(k_x^2-(n\pi)^2)} \tag{6.43}$$

Multiplying (7.15) by $J_z(z)$ and $I_z(x)$ and integrating wrt. z and x, we obtain

$$-\int_{-w/2}^{+w/2} dx\psi_s(x,0)\,I_z(x)\int_{-l/2}^{l/2} dz\; e^{-j\beta_s z}J_z(z)$$

$$=\frac{\omega\mu_0}{2\beta_s}\left(\int_{-w/2}^{+w/2} dx\psi_s(x,0)\,I_z(x)\right)^2\int_{-l/2}^{l/2} dz\int_{-l/2}^{l/2} dz'\;\left(1+\frac{1}{k_0^2}\frac{\partial^2}{\partial z^2}\right)\,e^{-j\beta_s|z-z'|}\,J_z(z)\,J_z(z')$$

$$+\int_0^\infty dk_x\int_0^\infty dk_y\frac{\omega\mu_0}{2\beta}\left(\int_{-w/2}^{+w/2} dx\psi(x,0)\,I_z(x)\right)^2$$

$$\int_{-l/2}^{l/2} dz\int_{-l/2}^{l/2} dz'\;\left(1+\frac{1}{k_0^2}\frac{\partial^2}{\partial z^2}\right)\,e^{-j\beta|z-z'|}\,J_z(z)\,J_z(z') \tag{7.16}$$

Dividing both sides of (7.16) by the square of its left hand side and substituting from (7.13), gives

$$-\frac{\omega\mu_0}{2\beta_s}\left(1-\frac{\beta_s^2}{\varepsilon_r k_0^2}\right)\frac{1}{\Gamma}$$

$$=\frac{\omega\mu_0}{2\beta_s}\frac{\displaystyle\int_{-l/2}^{l/2} dz\int_{-l/2}^{l/2} dz'\;\left(1+\frac{1}{k_0^2}\frac{\partial^2}{\partial z^2}\right)\,e^{-j\beta_s|z-z'|}\,J_z(z)\,J_z(z')}{\left(\displaystyle\int_{-l/2}^{l/2} dz\;e^{-j\beta_s z}J_z(z)\right)^2}$$

$$+\int_0^\infty dk_x\int_0^\infty dk_y\frac{\omega\mu_0}{2\beta}\left(\int_{-w/2}^{+w/2} dx\psi(x,0)\,I_z(x)\right)^2$$

$$\frac{\displaystyle\int_{-l/2}^{l/2} dz\int_{-l/2}^{l/2} dz'\;\left(1+\frac{1}{k_0^2}\frac{\partial^2}{\partial z^2}\right)\,e^{-j\beta|z-z'|}\,J_z(z)\,J_z(z')}{\left(\displaystyle\int_{-w/2}^{+w/2} dx\psi_s(x,0)\,I_z(x)\right)^2\left(\displaystyle\int_{-l/2}^{l/2} dz\;e^{-j\beta_s z}J_z(z)\right)^2} \tag{7.17}$$

We can rearrange (7.17) in the following sequence.

a) Cancel the common factor $\frac{\omega\mu_0}{2}$

b) Define

$$sc = \frac{1}{\beta_s}(1 - \frac{\beta_s^2}{k_0^2})$$

$$sx = \int_{-w/2}^{+w/2} dx \psi_s(x, 0)\, I_z(x)$$

$$cx(k_t) = \int_{-w/2}^{+w/2} dx \psi(x, 0)\, I_z(x)$$

$$sz = \int_{-l/2}^{l/2} dz\ e^{-j\beta_s z} J_z(z)$$

c) Use the change of variables

$$\beta = k_0 \cos\eta$$

$$k_t = k_0 \sin\eta$$

$$k_x = k_t \cos\theta$$

$$k_y = k_t \sin\theta$$

as shown in Fig.6.3a to obtain

$$\int_0^{\infty} dk_x \int_0^{\infty} dk_y \frac{1}{\beta} = \int_0^{\pi/2} d\theta \int_0^{\infty} k_t\, dk_t \frac{1}{\beta}$$

$$= \int_0^{\pi/2} d\theta \int_0^{\pi/2} d\eta\, k_t + \int_0^{\pi/2} d\theta \int_{\pi/2}^{\pi/2 + j\infty} d\eta\ k_t \qquad (7.18)$$

d) Use the change of variable $j\eta_1 + \frac{\pi}{2} = \eta$ in the second double integral, the latter becoming

$$\int_0^{\pi/2} d\theta \int_{\pi/2}^{\pi/2 + j\infty} d\eta\, k_t = j \int_0^{\pi/2} d\theta \int_0^{\infty} d\eta_1\, k_t$$

and $\sin\eta = ch\ \eta_1$, and $\cos\eta = -jsh\ \eta_1$.

Taking into account a) - d), (7.17) can be rewritten as

$$-sc\,\frac{1}{\Gamma} = \frac{1}{\beta_s\, sz^2}\int_{-l/2}^{l/2} dz \int_{-l/2}^{l/2} dz'\ (1+\frac{1}{k_0^2}\frac{\partial^2}{\partial z^2})\ e^{-j\beta_s|z-z'|} J_z(z)\,J_z(z')$$

$$+\frac{1}{sx^2\, sz^2}\int_0^{\pi/2} d\theta \int_0^{\pi/2} d\eta\ k_t\, cx^2(k_t)$$

$$\int_{-l/2}^{l/2} dz \int_{-l/2}^{l/2} dz'\ (1+\frac{1}{k_0^2}\frac{\partial^2}{\partial z^2})\ e^{-j\beta|z-z'|} J_z(z)\,J_z(z')$$

$$+j\,\frac{1}{sx^2\, sz^2}\int_0^{\pi/2} d\theta \int_0^{\infty} d\eta_1\ k_t\ cx^2(k_t)$$

$$\int_{-l/2}^{l/2} dz \int_{-l/2}^{l/2} dz'\ (1+\frac{1}{k_0^2}\frac{\partial^2}{\partial z^2})\ e^{-j\beta|z-z'|} J_z(z)\,J_z(z') \qquad (7.19)$$

In (7.19) sc is a constant for a given frequency. The integrals sx, cx(k_t) and sz can be done analytically. It is obvious that the first term in the right hand side of (7.19) is the contribution from the guided mode, the second from the propagating radiation modes and the third from the evanescent radiation modes.

It was mentioned that the commonly employed solenoidal eigenfunction expansion of the Green's function is incomplete within the region containing an arbitrarily oriented electric current point source. An explicit delta function term is required for making that expansion complete in the source region. Tai[2], Collin[3], Johnson[4] and Yaghjian[5] found that a complete set of the eigenfunction expansion should include the irrotational (or longitudinal) eigenfunctions in addition to the commonly used solenoidal eigenfunctions. By using different methods, they got different forms of results for different constructions. With our case as an example, we can explain the appearance of the δ function in a simpler way, without using the dyadic form of Green's function. On a longitudinal dipole the current is in the propagating direction. Therefore the $\frac{d^2}{dz^2}\, e^{-j\beta|z-z'|}$ term is involved in the evaluation of the scattered z-directed electric field. The first derivative of $e^{-j\beta|z-z'|}$ can be written as:

$$\frac{d}{dz}\, e^{-j\beta|z-z'|} = -j\beta\,(\,T\,(z-z') - T\,(z'-z)\,)\, e^{-j\beta|z-z'|} \tag{7.20}$$

where

$$T(z) = \begin{cases} 1 & z>0 \\ 0 & z<0 \end{cases}$$

From the application of distribution theory [6], we obtain the second derivative as:

$$\frac{d^2}{dz^2} e^{-j\beta|z-z'|} = -2j\beta\,\delta(z-z') - \beta^2\, e^{-j\beta|z-z'|} \tag{7.21}$$

From (7.21), it can be seen that when, and only when, a z-directed current exists, an explicit delta function appears in the expression of the electric field, because of the discontinuity of the derivative of the Green's function at the source point. Substituting (7.21) into (7.19) we obtain:

$$\begin{aligned}
-sc\,\frac{1}{\Gamma} = \frac{1}{sz^2}\Bigg(& sc \int_{-l/2}^{l/2} dz \int_{-l/2}^{l/2} dz'\; e^{-j\beta_s|z-z'|} J_z(z)\, J_z(z') - j\,\frac{\int_{-l/2}^{l/2} dz\, J_z^2(z)}{k_0^2} \Bigg) \\
& + \frac{1}{sx^2\, sz^2} \int_0^{\pi/2} d\theta \int_0^{\pi/2} d\eta\; cx^2(k_t) \\
& \left(\frac{1}{2} k_0 \sin^3\eta \int_{-l/2}^{l/2} dz \int_{-l/2}^{l/2} dz'\; e^{-j\beta|z-z'|} J_z(z)\, J_z(z') - j\sin\eta\cos\eta \int_{-l/2}^{l/2} dz\, J_z^2(z) \right) \\
& + j\,\frac{1}{sx^2\, sz^2} \int_0^{\pi/2} d\theta \int_0^{\infty} d\eta_1\; cx^2(k_t) \\
& \left(\frac{1}{2} k_0\, ch^3\eta \int_{-l/2}^{l/2} dz \int_{-l/2}^{l/2} dz'\; e^{-j\beta|z-z'|} J_z(z)\, J_z(z') - sh\eta\, ch\eta \int_{-l/2}^{l/2} dz\, J_z^2(z) \right)
\end{aligned} \tag{7.22}$$

In (7.22) the product of $J_z(z)$ and $J_z(z')$ is always real. For the surface modes and the propagating radiation continuum, β_s or β are real, therefore $e^{-j\beta|z-z'|}\, J_z(z)\, J_z(z')$ splits into real and imaginary parts. For the evanescent radiation continuum, it is pure real.

From (7.3) $J_{ze}(z)$ and $J_{zo}(z)$ can be written as:

$$J_{ze}(z) = \sqrt{1-(2z/l)^2}\ (-j\sin\beta_s z) \tag{7.23a}$$

$$J_{zo}(z) = \sqrt{1-(2z/l)^2}\ \cos\beta_s z \tag{7.23b}$$

Substituting (7.23) into (7.22) yields Γ_e and Γ_o, consequently Y_e and Y_o. By using (7.5) through (7.8), we obtain Γ and T. The radiation loss L_{rad} is given by:

$$L_{rad} = 1 - |\Gamma|^2 - |T|^2$$

and the phase shift of T is

$$\theta_T = \tan^{-1}\ \frac{image(T)}{real(T)}$$

It is not easy to get entirely satisfactory results for the quadratures in (7.22) because of the singularity of the integrands at the source point. Some further work needs to be done.

7.4 The Measurement of the Scattering Parameters of a Single Dipole on IDG

Electric-field probes are shown to be well-suited for direct standing wave measurements on dielectric guides. The results from the measurements of the guided wavelength and the field distribution have proven the movable electric-field probe to be a simple and reliable measuring technique for dielectric guides [7],[8]. Furthermore, the use of the probe was extended to the measurement of *VSWR* on dielectric guides in order to investigate the attenuation constants of the lines and to determine the effects of line discontinuities in the dielectric guides [9]. We have used this technique to determine the wavelength of *IDG*. Now we describe the experiments for the determination of the reflections from matched *IDG* terminations and from a thin longitudinal dipole on *IDG*.

The experimental setup is shown in Fig.7.2, where the two-stub tuner is used to enhance the sensitivity of the probe. The whole probe, including the tuner and the detector, is mounted on a vernier mechanism to ensure the probe moves along the line

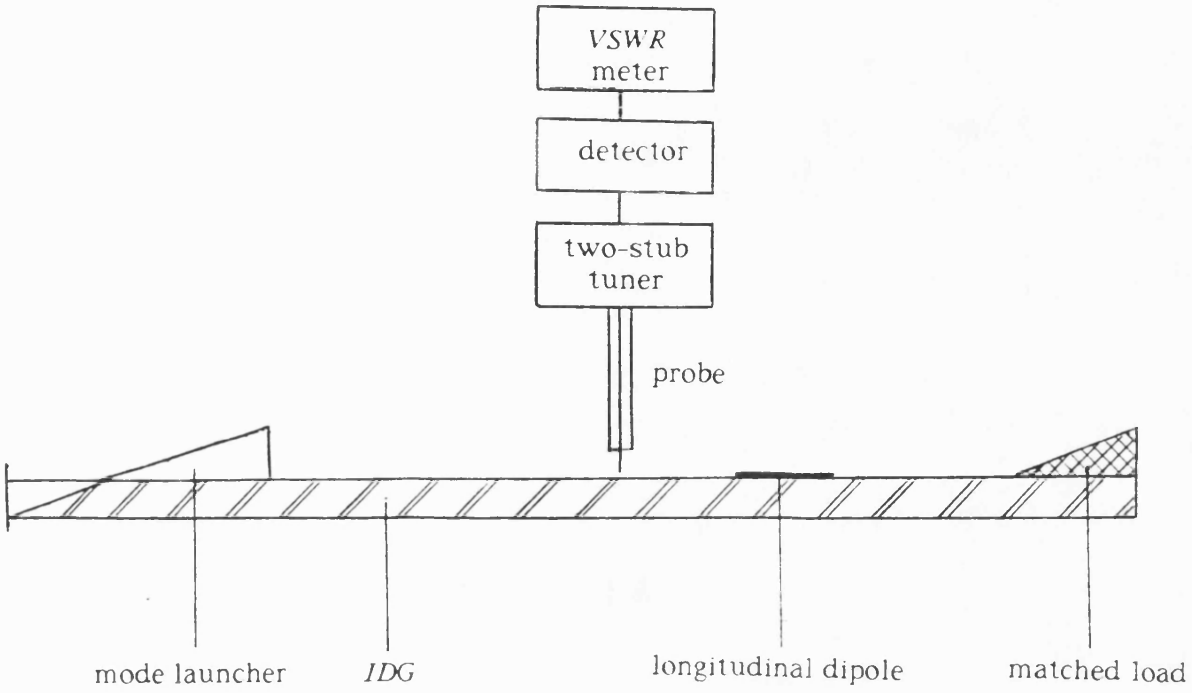

Figure 7.2 The experimental setup for the measurements of the reflection from a longitudinal dipole on *IDG*.

smoothly. This is very important because of the fact that the fields of the guided wave of the *IDG* decay exponentially with the distance from the line, so that the measured voltage of the field decreases with increasing distance from the line. The modulated wave incident from the launcher propagates along the *IDG* and is dissipated at the matched termination or is terminated by a second transition in place of the matched load. In either case, the wave is reflected partially at the termination and the resulting standing wave pattern on the *IDG* can be observed by means of the electric-field probe. The matched load was made of a piece of tapered absorbing material. Its *VSWR* was measured to be about 1.05 at 10 *GHz*. When a metal strip is placed on the top of the *IDG*, the incident wave is scattered. One part of the incident guided wave is reflected in the form of a guided wave, resulting in the standing wave pattern between the mode launcher and the strip. Another part of the wave is radiated, resulting in the nonuniformity of the field pattern near the strip. The third part of the wave is transmitted to the matched load at the end of the *IDG*.

In this kind of experiment, difficulties arise from a) nonuniformities of the lines, and b) the radiation field due to the mode launcher. For the *IDG* case, the first factor is not serious, but the second must be considered carefully.

The *IDG* E_{11} mode field distribution is very different from that of metal rectangular waveguide. Hence, if they are connected together directly, the discontinuity at the junction will cause strong radiation, particularly for the E_{11} mode. In order to improve the transition, an E-plane flared horn is used between the waveguide and the *IDG*, as shown in Fig.7.2. The advantage of using the horn is illustrated in Fig.7.3. The lower trace shows the S_{11} of the configuration in Fig.7.2; the upper trace that without horn. With this experimental setup, the *VSWR* of a metal strip (width 2 mm, length 1.1 mm) was measured to be about 1.35.

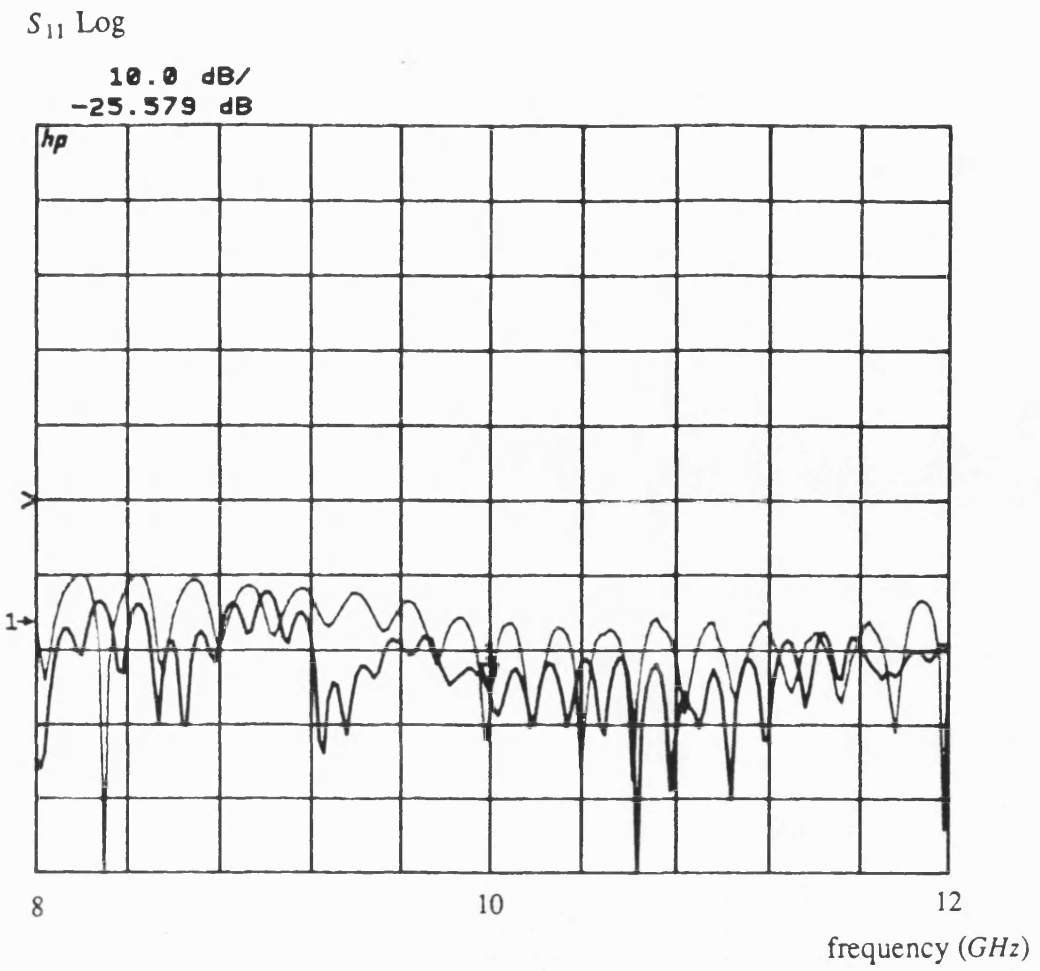

Figure7.3 The reflection coefficient of the mode launcher.
upper trace: without horns
lower trace: with horns.

A network analyzer is used to measure the S_{21} of a strip. The absolute value of the transmission coefficient of the dipole can be determined by comparing the S_{21} of the configuration with and without the strip on the top of the *IDG*. The measured results show that the absolute value of S_{21} is about 1 dB.

7.5 Array Design and Testing.

From the field distribution, we found that if we use a coaxial probe to excite the guide, the mode transition would be more natural. Furthermore, the feed point can be set at the center of the array, which reduces the full length of the array and makes the structure symmetrical. With these ideas in mind, we built a 15-element array with all the strips of the same dimensions (2 mm wide, 11 mm long), as shown in Fig.1.3. The ends of the array were loaded with absorbing material. Because the impedance of *IDG* is higher than that of coaxial line, the coaxial probe was placed 2 mm offset. To get a stronger coupling the distances between the probe and its adjacent elements were set to $\lambda_g/8$ and $3\lambda_g/8$, respectively. In order to compensate for the phase shift of each strip, the length of the strips was chosen to be 11 mm, and the spacing between two adjacent elements was 13 mm, i.e. half a guided wavelength.

The reflection coefficient of the array was measured with the HP 8510 vector network analyzer. The result shown in Fig.7.4 represents a good match over a fairly broad band. Trace 1 is the result when the array was terminated with absorbing material, trace 2 is the result when the array was terminated with short circuits. The closeness of these two curves shows that the radiation from the dipoles is very strong, therefore not much power reaches the terminals. The radiation pattern was tested in a full size anechoic chamber shown in Fig.7.5. For an array of $11.5\,\lambda_0$ length, with a tapered current distribution, without any special design, a half power beamwidth of 7^o represents a very good result, probably because of the element directivity. The sidelobe level is

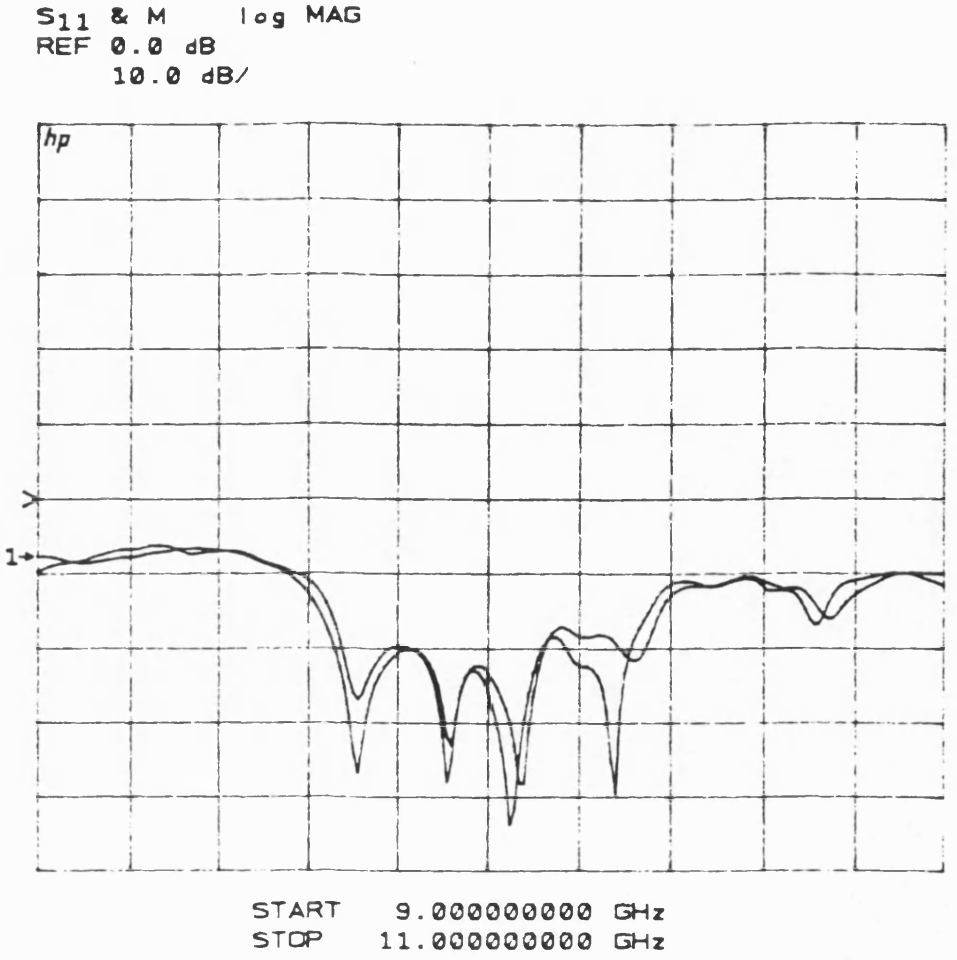

Figure7.4 The reflection coefficient of a 15-element array of Fig.1.3.

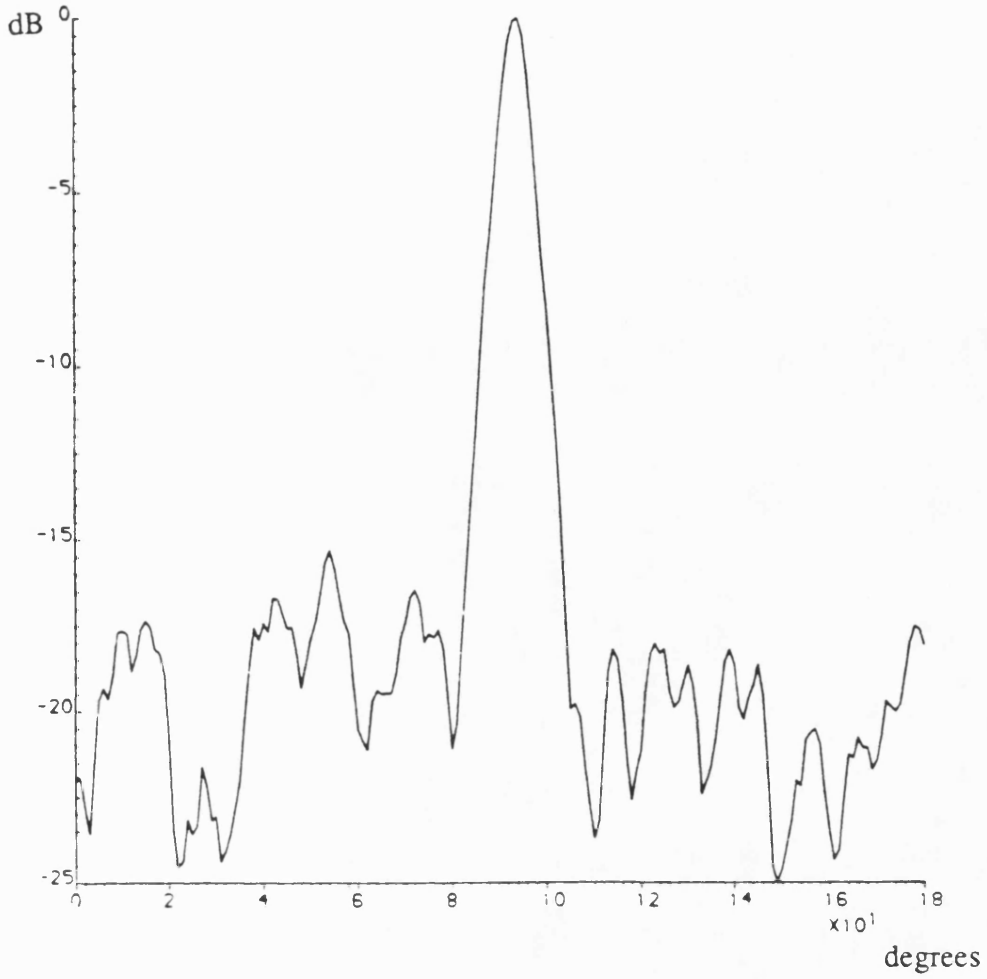

Figure7.5 The far field pattern of a 15-element array of Fig.1.3.

more than 15 dB lower than the mainlobe level. The results seem to indicate that if we were able to obtain the equivalent network for a single longitudinal dipole and use it to realize a proper current distribution by controlling the dimensions and positions of the strips, an even better performance could be expected.

REFERENCES

[1] Jin Au Kong, "Theory of Electromagnetic Waves," John Wiley & Sons, 1975.

[2] C. T. Tai, "On the eigenfunction expansion of dyadic Green's functions," Proc. IEEE. vol. 61, pp. 480-481, 1973.

[3] R. E. Collin, "On the incompleteness of E and H modes in waveguides," Can. J Phys., vol. 51, pp. 1135-1140, 1973.

[4] W. A. Johnson, A. Q. Howard, and D. G. Dudley, "On the irrotational component of the electric Green's dyadic," Radio Sci., vol. 14, pp. 961-967, 1979.

[5] A. D. Yaghjian, "electric dyadic Green's functions in source regions," Proc. IEEE, vol. 68, pp. 248-263,1980.

[6] J. Van Bladel, Electromagnetic Fields, Washington D.C., Hemishere, 1985.

[7] G. Novick, R. Walter, C. M. Locascio, and H. Jacobs, "Probe measurement of guide wavelength in rectangular silicon dielectric waveguide," in *IEEE int. Microwave Symp. Digest* (San Diego CA) pp. 118-120, June 1977.

[8] K. Solbach, "The fabrication of dielectric image lines using casting resins and the properties of the lines in the millimeter-wave range," *IEEE Trans. Microwave Theory and Tech., vol. MTT*-24, pp. 879-881, Nov. 1976.

[9] K. Solbach, "Electric probe measurements on dielectric image lines in the frequency range of 26-90 GHz." *IEEE Trans. Microwave Theory and Tech., vol. MTT*-26, pp.755-758, Oct. 1978.

CHAPTER 8

CONCLUSION

The objective of this concluding chapter is to bring together the work of the previous seven chapters. A discussion of the results and their significance will enable suggestions to be made for the further work in this area.

8.1 Discussion of the Work Presented in This Thesis

The work presented in this thesis has been concerned with the analysis of Inset Dielectric Guide (*IDG*) and its application in microwave and millimeter wave antennas.

The practical importance of millimetric wave was discussed in the beginning of this thesis. It is apparent that the choice of a particular structure for a certain application is the result of an engineering compromise between several factors. *IDG* was introduced as a practical evolution from image line with the potential for easier manufacture and improved performance.

A rigorous method of analysis for *IDG*, which was developed by Rozzi and Hedges, was discussed in Chapter 3 and extended to the odd mode case. This method is based on

the Transverse Resonance Diffraction (*TRD*) approach. It involved the derivation of the field components from a transverse equivalent circuit model. The resonance of this circuit then gave a set of coupled integral equations in the electric field components transverse to y. These were then solved by Galerkin's method using a basis set that accurately modelled the electric field variation across the interface. The choice of basis function in the formulation of the dispersion equation was demonstrated to be accurate by the fast convergence of the solution and the accuracy of the computed results.

The nature of the field was dependent on the geometry of the guide, i.e. for a guide with $h/a > 1$, the fundamental hybrid mode was essentially LSE_{01}; for $h/a < 1$, the hybrid mode can be expected to be LSM_{11}. The calculated dispersion curves based on *LSE*/*LSM* approximation showed excellent agreement with the measured results.

As an open waveguide, the spectrum of *IDG*, besides the discrete modes, includes a continuous range of modes. Once the complete spectrum is found, an appropriate Green's function of the guide can be constructed, which is commonly used in the analysis of discontinuity and radiation problem. Completing the characterization of the spectrum of *IDG* so as to include the continuum was one of the major aims of this work. The mathematical difficulty in the normalization of the continuum arises from the nonseparable nature of the two-dimensional cross section. The solution for this case had not been reported before this work started.

The complete spectrum was used to form the Green function, whereby the far field pattern of a single dipole could be evaluated.

This theory was successfully used in Chapter 5 to discover the equivalent network of a transverse dipole on the top of *LSE*-polarized *IDG*. A 23-element, 50 cm long array was designed and tested. The far field pattern and the other antenna characteristics demonstrate that the performance of the *IDG* antenna is superior to that of a traditional

slotted waveguide array of the same dimension, and its ease of manufacture is obvious, which is an important factor for the application at millimetric wave band. A coarse design and test of a 15-element array (in *LSM*-polarization) verified the feasibility of a horizontally polarized array with longitudinal dipoles.

We believe this thesis has demonstrated that *IDG* as an open, nonseparable two-dimensional structure possesses value for both theoretical research and practical application.

8.2 Suggestion for the Further Work in This Area

The investigation of *IDG* as a practically useful millimetric transmission medium is by no means complete. Further work is suggested as follows:

1) Investigate the equivalent network for a longitudinal dipole. Design and test horizontally polarized arrays.

The current on a longitudinal dipole is in the propagating direction. Therefore a $\frac{\partial^2}{\partial z^2} e^{-j\beta|z-z'|}$ term is involved in the evaluation of the scattered E_z. The discontinuity of the derivative of $e^{-j\beta|z-z'|}$ at the source point results in a delta function in the second derivative of $e^{-j\beta|z-z'|}$. This makes accurate quadrature not easy and some appropriate techniques and skill are still needed.

2) Design of circularly polarized arrays.

As the nature of the field depends on the geometry of the guide, for a certain dimension, a truly hybrid mode can exist. With properly arranged longitudinal and transverse dipoles, or some cross elements, a circularly polarized antenna can be constructed.

3) Realize two-dimensional arrays.

A very important feature of the *IDG* antenna is the virtual decoupling of the near field between parallel arrays. Coupling via surface waves on the substrate, which is a real problem in microstrip and image line antennas, is prevented here by the metal side walls of the guide. Therefore the *IDG* configuration is ideally suited to the realization of two-dimensional arrays.

4) Improve the mode launcher.

In order to realize a two-dimensional array as mentioned before, proper feed circuitry is necessary. The parallel arrays can be excited by slots on the narrow wall of a standard waveguide, but there may be better ways. For circularly polarized arrays, excitation from the end of the array might be necessary. The mode launcher, i.e. the transducer between the rectangular waveguide and the *LSM*-polarized *IDG*, needs to be improved further.

5) Extend the technique used in the normalization of the continuum of *IDG* to the other open structures.

6) Use *IDG* as transmission media to realize some passive components and active devices, such as filter, coupler, detector, mixer and so on.

8.3 Conclusion

It has become a universally recognized fact that the open dielectric waveguides are of direct importance to the areas of integrated optics, millimeter-wave integrated circuits and flat (or planar) antennas. For use above 100 GHz, popular structures like microstrip and finline can no longer be used. Image line has shown its disadvantage in being difficult to control radiation wherever a discontinuity appears. The work presented in

this thesis demonstrates that *IDG*, as a more practical variant of image line, has shown all the advantages of dielectric guides such as low metallic loss, ease of fabrication, low cost and good performance, without the disadvantages of some other guides. Furthermore it seems to offer particular promise for the flat antenna applications including high gain, high aperture efficiency and low loss. The need to continue work in this area is evident.